Cellular and molecular mechanisms of ANCA-associated vasculitis

Dissertation

zur

Erlangung des Doktorgrades (Dr. rer. nat.)

der

Mathematisch-Naturwissenschaftlichen Fakultät

der

Rheinischen Friedrich-Wilhelms-Universität Bonn

vorgelegt von

Nina Kessler

aus

Leverkusen

Bonn, Oktober 2022

Angefertigt mit Genehmigung der Mathematisch-Naturwissenschaftlichen Fakultät

der Rheinischen Friedrich-Wilhelms-Universität Bonn

Gutachter und Betreuer: Prof. Dr. Natalio Garcia Garbi

Gutachterin: Prof. Dr. Irmgard Förster

Tag der Promotion: 22.06.2023

Erscheinungsjahr: 2023

Content

Abbreviations

Abbreviation	Spelled
AAPV	Pulmonary ANCA-associated vasculitis
AAV	ANCA-associated vasculitis
AIM2	Absent in melanoma 2
AMs	Alveolar macrophages
ANCA	Anti-neutrophil cytoplasmic antibodies
BALF	Bronchoalveolar lavage fluid
BAS	Bronchoalveolar space
CD	Cluster of differentiation
cGAMP	2'3' cyclic GMP-AMP
cGAS	Cyclic GMP-AMP synthetase
d	Day
ddH_2O	Double distilled water
DHR123	Dihydrorhodamine 123
dsDNA	Double stranded DNA
E2	Estradiol
E2P4	Estradiol + Progesterone
EAE	Experimental autoimmune encephalomyelitis
EDTA	Ethylenediaminetetraacetic acid
ELISA	Enzyme-linke immuno sorbant assay
EnCs	Endothelial cells
EpCs	Epithelial cells
FACS	Fluorescence-activated cell scanning
FCS	Fetal calf serum
fMLP	N-Formyl-Met-Leu-Phe
FMO	Fluorescence minus one
HET	House of experimental therapy
i.p.	Intraperitoneal
i.t.	Intratracheal

Abbreviation	Spelled
IC	Immune complex
ICAM-1	Intercellular adhesion molecule-1
IFN	Interferon
IFNAR-1	IFN alpha/beta receptor alpha chain
IRF3	Interferon regulatory factor 3
ISGs	Interferon stimulated genes
IVIS	In Vivo Imaging Systems
JAK1	Janus activated kinase 1
LPS	Lipopolysaccharide
MMP	Metalloproteinases
Møs	Macrophages
MPO	Myeloperoxidase
MS	Multiple sclerosis
NADPHox	NADPH-oxidase complex
NE	Neutrophil elastase
NETs	Neutrophil extracellular traps
NO	Nitric oxide
O_2	Oxygen
P4	Progesterone
PBMCs	Peripheral blood mononuclear cells
PBS	Phosphate buffer saline
PCR	Polymerase chain reaction
PFA	Paraformaldehyde
PMNs	Polymorphonuclear leukocytes
PR	Progesterone receptor
PR3	Proteinase 3
PRRs	Pattern recognition receptors
RA	Rheumatoid arthritis
RBCs	Red blood cells

Abbreviation	Spelled
RIG-I	Retinoic acid inducible gene I
ROS	Reactive oxygen species
rpm	Revolution per minute
RT	Room temperature
s.c.	Subcutaneous
SAVI	STING-associated vasculopathy with onset in infants
SLE	Systemic lupus erythematodes
SPF	Specific pathogen free
STING	Stimulator of interferon genes
TBK1	TANK-binding kinase 1
TLRs	Toll like receptors
TNF	Tumor necrosis factor
TREX-1	Cytosolic 3’ repair exonuclease 1
TYK2	Tyrosine kinase 2
VCAM-1	Vascular cell adhesion molecule-1

List of Tables

List of Figures

Acknowledgment

First, I would like to express my deepest gratitude to Natalio! Not only did you teach me how to come up with new ideas, to think critically, and how great Aqua de Valencia tastes - you also always encouraged me to be independent, to believe in my gut feeling, and to try new things. I could always count on your support and trust. I couldn't have asked for a better supervisor. From the bottom of my heart: THANK YOU!

I would also like to thank Prof. Irmgard Förster and the rest of my committee for taking the time to evaluate my work.

Many thanks to Susi Q., with whom I had the honor of working so closely. Long days of experimentation or changing small details in manuscript figures late at night would have only been half as much fun without you. And two Monk's see double lines better than one.

Karola and Katharina, I would like to thank you for your confidence in my mentoring skills and your outstanding dedication to the lab and our project! I am sure you both have a great career ahead of you, as you are already exceptional scientists. I will always look forward to hearing or reading from you (scientifically and non-scientifically).

Special thanks, a big hug, and a shout-out go to *AG Gaaaarbiii* - you guys changed my life! Victoria, Caro, Lara, and Markus - my salad sisters - A total eclipse of my heart - not having you guys by my side in the lab anymore. It was a pleasure - every day anew - to work with you, to enjoy lunch together, and to deliver the one or other performance after the one or other gin. I am so happy to have you as friends. I am already looking forward to our AG Garbi Happening - the BuGa Marathon in 2029, and then on that night, we will be young again for sure!

Further, I have many people to thank for being by my side for the past four years, and especially for sticking through the daily grind and science madness with me. Natascha, Mary, Kostas, Helena, Blanca, Andreas, Max, Ann-Kathrin, Christine, Annika, Sümeyye, Celia, and Marcel. Thank you all for being part of this trip! It was a fun ride!

Lastly, I would like to thank my flatmates, friends, and family who always believed in me and patiently listened to my complaints when science got frustrating one day or another! Much much love to you all. I return all borrowed listening time whenever you need it.

1. Introduction

1.1.Autoimmune vasculitis

Vasculitis encompasses a group of life-threatening diseases causing severe inflammation within blood vessels. Inflammation can lead to rupturing or narrowing of blood vessels damaging the organs supplied by these. The most commonly affected are the kidney, respiratory tract, and skin [1]. Vasculitis can be a primary autoimmune disease or manifest secondarily after an earlier illness, infection, or medication [2]. In 2012 a new nomenclature was introduced, classifying idiopathic vasculitis diseases based on the affected vessel size. According to this, vasculitis is divided into large, medium, or small vessel vasculitis [3]. This thesis focuses on a subgroup of small- and medium-sized blood vessel vasculitis called anti-neutrophil cytoplasmic antibodies (ANCA)-associated vasculitis.

1.1.1.ANCA-associated vasculitis

ANCA-associated vasculitis (AAV) is a subgroup of small- and medium-sized vessel vasculitis characterized by the abundance of ANCA. These autoantibodies are mainly directed against myeloperoxidase (MPO) or proteinase 3 (PR3). AAV has an incidence of around 20 million people per year in Europe and, overall, a slight male predominance [4]. However, within the group of MPO-vasculitis, which is the subject of investigation in this thesis, women are more prone to develop the disease (64%) [5].

AAV manifests with increasing age, peaking at around 60-75 years [6]. Although pathology involves several organs, kidney failure and lung hemorrhages are the most severe manifestations with poorer prognoses [7]. Patients with active disease simultaneously suffer from lesions in different organs [8] and have a poor prognosis if left untreated. 90% of patients without therapeutic intervention die within two years of diagnosis [9]. Long-term immunosuppression is required, however, with the consequence of severe side effects on immunity and fertility, among others (further details on therapy for AAV are discussed in the respective Introduction section 1.1.3.). This prediction makes it crucial to investigate the underlying disease mechanisms to elucidate different therapeutic approaches.

1.1.2.Pathogenesis of ANCA-associated vasculitis

1.1.2.1.Autoantibodies

ANCA are found in 90% of patients with AAV and are thought to be involved in the pathogenesis of ANCA-associated vasculitis [10]. The autoantibody targets MPO and PR3 are mainly stored in primary granules of neutrophils [11]. However, as low levels of ANCA are also found in healthy individuals, it is believed that they are not pathogenic themselves [12]. A well-accepted hypothesis of disease pathogenesis is that upon priming of neutrophils by a pro-inflammatory stimulus, MPO and PR3 are translocated to the cell surface, enabling antibodies to bind their target [13, 14]. In turn, neutrophils become fully activated, leading to respiratory burst and degranulation, resulting in release of immunogenic DNA into the extracellular milieu (Figure 1) [15]. Some studies suggest that increased attachment of neutrophils to the vessel wall and the release of inflammatory cytokines provoke damage to endothelial cells, resulting in pulmonary hemorrhages or kidney damage [16]. Although AAV is traditionally considered a ‘pauci-immune’ vascular inflammation, meaning without deposition of immune complexes (IC), more and more studies show IC deposition in the kidneys of patients with AAV [17] and its correlation with aggravated disease progression [18]. IC may directly interact with endothelial cells by binding via the Fc receptor [19]. However, if IC are involved in vessel breakdown during vasculitis remains unknown.

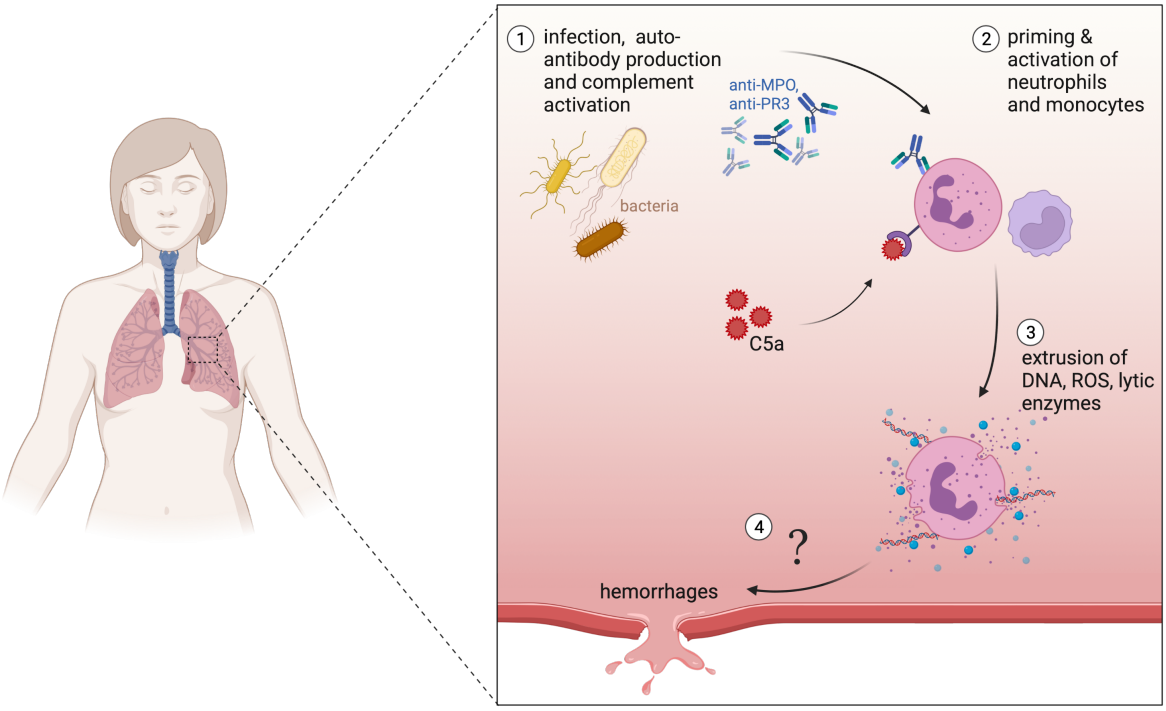

Figure 1: Currently proposed mechanism of ANCA-associated vasculitis. Bacterial or viral infections, enhanced autoantibody production, and complement activation are believed to activate neutrophils and trigger AAV pathogenesis. Neutrophils, in turn, release pathogenic molecules like ROS, lytic enzymes, and NETs, which will damage endothelial cells leading to, e.g., pulmonary hemorrhages. Figures were made with Biorender.com.

1.1.2.2.Cellular involvement

Vasculitis is a complex disease involving many different immune cell populations contributing to pathogenesis. Besides neutrophils, which are the main source of the ANCA targets MPO and PR3, other immune cells like monocytes and macrophages, as well as T lymphocytes, were found to infiltrate lesions of AAV patients. They may therefore be involved in disease pathogenesis [20].

Neutrophils are the leading producers of the ANCA targets MPO and PR3 and are therefore considered to be an essential player in disease pathogenesis [21, 22]. Depletion of neutrophils completely inhibited glomerular histological injury in a murine model of anti-MPO mediated glomerulonephritis [23], highlighting neutrophils' central role in disease induction. One pathology in patients with AAV is increased circulating DNA abundance [24-26]. Although the cellular source of

extracellular DNA is unclear, neutrophils are believed to release DNA in the form of neutrophil extracellular traps (NETs). This extracellular DNA was found to be decorated with several pro-inflammatory proteins, including histones, calprotectin [27], LL-37 [28], neutrophil elastase (NE), MPO, and PR3 [29].

Besides the release of NETs [24, 30], *in vitro* neutrophil stimulation with ANCA also induced the production of reactive oxygen species (ROS) [13]. Fuchs et al. identified a novel cell death mechanism by which NETosis and resulting neutrophil death depend on NADPH-oxidase-generated ROS [31].

Neutrophils may also mediate disease pathogenesis by producing pro-inflammatory mediators such as metalloproteases (MMP)-3 and -9, which are common biomarkers in patients with AAV [32, 33]. Metalloproteases regulate many non-immunological processes like tissue remodeling as well as immunological processes like effector functions or cell migration. MMP-9 was identified to mediate neutrophil migration [34]. Interestingly, NADPH oxidase signaling up-regulated MMP-9 [35], e.g., in atherosclerosis [36]. However, whether and how these factors might contribute to disease pathology remains to be elucidated.

Monocytes' role in AAV is still controversial. Monocytes also express MPO and PR3, and there is evidence that they are targetable by ANCA [37]. For example, O'Brien et al. demonstrated in their *in vitro* study an increased production of the pro-inflammatory cytokines interleukin (IL)-1β, IL-6, and IL-8 by monocytes upon ANCA stimulation [38]. Like neutrophils, monocytes were also found to produce ROS upon ANCA stimulation [39]. Additionally, ANCA provoked the up-regulation of CD14 - one of the receptors for lipopolysaccharide (LPS) [40], and LPS binding by CD14 resulted in tumor necrosis factor (TNF)-α production by blood monocytes [41]. In an open-label study of Infliximab - an anti-TNF-α antibody - effective remission induction in patients with AAV was observed [42], suggesting TNF-α-signaling to be an important mechanism in AAV pathogenesis.

Nevertheless, monocytes might be less likely targets of circulating ANCA as their expression of MPO, and PR3 decreases significantly upon release from the bone marrow into the blood [43] and further upon differentiation into macrophages [37]. Additionally, overall numbers of monocytes do not seem to be changed in patients with AAV compared to healthy controls [44]. At the moment, *in vivo* studies have elucidated the necessity of neutrophils in disease progression rather than the sole role of monocytes [23, 45].

Macrophages undergo dynamic changes during inflammation. While monocyte-derived macrophages are generally considered pro-inflammatory, tissue-resident macrophages often fulfill anti-inflammatory roles. In ANCA-associated vasculitis, macrophages accumulate in lesions of glomerulonephritis [46, 47]. Harper et al. demonstrated that ANCA increased the opsonization of apoptotic neutrophils and uptake by phagocytic macrophages, which on the one hand, supported tissue clearance but, on the other hand, triggered the release of pro-inflammatory cytokines [48]. Different studies have provided evidence of the anti-inflammatory role of macrophages in AAV, demonstrating that at the side of lesions, macrophages displayed increased expression of CD206 and CD163 [49], which suggests a polarized healing-associated phenotype [50]. Additionally, soluble CCL2 and CD163 were increased in the urine of patients undergoing active vasculitis [51], indicating monocyte recruitment to the side of the lesion and subsequent differentiating into anti-inflammatory macrophages.

B cells are essential key players of ANCA-associated vasculitis during the initiation phase, where an excessive production of autoantibodies is crucial for disease pathogenesis [52]. In addition, there is increasing evidence for a pathogenic role of B cells independently of antibody production. For example, B cells produce pro-and anti-inflammatory cytokines by which they can regulate T cell responses and overall innate immunity [53]. However, this function has not been investigated in AAV yet.

T cell help is required for an efficient class switch and affinity maturation of auto-reactive antibodies. In this regard, dysfunction of T regulatory cells (Tregs) has been shown to induce loss of tolerance, resulting in a pathogenic ANCA autoimmune response [54, 55]. During disease flares in the clinically relevant effector phase, increased soluble factors associated with T cell activation have been found in the serum of patients with AAV, such as sIL2R, sCD30, or BAFF [56-58]. This suggests a pathogenic role for T cells in AAV pathogenesis. Indeed $CD4^+$ T cell depletion attenuated disease progression without altering ANCA titers in a murine anti-MPO glomerulonephritis model [59]. Also, in humans, treatment with Alemtuzumab - an anti-CD52 antibody that selectively depletes lymphocytes - effectively induced remission in patients with AAV. However, relapses and adverse effects occurred frequently [60].

Endothelial cell (EnCs) damage followed by hemorrhages is a hallmark of vasculitis. EnCs display an activated phenotype in AAV, indicated by increased expression of adhesion molecules like intercellular adhesion molecule-1 (ICAM-1) [61] and vascular cell adhesion molecule-1 (VCAM-1) [62]. Up-regulation of adhesion molecules enables interactions with neutrophils that are essential for the migration of neutrophils to inflammatory sites [63]. In line with this, Radford et al. found increased adhesion of neutrophils to the endothelium upon ANCA stimulation [64]. Neutrophil signaling led to permeability of the endothelium, which can be even more perpetuated if neutrophils release, e.g., proteases like metalloproteases (MMPs) or oxidants like ROS or nitric oxide (NO) [65]. Additionally, to the direct interaction of endothelial cells and neutrophils, NETs were also found to cause endothelium injury [66, 67]. Schreiber et al. showed that NETs from *in vitro* anti-MPO activated neutrophils induced permeability in an endothelial cell monolayer indicative of EnC damage. Inhibition of RIPK3-dependent necroptosis via Nec-1 and DNase I treatment was strongly protective in this setup [68]. Histones bound to NETs might be one mechanism of how NETs provoke endothelial or epithelial injury [69].

1.1.3.Treatment of ANCA-associated vasculitis

As the underlying cellular and molecular mechanisms of ANCA-associated vasculitis are poorly understood, the most common treatment option for patients with AAV is the use of immunosuppressive agents like glucocorticoids and cyclophosphamides [70]. Glucocorticoids have many immune-modulatory actions and are therefore used as the standard therapy for autoimmune disorders [71]. Cyclophosphamide, on the other hand, acts mainly by inducing lymphopenia, particularly of B cells, thereby suppressing antibody responses [9], including those directed against self-antigens.

Although glucocorticoid therapy induced remission in up to 75% of the patients with AAV, its long-term use often results in relapses [72]. Additionally, long-term glucocorticoid therapy can cause severe side effects such as increased susceptibility to infections, a higher risk of cancer growth, and infertility [73-75]. Indeed, within the first year of treatment with glucocorticoids, 48% of patients with AAV died because of microbial infections while vasculitis-associated pathology only accounts for 19% [76].

Therapeutic intervention targeting B cells, aiming at reducing the production of pathogenic ANCA, was implemented in 2006, first to treat rheumatic arthritis [77]. However, several studies have demonstrated that B cell targeting therapy with Rituximab has similar efficacy to standard immunosuppressive therapies for AAV [72, 75, 78].

In 2021, FDA approved the use of the C5a inhibitor Avacopan for patients with ANCA-associated vasculitis. Despite effectively induced remission, adverse effects occurred in more than 80% of the patients receiving Avacopan in a randomized study [79].

Thus, although the current treatment options can reduce the mortality rate to 25% within five years of diagnosis, 50% of the patients still suffer from relapses [76]. In addition, the currently available therapeutic interventions are still accompanied by many adverse effects. This prediction makes it crucial to investigate the underlying molecular or cellular disease mechanism of ANCA-associated vasculitis to identify new targets to improve therapeutic avenues.

1.1.4. Mouse models of ANCA-associated vasculitis

The molecular and cellular mechanisms underlying ANCA-associated vasculitis are not well understood, partly because of the lack of suitable mouse models. The identification of ANCA in humans in the 1980s [80] initiated the development of mouse models mimicking AAV. Most established mouse models rely on the passive transfer of ANCA, underlining their importance in disease pathogenesis. Currently, anti-MPO antibodies are generated by immunizing MPO-deficient mice. The isolated ANCA are then transferred in wild-type mice which will cause focal necrotizing and crescentic pauci-immune glomerulonephritis [81]. Additional treatment with LPS was found to increase disease severity [82, 83]. Nevertheless, disease incidence and severity in those animal models are highly variable.

Another major disadvantage of most pre-clinical models is that they focus on kidney disease development. When starting this project, there was no published MPO-vasculitis mouse model for lung involvement. However, pulmonary inflammation and hemorrhages are common complications in patients with AAV [74, 84] and the most lethal disease manifestations during vasculitis flares [85]. Therefore, there was a high need to develop a preclinical model that mimics severe pulmonary ANCA vasculitis, which is part of this thesis.

1.2. Nucleic acid recognition in immunity

Nucleic acid sensing is a well-known defense mechanism against microbial infections. Infections are recognized by the innate immune system via pattern recognition receptors (PRRs) [86]. They are located in the cytosol or endosomes where self-DNA is not commonly found, but bacterial or viral RNA/DNA may be detected. Nucleic acid sensors like cyclic GMP–AMP synthetase (cGAS), absent in melanoma 2 (AIM2), retinoic acid-inducible gene I (RIG-I), or toll-like receptors (TLRs) belong to these PRRs. They can detect foreign DNA or RNA and, in turn, trigger a pro-inflammatory response, often via type-I interferon (IFN) production [87, 88] (Figure 2).

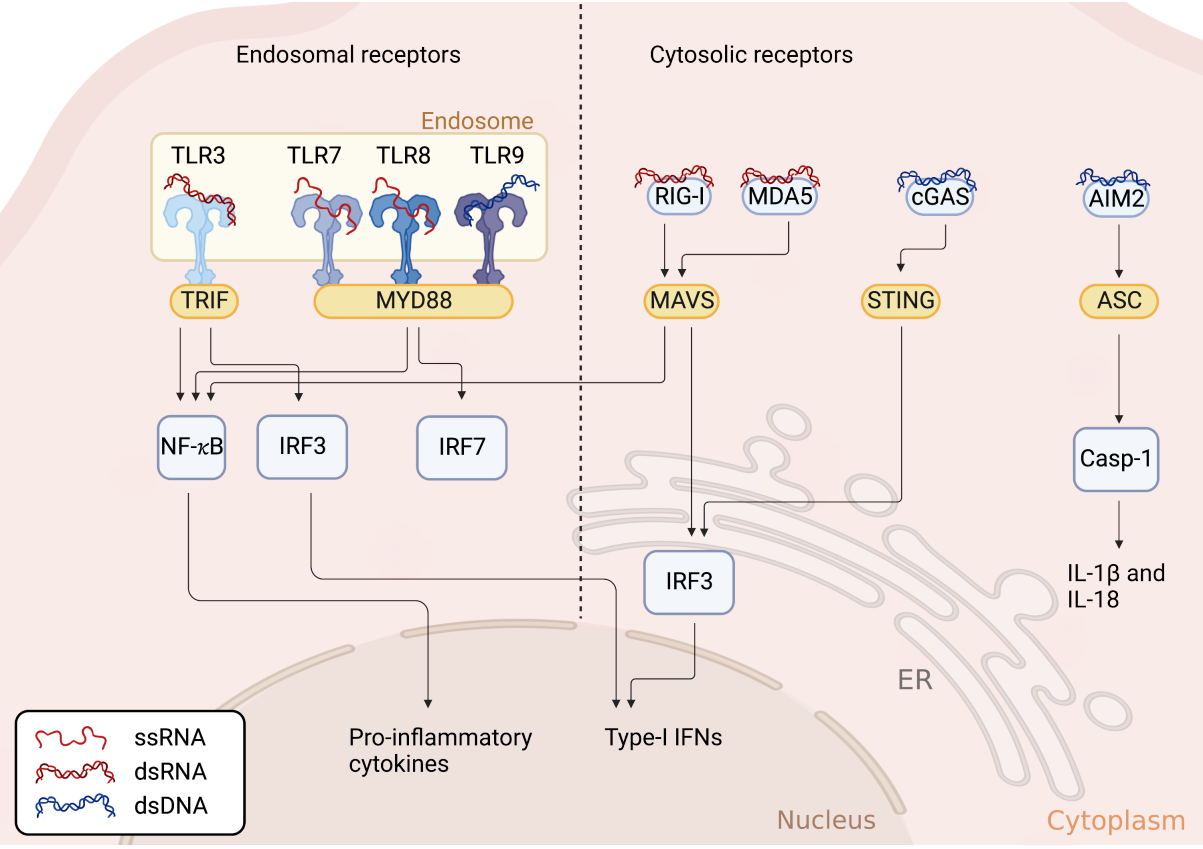

Figure 2: Endosomal and cytosolic nucleic acid sensors. Intracellular nucleic acid sensors detect foreign and self ssRNA, dsRNA or dsDNA and induce a pro-inflammatory immune response. Figures were made with Biorender.com. Adapted from [89].

However, certain conditions result in nuclear or mitochondrial DNA release to the cytosol [90, 91] and the extracellular milieu [92, 93], where DNA can be recognized by the PRRs mentioned above. In autoimmune systemic lupus erythematosus (SLE), circulating extracellular DNA was elevated [92]. Later, Christensen et al. showed that the detection of self-DNA by TLR7 was involved in the pathogenesis of SLE [94]. A regulated response to cytosolic or extracellular DNA is crucial. Nucleases degrade RNA/DNA in endosomes and cytosol, preventing their accumulation outside the nucleus. However, there are cases of pathogenic mutations, for instance, leading to the inactivation of the cytosolic 3' repair exonuclease 1 (TREX1), resulting in cytosolic DNA accumulation, which triggers exacerbated nucleic acid sensing and the development of the auto-inflammatory Aicardi–Goutières syndrome [95]. Additionally, mutations that constitutively activate the nucleic acid sensing pathway inducing pathology are reported. For instance, in STING-associated vasculopathy with onset in infants (SAVI), a gain-of-function mutation in STING results in IFN production and vascular injury [96].

1.2.1.cGAS-STING-type-I interferon pathway

DNA sensing by cGAS is considered the most common DNA recognition pathway. Double-stranded DNA (dsDNA) binding to cGAS results in the production of the second-messenger molecule 2'3' cyclic GMP-AMP (cGAMP). cGAMP then binds to the stimulator of interferon gene (STING), inducing its dimerization which, in turn, initiates its translocation from the endoplasmic reticulum to the Golgi apparatus. STING then recruits TANK-binding kinase 1 (TBK1), which upon phosphorylation, recruits interferon regulatory factor 3 (IRF3), resulting in its phosphorylation and dimerization. Finally, phosphorylated IRF3 is translocated to the nucleus, where transcription of type-I interferons (IFN) is initiated [97] (Figure 3).

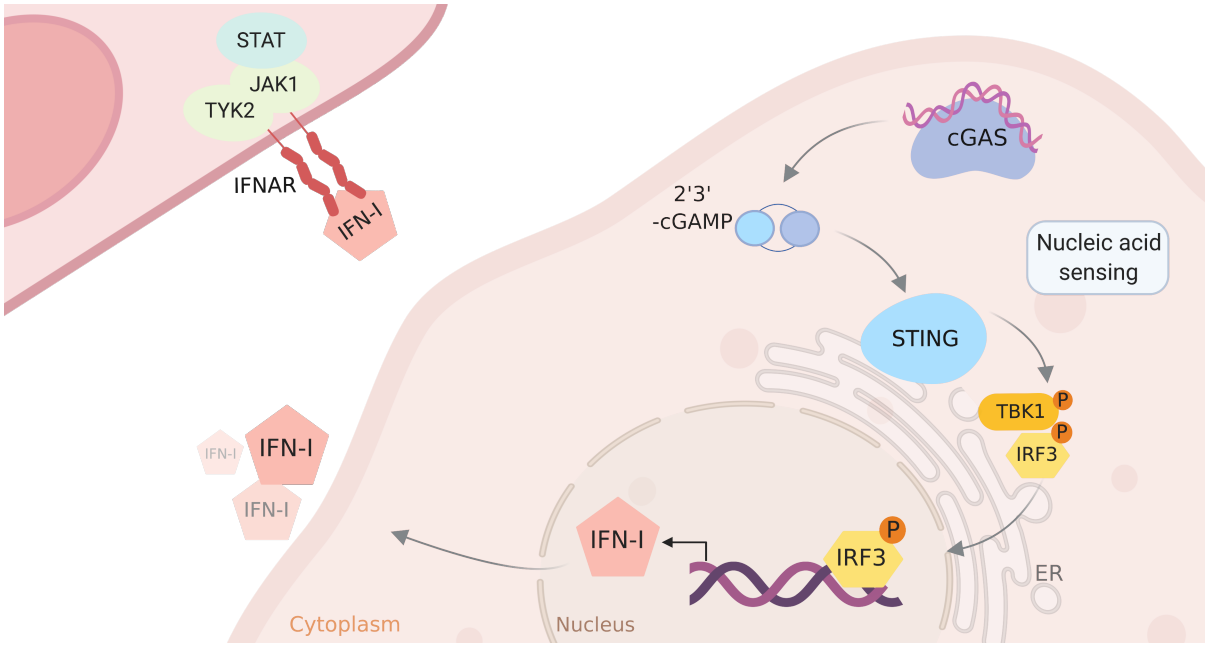

Figure 3: Nucleic acid sensing by the cGAS-STING-type-I interferon pathway. Double-stranded DNA (dsDNA) gets sensed by cGAS, leading to the production of 2'3' cGAMP. This, in turn, will activate STING, which will translocate to the Golgi apparatus phosphorylating TBK1. TBK1 induces phosphorylation of IRF3, which leads to transcription of type-I IFN after translocating to the nucleus. IFN-I can then activate the JAK/STAT pathway in an autocrine or paracrine manner. Figures were made with Biorender.com.

Type-I IFNs can signal via the interferon receptor (IFNAR) in a paracrine or autocrine manner [98]. The respective receptor consists of two subunits - IFNAR-1 [99] and IFNAR-2 [100]. The association of IFNAR with the Janus activated kinase (JAK1) and the tyrosine kinase 2 (TYK2) and the downstream signaling has been extensively studied [101, 102]. IFNAR activation triggers the expression of so-called interferon-stimulated genes (ISG) with pleiotropic effects ranging from increased cellular resistance and viral infection to promoting inflammatory immune response [103].

Besides the cell intrinsic activation of STING, Ablasser et al. reported that cGAMP can be transferred to neighboring cells through tight junctions to propagate and amplify inflammation [104]. Additionally, it was shown that 2’3’ cGAMP can be produced by bacteria, activating STING without previous recognition of DNA by cGAS [105].

The importance of cGAS/STING-signaling in different diseases is striking. Due to its central role in viral recognition of, for example, herpes simplex virus 1 (HSV-1) [106], or Kaposi's sarcoma-associated herpesvirus (KSHV) [107], cGAMP is under investigation to be used as an adjuvant. In an influenza vaccine model, co-administration with cGAMP boostered the immune response [108]. But also, in tumor immunity, cGAS was shown to be activated. Genome instability [109] or mitochondrial damage [110] results in cytosolic DNA accumulation, which is sensed by cGAS. Using STING agonists has been demonstrated to be a promising treatment option [111].

1.3.Macrophages in health and disease

Macrophages are important phagocytes involved in infections, injury, or repair. In the 1970s, macrophages were originally classified together with monocytes and dendritic cells as part of the mononuclear phagocyte system [112]. It is now well-accepted that macrophages develop from two independent origins. Embryonic macrophages develop prenatally and independently of the hematopoietic lineage, whereas macrophages during adulthood develop from infiltrating bone marrow-derived monocytes.

In general, it is believed that tissue-resident macrophages fulfill homeostatic functions [113, 114] and play a crucial role in wound healing [115] and tissue regenerative processes [116, 117]. For instance, during embryonic development, macrophages phagocytose unwanted cell structures [118, 119]. Tissue-resident macrophages specify phenotype and function within their particular organ and fulfill homeostatic roles besides immune functions [120].

In contrast, monocyte-derived macrophages are considered more pathogenic. Upon pathological conditions, Ly-6C$^+$ monocytes are released from the bone marrow via the CCR2/CCL2-axis [121] and differentiate in order to reconstitute tissue macrophages [122]. Integration was shown, for example, in the heart after myocardial infarction [123]. After they enter the tissue, monocyte-derived macrophages can adapt to their new environment and become phenotypically similar to tissue-resident macrophages [124]. However, whether they become functionally equivalent still needs to be investigated.

1.3.1. Macrophages in autoimmune diseases

The role of tissue-resident and monocyte-derived macrophages were already investigated in several autoimmune diseases. In a murine model of human multiple sclerosis (MS), called experimental autoimmune encephalomyelitis (EAE), it was shown that monocyte-derived macrophages were highly phagocytic and expressed pro-inflammatory cytokines such as IL-1β and TNF-α [125, 126]. It was further demonstrated that depletion of macrophages attenuated damage to the central nervous system in mice [127, 128] as well as in clinical trials in which macrophage apoptosis was induced in patients with MS using IFN-β [129]. Moreover, amplified macrophage polarization by IL-33 ameliorated EAE development [130].

Additionally, synovial macrophage numbers were increased in rheumatic arthritis (RA), positively correlating with articular destruction [131]. Interestingly, depletion of tissue-resident macrophages by clodronate liposome injection [132] and defective differentiation of monocytes by SIRT1 over-expression [133] ameliorated experimental arthritis. Moreover, TNF-α production by synovial macrophages is an important cytokine in the pathogenesis of RA [134].

1.4.Sex hormones and autoimmunity

5-8% of the world's population is affected by autoimmune diseases [135]. Most of the about 80 different autoimmune disorders occur more frequently in women than in men [136]. Reasons for this sex bias in prevalence and disease severity may be, on the one hand, genetic factors [137, 138]. For instance, X-chromosome-linked expression of *Tlr7* was shown to escape X-chromosome inactivation [139], increasing the risk of lupus by enhanced TLR7-driven plasma cell proliferation. On the other hand, hormonal differences between women and men may affect the immune system [140, 141].

Women are exposed to highly fluctuating levels of sex hormones, which may affect their immune status driving autoimmune diseases. The function of estrogen and progesterone on the immune system will be discussed in the following section.

1.4.1.Estrogen

Estrogens are one of the main groups of female sex hormones. They include estrone (E1), 17β-estradiol (E2), and estriol (E3), with E2 being the predominant form in premenopausal women. Estrogen production in the ovaries gradually increases from puberty at around ten years of age, reaching a peak in women of about 40 to dramastically decrease in menopause (Figure 4).

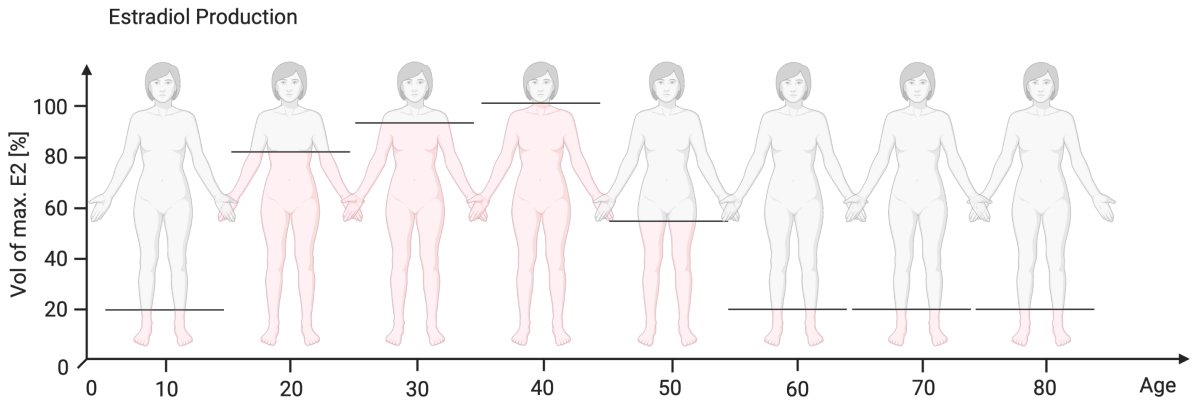

Figure 4: Estradiol levels in women over their lifespan. Circulating estradiol levels in blood of women reach their maximum at the age of 40 years and decline from then on. When entering menopause at around 50, estradiol levels start dropping to approximately 20% of the maximal estrogen levels at about 60 years of age. Figures were made with Biorender.com. Adapted from [142]**.**

Estrogens fulfill essential regulatory non-immune functions like uterine epithelial cell proliferation [143] or endometrial tissue growth [144] primarily during female reproduction by signaling via the estrogen receptor-α [145] or -β [146]. However, there is increasing interest in investigating the role of E2 in cancer, neurodegenerative diseases, and immune regulation.

Many immune cells in humans and mice express the estrogen receptor, e.g., B, T, NK cells, or macrophages [147]. Therefore, it is likely that estrogen can regulate the immune response. Indeed, E2 actions have been implicated in many autoimmune diseases, although its role is still controversially discussed. SLE, for instance, has a higher prevalence in women, and Carlsten et al. observed in a lupus model that E2 ameliorated T cell-mediated renal vasculitis [148]. Contradictory to these findings, Singh et al. claimed that estradiol increases the expression of ISGs, worsening SLE [149]. Supporting this, oral contraception and hormone replacement therapy after menopause positively correlated with a more severe SLE outcome [150]. Thus, findings point towards various estrogen actions.

Rheumatoid arthritis has a 3-fold higher incidence in women [151] and often develops after menopause. Suggesting an involvement in protection against RA progression, Hall et al. observed ameliorated disease progression in female patients who received hormone replacement postmenopausal [140]. Multiple sclerosis (MS) is another autoimmune disease that has an increased female-to-male ratio (3:1) [152]. In EAE, it has been shown that estrogen reduces the clinical manifestations of active EAE disease [141]. Estradiol has been further shown to reduce the expression of cytokines and chemokines in EAE [153] and to induce the production of anti-inflammatory cytokines like IL-4 [154].

Furthermore, Gold and colleagues investigated estriol regulation of immune cell migration. Estriol inhibited MMP-9, which hindered migration of monocytes and T cells into the CNS, reducing inflammatory lesions in EAE [155].

1.4.2.Progesterone

Progesterone (P4) is another crucial female steroid hormone complementing and counteracting the role of estrogens. Like E2, P4 is produced by the ovaries when girls enter puberty at around 10-14 years and declines upon menopause (Figure 5).

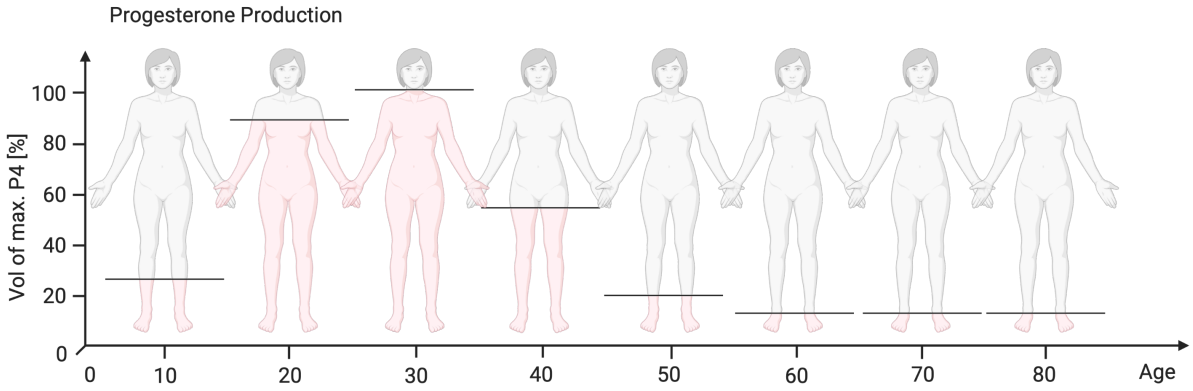

Figure 5: Progesterone levels in women over their lifespan. Circulating progesterone levels in blood of women reach their maximum at the age of 30 years and decline from then on. At the time of peri-menopause, at the age of around 40, progesterone levels start dropping to approximately 10% of the maximal estrogen levels at about 50 years of age. Figures were made with Biorender.com. Adapted from [156] based on values from [157].

Progesterone is involved in several processes of female reproduction. Ovulation depends on ovarian granulosa cells' progesterone receptor (PR) expression [158]. Lydon et al. reported that despite mature pre-ovulatory follicles, mice lacking the progesterone receptor failed to ovulate [159]. Furthermore, progesterone plays a central role in the implantation of the fertilized egg and in maintaining pregnancy [160].

Although PR is widely expressed in different immune cells like NK cells, macrophages, dendritic cells, and T cells [156], the role of progesterone in autoimmune diseases has not been investigated as extensively as that of estrogens. However, some studies implicate the involvement of progesterone in MS or RA. Symptoms of these diseases are often reduced during pregnancy when progesterone levels are strongly increased [161, 162]. In line with this, Yates et al. reported that progesterone treatment reduced the secretion of inflammatory cytokines like IL-2 and IL-17 and ameliorated disease progression in EAE [163].

1.4.3.Hormonal fluctuation in humans

Estrogen and progesterone fluctuation is a tightly regulated mechanism. Progesterone and estrogen regulate the menstrual cycle and, thus, pregnancy. In humans, the menstruation cycle in women during pre-menopause is around 28 days long [164]. During the first days (follicular phase), estrogen levels rise until they peak on ovulation (around day 14) with an estradiol concentration of around 200-250 pg/ml. After ovulation, estrogen levels decline, and progesterone rises, peaking around days 22-24, reaching about 10-15 ng/ml (luteal phase). After that, the two hormones decrease, and menstruation bleeding indicates the beginning of a new cycle [165] (Figure 6).

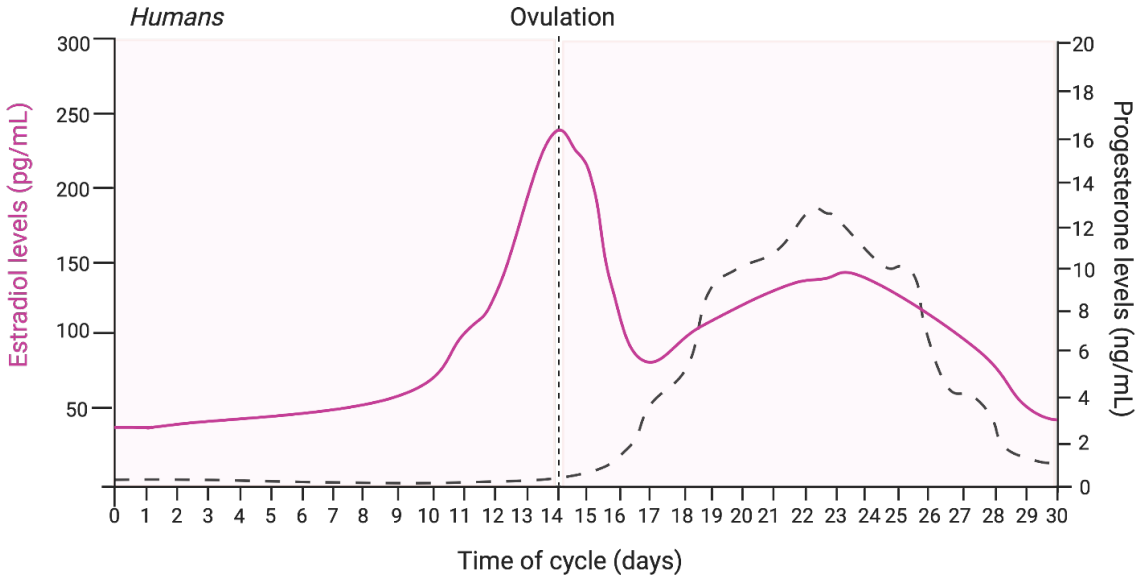

Figure 6: Estrogen and progesterone levels over the menstruation cycle in humans. In the follicular phase, estrogen levels rise until ovulation (around day 14). Subsequently, estrogen levels are decreasing, and progesterone levels are rising. The decline of progesterone induces menstruation bleeding, indicating the beginning of a new cycle. Figures were made with Biorender.com. Adapted from [165].

Hormonal imbalance occurring during peri-menopause may affect the immune system, potentially inducing autoimmune diseases. First symptoms of arthritis in women, for instance, develop at the time of menopause [166]. However, the correlation between vasculitis and hormone withdrawal during menopause has not been investigated yet.

1.4.4.Estrogens and progesterone in men

Traditionally, estrogen and progesterone have been considered female sex hormones. However, the two hormones are also expressed by men and play critical roles, especially in sexual function. Circulating estradiol in men originates from testicular secretion and peripheral aromatization of testosterone [167-170]. Serum estradiol concentrations range from around 150 pmol/L in young men to 90 pmol/L in older men, which is approximately four times less than in premenopausal women [171, 172]. Progesterone in men is produced by the testicles and the adrenal gland and rapidly converts into testosterone and other steroids. Therefore, plasma levels in adult men are similar to children or women in the follicular phase [173]. Since several studies suggest that progesterone and estrogen affect immunity and some autoimmune diseases in women, as described above, it is conceivable that they may have the same effect in males. However, estrogens and progesterone are not oscillating in men as in women, which might be a critical factor concerning their function in health and disease.

1.4.5.Testosterone

Testosterone, a steroid hormone important in determining male sexual development and associated with male reproductive function, is also expressed by the ovaries in women. In contrast to progesterone and estrogen, testosterone levels do not oscillate in women and are relatively stable. Testosterone levels increase during puberty [174], peak at age 20 - 25, and decline from then on [175, 176], while in men, testosterone levels remain stable until the age of around 80 years [176].

Circulating testosterone levels are about 15-20 times lower in women than in men [177], but still, fulfill essential functions in women's health. However, high testosterone levels may lead to irregular menstrual periods resulting in infertility [178].

Regarding the immune system, androgen-deficiency resulting from Klinefelter's syndrome was associated with an increased risk of SLE [179]. In line with this, treatment with the testosterone precursor dehydroepiandrosterone (DHEA) in an open study reduced indices of SLE activity [180, 181].

1.5. Aim of the study

The overarching goal of this study was to identify cellular and molecular mechanisms underlying the pathogenesis of severe MPO-ANCA-associated vasculitis to identify specific targets for novel potential therapeutic approaches. For this, we addressed four aims:

1. We wanted to elucidate the role of neutrophils in disease initiation and progression. Therefore, we characterized them phenotypically and functionally throughout the disease course using our newly established mouse model mimicking pulmonary AAV in patients.

2. We investigated the role of extracellular DNA accumulation in the lung and nucleic acid sensing via the STING/IFN type-I axis in the pathogenesis of pulmonary vasculitis.

3. We further investigated the role of two distinct macrophage populations and their involvement in pro- and anti-inflammatory mechanisms throughout the disease course.

4. Autoimmune diseases occur more frequently in women than men, and we observed sex differences in our mouse model. Hence, we aimed to elucidate the effect of sex hormones - specifically estradiol and progesterone - on the immune system and AAPV progression.

2. Material and Methods

2.1. Materials

2.1.1.Equipment

Table 1: Equipment

Equipment	Manufacturer
Aesculap Isis Shaver	Aesculap, Tuttlingen, Germany
Autoclave	Belimed, Cologne, Germany
Bright-field scanner Aperio AT2	Leica Biosystems, Nußloch, Germany
Centrifuge (5417R)	Eppendorf AG, Hamburg, Germany
Centrifuge (5810R)	Eppendorf AG, Hamburg, Germany
Centrifuge (Biofuge pico)	Heraeus, Braunschweig, Germany
Centrifuge (Multifuge 3 S-R)	Heraeus, Braunschweig, Germany
ChemiDoc XRS+ System	Bio-Rad, Hercules, USA
Cytospin Centrifuge	Thermo scientific GmbH, Schwerte, Germany
Dako Pen	Agilent Dako, Santa Clara, USA
Dissecting set	FST Dumont Biology, Dumont, Switzerland
Electronic balance	Sartorius, Göttingen, Germany
Electronic precision balance	Sartorius, Göttingen, Germany
Flow cytometers	Becton, Dickinson and Company, Franklin Lakes, NJ, USA
Freezer (-20°C)	AEG, Frankfurt, Germany
Freezer (-80°C)	Heraeus, Braunschweig, Germany
Heating block	Eppendorf AG, Hamburg, Germany
Heating plate for small animals	N/A
Ice machine	Frimont Bettlonic, Pogliano, Italy
Incubator	Heraeus, Braunschweig, Germany
IVIS Lumina LT Series III	PerkinElmer, Waltham, MA, USA
Mastercycler	Eppendorf AG, Hamburg, Germany
Mice cages	Techniplast, Hohenpleißenberg, Germany

Equipment	Manufacturer
Micro-centrifuge	Biozym, Hessisch Oldendorf, Germany
Micropipettes	Eppendorf AG, Hamburg, Germany
Microplate reader	Tecan Trading AG, Männedorf, Switzerland
Microscope (IX71)	Olympus, Hamburg, Germany
MicroVent ventilator	Harvard Apparatus, Cambridge, MA, USA
MouseOx™Pulse oximeter	STARR Life Science, Oakmont, PA, USA
Pipette controller	Hirschmann Laborgeräte, Eberstadt, Germany
QIAxel	Qiagen, Hilden, Germany
Refrigerators (+4°C)	Liebherr, Bulle, Switzerland
See-saw rocker (SSL4)	Stuart Equipment, Staffordshire, United Kingdom
Small animal laryngoscope	Penn century, Wyndmoor, PA, USA
Sterile workbench	Heraeus, Braunschweig, Germany
Thermo cauter	Faromed, Berlin, Germany
Vacuum pump (AC)	HLC Biotech, Bovenden, Germany
Vortex	Bender & Hobein, Ismaning, Switzerland
Waterbath	Julabo GmbH, Seelbach, Germany

2.1.2.Consumables

Table 2: Consumables

Consumable	Company
96-well cell culture plates	VWR International GmbH, Darmstadt Germany
Corning Falcon test tubes with strainer cap	Thermo scientific GmbH, Schwerte, Germany
Diagnostic microscope slides, Teflon, 8 well	Thermo scientific GmbH, Schwerte, Germany
DNA ladder	New England BioLabs GmbH, Frankfurt, Germany
DNA Screening Cartridge	Qiagen, Hilden, Germany
FACS-Tubes	SARSTEDT AG + Co.,Nümbrecht, Germany
Falcontubes	SARSTEDT AG + Co.,Nümbrecht, Germany

Consumable	Company
Filtertips	SARSTEDT AG + Co.,Nümbrecht, Germany
IV indwelling cannula (blue) Introcan®-W	B. Braun Melsungen AG, Melsungen. Germany
Kodan® Tinktur Forte skin disinfectant	Schülke & Mayr GmbH, Norderstedt, Germany
Luer-lock single use cannula (black)	Henke-Sass, Wolf GmbH, Tuttlingen, Germany
Microplate 96-well, white	Greiner bio-one, Frickenhausen, Germany
Microscope slides	Paul Marienfeld GmbH & Co. KG, Lauda Königshofen, Germany
Microscopecover glasses	Paul Marienfeld GmbH & Co. KG, Lauda Königshofen, Germany
nCounter Cartridge	Nanostring, Seattle, USA
nCounter PrepPack	Nanostring, Seattle, USA
nCounter PrepPlates	Nanostring, Seattle, USA
Parafilm M	Sigma-Aldrich, St. Louis, MO, USA
Pipettetips	Starlab, Hamburg, Germany
Polyethylene Tubing (non-toxic, 0.58mm)	Becton, Dickinson and Company, Franklin Lakes, NJ, USA
Reaction tubes	Eppendorf AG, Hamburg, Germany
Reagent reservoir	Thermo scientific GmbH, Schwerte, Germany
Serological pipette	Corning, New York, USA
Silk suture 6-0	Ethicon, Raritan, USA
Single use syringe 1 ml	B. Braun Melsungen AG, Melsungen. Germany
Weighing pans	BRAND GMBH + CO KG, Wertheim, Germany

2.1.3.Chemicals and reagents

Table 3: Chemicals and reagents

Reagent	Company
17β-estradiol	Sigma-Aldrich, St. Louis, MO, USA
APC-eFluor780 Viability dye	Thermo Fischer Scientific, Waltham, MA, USA
CaliBRITE™ Beads (FITCS, APC, PerCP)	Becton, Dickinson and Company, Franklin Lakes, NJ, USA

Reagent	Company
Carprofen	Cp-Pharma, Hildesheim, Germany
Clodronate-Liposomes	Liposoma, AMSTERDAM, The Netherlands
Collagenase IV	Sigma-Aldrich, St. Louis, MO, USA
D-Luciferin, Sodium Salt	BioVision, Inc, Waltham, MA, USA
ddH_2O	Kurts Laboratory
Deoxyribonuclease I (DNAse I)	Sigma-Aldrich, St. Louis, MO, USA
Dihydrorhodamine 123	Thermo Fischer Scientific, Waltham, MA, USA
dNTPs	Promega, Mannheim, Germany
Estradiol ELISA	DRG Diagnostics, Marburg, Germany
Ethanol, absolute	Merck, Darmstadt, Germany
Ethylene diamine tetraacetic acid (EDTA)	Merck, Darmstadt, Germany
Fetal calf serum (FCS)	Life Technologies, Carlsbad, CA, USA
Formaldehyde, Methanol-free	Thermo Fischer Scientific, Waltham, MA, USA
FoxP3/Transcription factor staining kit	eBioscience, San Diego, CA, USA
Giemsa-Stammlösung	Roth, Karlsruhe, Germany
GoTaq®qPCR Master mix with SYBR green flourescence	Promega, Mannheim, Germany
H151	kindly provided by Andrea Ablasser (available at Invivogen)
Hemoglobin Assay Kit	Sigma-Aldrich, St. Louis, MO, USA
Heparin	Ratiopharm GmbH, Ulm, Germany
Human poly Ig Octagam 10%	Octapharma, Langenfeld, Germany
Iron Stain Kit	Abcam, Cambridge, UK
Isoflurane	Piramal Critical Care Limited, West Drayton, UK
Ketamin (10%)	Wirtschaftsgenossenschaft deutscher Tierärzte eG, Garbsen, Germany
Lipopolysaccharides (LPS) Serotype: O26:B6)	Sigma-Aldrich, St. Louis, MO, USA
Luciferase Assay System	Promega, Mannheim, Germany
Methanol (100%)	Roth, Karlsruhe, Germany

Reagent	Company
Moloney murine leukemia virus revers transcriptase	Promega, Mannheim, Germany
N-Formyl-Met-Leu-Phe (fMLP)	Sigma-Aldrich, St. Louis, MO, USA
PBS-Liposomes	Liposoma, AMSTERDAM, The Netherlands
Phosphate buffered saline (PBS)	Life Technologies, Carlsbad, CA, USA
Progesterone	Sigma-Aldrich, St. Louis, MO, USA
Progesterone ELISA	DRG Diagnostics, Marburg, Germany
Proteome Profiler Array Kit	R&D Systems, Minneapolis, USA
Quant-iT™ Pico Green™ dsDNA Assay Kit	Thermo Fischer Scientific, Waltham, MA, USA
RLT lysis buffer	Promega, Mannheim, Germany
RLT buffer	Qiagen, Hilden, Germany
RNasin	Promega, Mannheim, Germany
RNeasy Mini Kit	Qiagen, Hilden, Germany
Rompun® (2%)	Bayer Vital GmbH, Leverkusen, Germany
ROTI®Histokitt	Roth, Karlsruhe, Germany
Sesame oil	Sigma-Aldrich, St. Louis, MO, USA
Sodium azide (NaN3)	Roth, Karlsruhe, Germany
Ultracomp eBeads™ Compensation-Beads	Thermo Fischer Scientific, Waltham, MA, USA

2.1.4.Buffers, media, and solutions

Table 4: Buffers, media, and solutions

Buffer	Reagent
Collagenase IV	100 mg/ml in PBS
DNAse I	10 mg/ml in PBS
EDTA-Stock solution	0.5 M EDTA in ddH_2O, pH 8.0
FACS buffer	3% FCS, 0.1% NaN_3 in PBS
FACS blocking buffer	FACS buffer + 1.5% human poly Ig Octam
fMLP	100 mM in 0.2% DMSO/PBS

Buffer	Reagent
LPS	5 mg/ml (10.000 EU/mg) in ddH_2O
Phorbol myristate acetate (PMA)	1 mg/ml in H2O
Red cell removal buffer (RCB)	10 mM NH4Cl, 0.1 mM EDTA. 0.01 M $NaHCO_3$, pH 7.3

2.1.5.Antibodies

2.1.5.1.Antibodies for flow cytometry analysis

Table 5: Antibodies for flow cytometry analysis

Antibody	Clone	Isotype	Company
CD103	2E7	hamIgG	BioLegend, San Diego, USA
CD11b	M1/70	rIgG2b	Becton, Dickinson and Company, Franklin Lakes, NJ, USA
CD11c	N418	hamIgG	eBioscience, San Diego, CA, USA
CD19	6D5	rIgG2a	BioLegend, San Diego, USA
CD206	C068C2	rIgG2a	BioLegend, San Diego, USA
CD31	390	rIgG2a	BioLegend, San Diego, USA
CD326	G8.8	rIgG2a	BioLegend, San Diego, USA
CD3ε	17A2	rIgG2b	BioLegend, San Diego, USA
CD4	GK1.5	rIgG2b	Becton, Dickinson and Company, Franklin Lakes, NJ, USA
CD45	30-F11	rIgG2b	BioLegend, San Diego, USA
CD8α	53-6.7	rIgG2a	Becton, Dickinson and Company, Franklin Lakes, NJ, USA
F4/80	BM8	rIgG2a	BioLegend, San Diego, USA
Hoechst	33258	Dead cell marker	Thermo Fischer Scientific, Waltham, MA, USA
Ki-67	16A8	rIgG2a	BioLegend, San Diego, USA
Ly-6B2	7/4	rIgG2a	Bio-Rad, Hercules, CA, USA
Ly-6C	HK1.4	rIgG2c	BioLegend, San Diego, USA
Ly-6G	1A8	rIgG2a	BioLegend, San Diego, USA

Antibody	Clone	Isotype	Company
MHC-II	M5/114.15.2	rIgG2b	BioLegend, San Diego, USA
NK1.1	PK136	mIgG2a	BioLegend, San Diego, USA
Propidium Iodide			Sigma-Aldrich, St. Louis, MO, USA
Siglec-F	E-50-2440	rIgG2a	Becton, Dickinson and Company, Franklin Lakes, NJ, USA
TCRβ	H57-597	hamIgG	eBioscience, San Diego, CA, USA
TCR$\gamma\delta$	GL3	hamIgG	Becton, Dickinson and Company, Franklin Lakes, NJ, USA
TER-119	Ter-119	rIgG2b	BioLegend, San Diego, USA

2.1.5.2.Antibodies for *in vivo* treatment

Table 6: Antibodies for *in vivo* treatment

Antibody	Clone	Isotype	Company
anti-MPO	6D1	IgG2b	BioXcell, West Lebanon, USA
anti-MPO	6G4	IgG2c	BioXcell, West Lebanon, USA
anti-IFNAR-1	MAR1-5A3	IgG1	BioXcell, West Lebanon, USA
Isotype control	MOPC-21	IgG1	BioXcell, West Lebanon, USA

2.1.6.Mouse strains

Table 7: Mouse strains

Mouse Strain	Name	Description
C57BL/6J	BL6	Non-transgenic wild-type mice
B6.129S4-Ccr2tm1Ifc/J	CCR2$^{-/-}$	Animals lack CCR2 and therefore cannot release monocytes from the bone marrow
B6.129S-Cybbtm1Din/J	gp91phox$^{-/-}$	Animals can not produce any NADPH-oxidase dependent ROS
B6(Cg)-Tmem173tm1.2Camb/J	STING$^{-/-}$	Animals lack the transmembrane protein 173 (STING), which signals downstream of cGAS. Due to this deficiency, nucleic acid recognition through cGAS/STING is impaired.
from Rayk Behrendt	Δβ-Luc	Animals express luciferase reporter upon IFN-β production [182]

2.1.7.Software

Table 8: Software

Software	Company
BioRender	BioRender, Toronto, Canada
FACS Diva V6.1.1	Becton, Dickinson and Company, Franklin Lakes, NJ, USA
FlowJoTM 10.5.3	Tree star, Ashland, OR, USA
Graphpad Prism 8	GraphPad Software, La Jolla, CA, USA
Image Lab	Bio-Rad, Hercules, USA
Living Image® Software	PerkinElmer, Waltham, MA, USA
MagellanTM 6	Tecan Trading AG, Männedorf, Switzerland
nSolver 4.0	NanoString Technologies
Numbers	Apple, USA
Pages	Apple, USA
QIAxcel ScreenGel	Qiagen, Hilden, Germany
Quantstudio 5	Thermo Fischer Scientific, Waltham, MA, USA

2.2. Methods

2.2.1.Mouse handling

Female and male 8-12 week-old mice were used in this study. Mice were kept under specific pathogen-free (SPF)-conditions with five mice per cage in the house of experimental therapy (HET), University Hospital Bonn. One week before experiments, mice were transferred to the mouse facilities in our laboratories to avoid stress during the investigation. When C57BL/6J mice were used as a control group for knockout mice, they were bred in the same facility. When only C57BL/6J mice were used in experiments, they were bought from Charles River, Sulzfeld, -Germany, or bred in our facility, depending on the experiment. All animal experiments were approved by governmental committees (Landesamt für Natur, Umwelt und Verbraucherschutz (LANUV), NRW). As such, all studies were carried out under the projects Az. 81-02.04.2019.A174 and Az. 81-02.04.2020.A149.

2.2.2.Vaginal lavage

Vaginal lavage was collected daily, starting four days before vasculitis induction, to determine the estrus cycle phase of female mice. Unanaesthetized mice were firmly held, and the vagina was flushed with 75 µl PBS by pipetting on the vaginal opening and subsequent aspiration. Vaginal lavage was pipetted on diagnostic microscope slides with a Teflon field (Thermo Fisher) and air-dried. Afterwards, slides were fixed with methanol (100%) for 10 minutes at room temperature (RT) and stained with Giemsa (for detailed description, see section 2.2.22.). Slides were mounted using ROTI®Histokitt, and images were taken with an IX71 light microscope. Estrus cycle stage was then determined by cytology of vaginal lavage as previously described [183]. In brief, the estrus cycle can be divided into 4 phases: proestrus, estrus, metestrus, and diestrus. The proestrus phase is characterized by round nucleated epithelial cells. During the estrus stage, cytology displays dying non-nucleated epithelial cells that become folded. The next phase, metestrus, is cytologically characterized by a few infiltrating neutrophils together with nucleated and non-nucleated/folded epithelial cells. In the last phase, diestrus, cytology consists of neutrophils only. Each phase lasts about one day. Representative images of each phase are shown in Appendix Figure 34.

2.2.3.Ovariectomy

24 days before AAPV induction, female mice were anesthetized with 2-3% isoflurane in O_2. When mice did not react to pinching in the paws anymore, a small area of the lower back was shaved. Mice were placed on a 37°C warm heating mat to maintain body temperature. The shaved skin was disinfected, and a small incision was made on the dorsal side of the mice. Subsequently, an incision of the muscle layer was made on the left and right side of the backbone, the ovaries plus fat pad were pulled out, and the ovaries were cauterized. The fat pad was carefully pushed back into the mouse, and wounds were closed by sewing with a 6.0 surgical silk thread. Operated mice were placed in a new cage that was maintained warm until mice were fully awake again. Mice were treated with painkillers (Carprofen 4 mg/kg) on the day of operation and the following three days. ELISA confirmed the absence of hormones (estrogen and progesterone) in serum (see section 2.2.11.).

2.2.4.*In vivo* blocking treatment

For in vivo blockade of interferon receptor-1 (IFNAR-1), mice received 250 µg of IFNAR-1 antibody or the respective isotype control antibody via intraperitoneal (i.p.) injection every 2nd day, starting one day before AAPV induction (d-1) [184]. For in vivo blockage of STING, mice received 750 nmol of the small molecule inhibitor H151 in 200 µl PBS supplemented with 10% DMSO and 10% Tween-80 daily i.p., starting at d0 [97]. Prof. Andrea Ablasser kindly provided H151. Control mice received only vehicles.

2.2.5.Alveolar macrophage depletion

To deplete alveolar macrophages, mice were given 50 µl of Clodronate-Liposomes. Control mice received PBS-Liposomes (Liposoma, Netherlands) or PBS intratracheally (i.t.) [185] under isoflurane anesthesia two days before AAPV induction. For a detailed description of intratracheal application, see section 2.2.9..

2.2.6.Hormone supplementation

17β-estradiol (here referred to as estradiol or E2; 50 µg/ml) and progesterone (P4; 10 mg/ml) were diluted in sesame oil [186, 187]. Mice received 100 µl of hormone solution subcutaneously (s.c.) daily, starting four days before vasculitis induction until the day of final analysis. The injection site alternated between the neck, right flank, and left flank.

2.2.7.Pulse Oximetry

To quantify blood SpO_2 (%), mice were anesthetized with 2-3% isoflurane in air. Hind-leg was shaved, and an oximeter sensor was placed on the thigh. SpO_2 was measured using MouseOx™ Pulse-oximeter (Starr Life Science) each second for 3-5 min, and values were averaged. Measurements were performed by Dr. Susanne F. Viehmann.

2.2.8.*In vivo* luminescence quantification

To quantify *in vivo* luminescence in IFN-β reporter mice (Δβ-Luc mice) before AAPV induction and before killing on day 3, 4.5 mg D-luciferin was injected in 150 µl PBS i.p.. Mice were anesthetized with 2-3% isoflurane in O_2 and placed in an IVIS Lumina III pre-warmed at 37°C. Quantification of luminescence was started 5 minutes later. Sequential pictures of decreasing exposure time were acquired, and the time point at which there was no signal saturation for all mice was selected for quantification. The following machine settings were used: Field of view: 12.5; Binning factor: 4; emission filter: open; excitation filter: blocked; filter position: 1.

2.2.9.Vasculitis induction

For vasculitis induction, mice were anesthetized with 2-3% isoflurane in O_2 on day 0. Mice were fixed on an intubation platform (Harvard Apparatus) and intubated with the help of a laryngoscope for small animals and a 22G (0.9 x 25 mm) butterfly cannula. Mice were then ventilated using a MicroVent ventilator (Harvard Apparatus) with 2-3% isoflurane and O_2 at 250 µl air/stroke and 250 strokes/minute. Then, 10 µg fMLP and 10 µg LPS were applied intratracheally (i.t.) in 50 µl PBS through

the cannula. Mice were further ventilated for 30 seconds (sec) to evenly distribute the compounds throughout the lung before removing the cannula. 1 mg total anti-MPO antibodies (clone 6G4 and 6D1, each 0.5 mg) were diluted in 200 µl PBS and injected i.p.. Control groups were left untreated or received only the anti-MPO antibodies i.p., respective isotype controls, or only fMLP+LPS i.t., as indicated in the respective Results section. Mice's well-being was visually monitored and by weighing daily.

2.2.10.Organ sampling

Mice were painlessly killed by an overdose of Rompun/Ketamin. For this, 200 µl of 10% Rompun and 10% Ketamin in PBS were injected i.p. per mouse. To sample the bronchoalveolar fluid, mice were opened on the ventral side, and the lungs and the heart were exposed by opening the ribcage carefully. Blood was taken from the heart using a heparinized syringe, collected in an Eppendorf tube, and maintained on ice until further isolation of plasma (see section 2.2.11.). Afterwards, mice were tracheostomized by exposing the trachea, removing the muscle layer, and making a small incision below the cricoid cartilage. Bronchoalveolar lavage fluid (BALF) was taken by intubating the trachea with a self-made tubing made from a needle and 0.58 mm diameter polyethylene tubing. Lungs were then flushed thrice with 1 ml PBS + 2 mM EDTA each. Depending on the downstream assay, BALF was handled differently, as described in the respective Methods subsections.

Lungs were collected after collecting the BALF. For histological analysis, lungs were slowly filled with 1 ml 4% paraformaldehyde (PFA), stored at 4°C in 4% PFA overnight, and further processed as described in section 2.2.12.. For analyzing gene expression, lungs were removed, frozen in liquid nitrogen, and stored at -80°C until further processing (see section 2.2.13.). For flow cytometric analysis, lungs were dissected and digested using 1 mg/ml collagenase IV (1x) and 100 U/ml DNase I for 30 minutes at 37°C with occasional mixing until fully digested. Afterwards, samples were filtered through a 5 ml polystyrene tube equipped with a 35 µm cell strainer cap (Thermo Scientific). Samples were centrifuged for 5 minutes at 1600 rpm, and red blood cells were lysed for 10 mins at RT using RCB lysis buffer. Cells were washed with PBS and surface stained, as described in section 2.2.17..

2.2.11.Plasma isolation and hormone quantification

Plasma was isolated by centrifuging whole blood for 10 mins at 14000 rpm. Plasma was transferred to a new tube and centrifuged for 10 mins at 14000 rpm. Plasma was transferred to a new tube and stored at -20°C until further use. 17β-estradiol (E2) and progesterone (P4) concentrations were quantified by ELISA according to the manufacturer's description (Estradiol or Progesterone ELISA, DRG).

2.2.12. Lung histology

PFA-fixed lungs were sent to Prof. Peter Boor (Institute of Pathology, University Hospital Aachen) for processing and analysis. H&E staining was performed on 1 µm thick microtome sections in paraffin, and slides were scanned using a bright-field scanner (Aperio AT2, Leica) at 40x magnification. Blinded histopathological scoring was performed as previously described [188, 189]. In brief, samples were scored according to three parameters: immune cell infiltration, tissue destruction, and the number of lobes affected. Hemorrhage involvement was not included. Scores were: 0 (no inflammation), normal lung structure; 1 (slight), very few and only focal inflammatory cells on vessel walls, no or minimal tissue destruction; 2 (medium), few cells in airspace with small areas of tissue destruction; 3 (strong), large areas with inflammatory infiltrates and tissue destruction, up to one lobe involved; 4 (extensive), as 3 but involving more than 1 whole lobe.

2.2.13.Gene expression analysis in lung tissue

mRNA isolation from frozen lungs and gene expression quantification was kindly performed by our collaboration partners, Dr. Hella Luksch and Prof. Angela Rösen-Wolff (University Hospital Dresden), as previously described [190]. RNA was extracted using RNeasy Mini Kit (Qiagen, Hilden, Germany). 2 µg RNA were transcribed (Promega, Mannheim, Germany) according to the manufacturer's instructions. qPCR was prepared using GoTag®qPCR Master Mix with SYBR green fluorescence (Promega, Mannheim, Germany). Quantitative real-time PCR was performed using Quantstudio 5 (Thermo Fisher Scientific, Berlin, Germany). Gene expression was normalized to the housekeeping gene using the ΔΔCt method for

comparing relative expression. Primer sequences: *Ifn-β* Forward: 5'-TCC GAG CAG AGA TCT TCA GGA A-3; *Ifn-β* Reverse: 5'-TGC AAC CAC CAC TCA TTC TGA G-3'.

2.2.14.Hemoglobin quantification in BALF

150 µl of BALF was taken and diluted 1:2 and 1:4 in PBS + 2 mM EDTA in a 96 flat-bottom plate to obtain non-saturated measurements. Hemoglobin absorbance was quantified at 400 nm with subtraction of background at 670 nm using an absorbance reader (Tecan). PBS + EDTA served as blank. Afterwards, background absorbance and blank were subtracted from samples, and dilution factors were calculated. Additionally, hemoglobin concentration was quantified using a colorimetric assay (Sigma). Because colorimetric quantification correlated strongly with optical density quantification (R=0.98) (see Appendix Figure 36), we continued using only optical density for hemoglobin quantification.

2.2.15.Extracellular DNA quantification in BALF

100 µl supernatant of the first BALF lavage was taken to quantify extracellular DNA. Samples were transferred to a 96-well plate, and DNA was quantified according to the manufacturer's instructions (Quant-iTTM Pico GreenTM dsDNA Assay Kit, Thermo Fisher Scientific). In brief, DNA standards and samples were incubated with Quant-iTTM PicoGreenTM dsDNA Reagent for 2 min in the dark at room temperature. Fluorescence intensity was quantified using a plate reader (Tecan) with an excitation wavelength of 480 nm and an emission wavelength of 520 nm.

2.2.16.Cytokine quantification of BALF

To quantify cytokines in BALF of mice with AAPV, we used a Proteome Profiler Array (R&D) according to the manufacturer's description. In brief, membranes were blocked by shaking for one hour at RT and afterwards incubated with 200 µl supernatant of the first BALF lavage overnight at 4°C under shaking. Membranes were washed with the provided washing buffer three times for 10 mins at RT and then incubated with detection antibody for one hour, shaking at RT. Membranes were washed and incubated with horseradish peroxidase (HRP) for 30 mins at RT,

shaking. Membranes were covered with chemiluminescence reagent and incubated for one minute. The excessive reagent was removed, and membranes were imaged using ChemiDoc XRS+ System (Bio-Rad) with an exposure time of 60 seconds. Intensities were quantified using Image Lab Software (Bio-Rad).

2.2.17.Flow cytometry analysis

Flow cytometry was performed as previously described [191, 192]. Briefly, cell pellet of BALF or lungs was resuspended in fluorescence-activated cell scanning (FACS) blocking buffer, and 10% volume was transferred to a 96-well plate for staining. The plate was centrifuged for 5 min at 1600 rpm, 4°C, to pellet the cells, and the supernatant was removed. Cells were resuspended in 50 µl antibody mixture diluted in FACS blocking buffer. Cells were stained on ice for 20 minutes in the dark. Afterwards, the plate was centrifuged, the supernatant removed, and cells washed in 150 µl FACS buffer to remove unbound antibodies. After centrifugation, the supernatant was removed, and cells were resuspended in FACS buffer containing the live/dead marker HOECHST33258 (1:10,000) and 5,000 CaliBRITE™ counting beads per well (BD). Cell acquisition was performed using the LSR Fortessa with DiVa software v9.0.1 (BDBiosciences). The gating strategy for cell identities is shown in Appendix Figure 35. Analysis was performed in FlowJo v10 (TriStar).

For compensation, Ultracomp eBeads (Thermo Fisher Scientific) were used. Beads were stained and treated as described for samples, but each sample with only a single antibody.

For intracellular staining, samples were first stained with Zombie UV fixable viability dye (1:2,000) in PBS for 30 minutes on ice. Excess viability dye was washed out twice with PBS. Surface staining with antibody master mix diluted in FACS blocking buffer was performed for 30 mins on ice in the dark. Samples were washed and fixed using Fix/Perm solution (Foxp3 transcription factor staining kit, eBioscience) for 30 minutes at room temperature. Samples were washed in 1x Perm buffer (eBioscience) and intracellularly stained for Ki-67 or CD206. After 60 minutes of

incubation at RT, samples were washed twice in Perm buffer, resuspended in FACS buffer containing counting beads, and acquired immediately.

Uniform Manifold Approximation and Projection for Dimension Reduction (UMAP) plug-in in FlowJo v. 10.6.1 was used to perform dimensionality reduction of flow cytometric data. Prior to UMAP, data was cleaned using the FlowAI plug-in in FlowJo, and samples were concatenated. Doublets and dead cells were excluded before UMAP. Specific cell populations were identified by standard gating, as shown in Appendix Figure 35.

2.2.18.ROS staining

To quantify reactive oxygen species (ROS), cells were cell-surface stained first, as described in 2.2.17. and then incubated with dihydrorhodamine 123 (DHR123) for 30 mins at 37°C following the manufacturer's instructions. Positive control for ROS production was treated with 1 µg/ml phorbol myristate acetate (PMA) for 30 mins at 37°C before ROS staining.

2.2.19.Cell sorting

Mice were painlessly sacrificed, and lungs were dissected and digested, as described in section 2.2.10. Cells were surface stained to identify the populations of interest to be sorted using BD FACSMelody or BD FACSAria cell sorter.

2.2.20.*Ex vivo* luminescence quantification of sorted cells

In order to identify IFN-β production in different cell populations, macrophages, neutrophils, eosinophils, endothelial cells, epithelial cells, and lymphoid cells identified as shown in Appendix Figure 37 were sorted from lungs of Δβ-Luc mice three days after disease induction. Naive mice served as control. Depending on the experiment, an equivalent number of cells ranging from 62,500 to 500,000 was plated in a white 96-well plate and lysed by incubation with 20 µl passive lysis buffer (Promega) for 5 mins on a rocking plate. Afterwards, 100 µl of luciferase substrate (Promega) was added per well, and luminescence was acquired for 10,000 ms using a Tecan plate reader.

2.2.21.NanoString

Classical and Siglec-F$^+$ neutrophils were sorted from the lungs of C57BL/6J mice six days after AAPV induction (as described in 2.2.19.). 250,000 sorted cells were resuspended in 8 µl PBS and lysed by adding 4 µl RLT buffer (Qiagen, Hilden). Cells were vortexed for one minute, and cell lysates were either used fresh or stored at -20°C for seven days before use. For NanoString analysis, fresh or thawed lysates were used, and hybridization was prepared as described in the manufacturer's guide. Hybridization was conducted for 24 h at 65°C, and samples were afterwards cooled down at 4°C and analyzed immediately. The "Immunology panel" from NanoString was used, which analyzes 317 genes associated with immunologic processes and pathways. Dr. Fraser Duthie (University Hospital Bonn) kindly performed NanoString analysis. Further detailed quantification was performed using nSolver 4.0 software. Quality control was performed by excluding counts below the detection limit (threshold set to 20) and normalizing samples to six positive controls and 14 housekeeping genes. Pathway scores were automatically calculated in the nSolver software and were derived from the first Principle Components Analysis (PCA) scores.

2.2.22.Preparation and staining of cytospins

The population of interest was sorted as described in section 2.2.19.. To spin cells on a glass slide, cells were resuspended in 50% FCS in PBS, and 200 µl containing about 100,000 cells were loaded in a cytospin chamber. Chambers were centrifuged for 3 min at 800 rpm at RT. Glass slides were removed, air-dried, and stored at RT until further use.

For Giemsa staining, cells on cytospins were surrounded with a Dako Pen (Agilent Dako, USA) to avoid liquid leakage during the fixation/staining process. Cells were then fixed for 10 min with 100% methanol, washed in ddH2O, and stained with 20% Giemsa in ddH_2O for 20 min. Excess stain was removed by washing the slides in ddH2O. Slides were mounted and analyzed using a light microscope (IX71, Olympus).

For iron staining, a Prussian blue stain (Iron Stain Kit, Abcam) was used according to the manufacturer's description. In brief, slides were incubated with iron stain for 3 minutes, washed in ddH_2O, and afterwards counterstained in nuclear fast red for 5 mins and washed in distilled water again. Slides were mounted and analyzed using a light microscope (IX71, Olympus).

2.2.23.Statistical Analysis

Statistical analysis was performed with Graphpad Prism software v9. Mann-Witney student's *t*-test was used to compare two groups. One- or two-way ANOVA was used when comparing 3 or more groups with Tukey's multiple comparisons test. Statistical significance was marked as follows: * $p<0.05$; ** $p<0.01$; *** $p<0.001$.

3. Results

3.1. Development of a novel mouse model for ANCA-associated vasculitis in the lung

3.1.1. Combination of fMLP, LPS, and anti-MPO IgGs induce pulmonary vasculitis

We have developed a novel mouse model that mimics clinical disease hallmarks to investigate the underlying mechanisms driving ANCA-associated pulmonary vasculitis (AAPV). In patients, vasculitis surges are often preceded by bacterial infections [193]. Therefore, we applied low doses of the bacterial ligands fMLP and LPS intratracheally together with intraperitoneal administration of two mouse monoclonal antibodies directed against murine MPO (clone 6D1 and 6G4) [83, 189] (Figure 7, A). Within three days, mice had a decrease in well-being indicated by a weight loss of up to 20% of their initial body weight (Figure 7, B) and a decreased survival rate (Figure 7, C), which were not observed in naive mice or mice treated only with anti-MPO IgGs. Mice treated only with fMLP+LPS underwent moderate and transient weight loss. Additionally, combination of fMLP+LPS and anti-MPO reduced lung function as quantified by peripheral blood oxygenation (Figure 7, D). AAPV induction also increased lung pathology (Figure 7, E and F) from day one after induction (Figure 7, G). Furthermore, mice with AAPV developed severe pulmonary hemorrhages quantified by the optical density of hemoglobin in the BALF (Figure 7, H and I), peaking by days 1 to 3 (Figure 7, J and K). Hemorrhages were macroscopically visible (Figure 7, L) and were specific to the combinatory treatment as none of the control groups developed them at any time (Figure 7, H and I). Optical density of hemoglobin (Hb) was the method of choice for hemorrhage quantification as it directly correlated with Hb quantification by a colorimetric assay (Sigma) (Appendix Figure 35). Although fMLP+LPS treatment induced a degree of lung pathology (Figure 7, E), it was to a lesser extent than that in mice undergoing AAPV; notably, it did not result in lung bleeding (Figure 7, H). Surviving mice with AAPV recovered most of their original weight by day 7 (Figure 7, B) when they displayed reduced lung hemorrhages (Figure 7, I-K). Together, this model reflects severe pulmonary involvement in patients with AAPV.

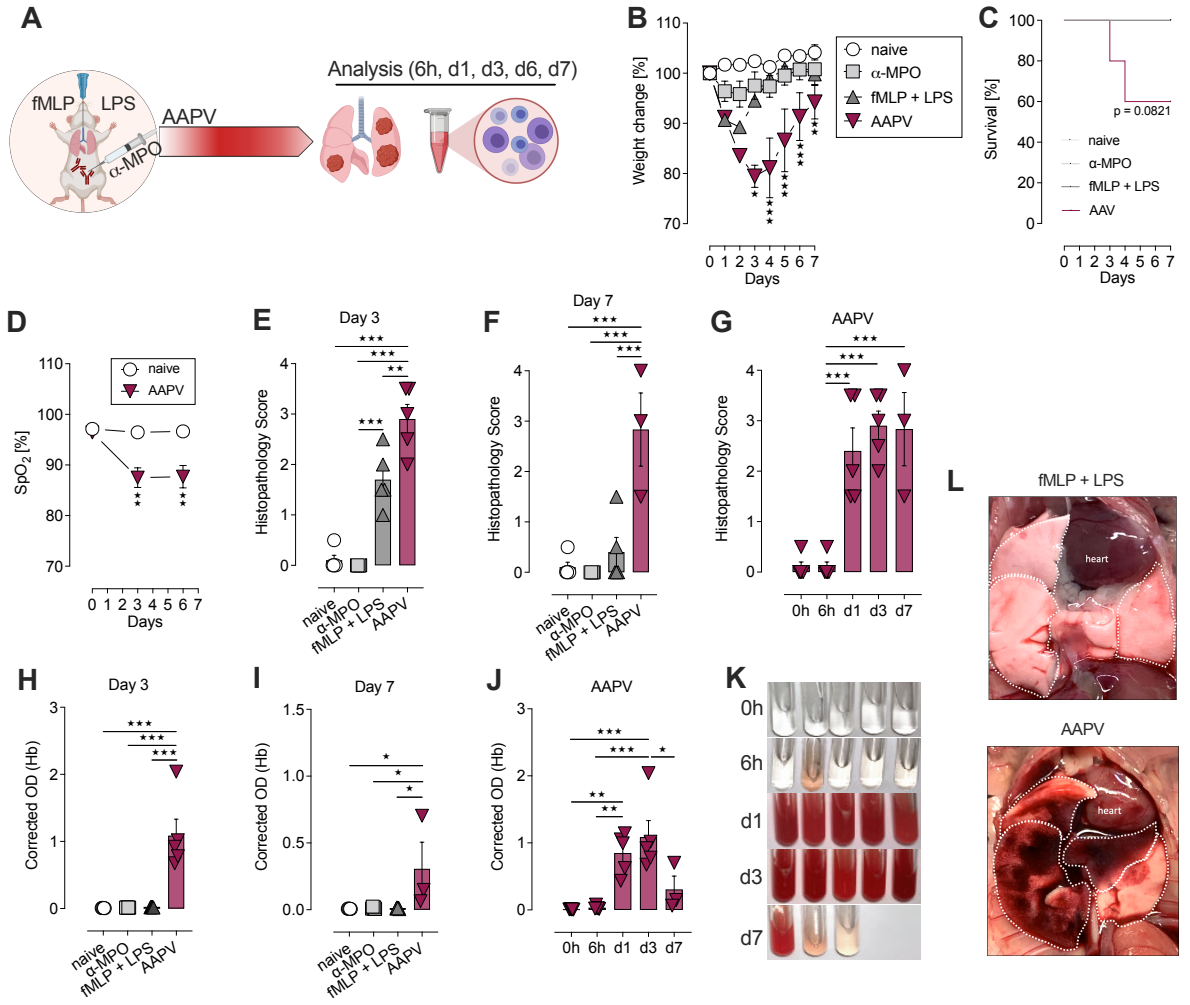

Figure 7: Combination of fMLP, LPS, and anti-MPO IgGs induce pulmonary vasculitis. (**A**) Schematic representation of experimental setup. On day 0, female mice were given either 10 µg fMLP + 10 µg LPS in 50 µl PBS i.t, 1 mg anti-MPO antibody i.p. (0.5 mg of each clone 6D1 and 6G4), or their combination (AAPV group). (**B**) Weight changes over time. (**C**) Survival over time. (**D**) Peripheral blood oxygen (SpO_2) saturation over time. (**E-G**) Histopathology score of the lung from the indicated treatments at day 3 (E) at day 7 (F) and of mice with AAPV over time (G). (**H-J**) Hemoglobin quantification in bronchoalveolar lavage fluid from the indicated treatments on day 3 (H) on day 7 (I) and of mice with AAPV over time (J). (**K**) Representative images of bronchoalveolar lavage fluid of mice with AAPV at the indicated time points. (**L**) Representative images of lungs of fMLP+LPS and AAPV-treated mice at day 3. The data shown represent 2 (C-G) or more than 5 experiments (B, H-L). Mean ± SEM; each symbol represents a mouse. One-way ANOVA, *p<0.05; **p<0.01; ***p<0.001. The experiment was performed with the assistance of Dr. Susanne F. Viehmann, University of Bonn.

3.1.2. Immune cell infiltration in the bronchoalveolar space during AAPV disease

To identify which cell types may be involved in disease pathogenesis, we characterized the cellular compartment during disease progression in the bronchoalveolar space (BAS) as a surrogate for infiltration into the lung [194]. For this, mice were treated either with anti-MPO, fMLP+LPS, or their combination (AAPV), and immune cells in the bronchoalveolar lavage fluid (BALF) were quantified after 6 hours and after 1, 3, or 7 days. Standard, as well as Uniform Manifold Approximation and Projection (UMAP) analyses, demonstrated that anti-MPO treatment alone did not provoke immune cell infiltration, with most of the cells being resident alveolar macrophages (AMs) as in naive untreated mice (Figure 8, A and B). In contrast, fMLP+LPS or AAPV treatment resulted in a rapid influx of immune cells, although the latter resulted in an over 2-Log higher increase at the peak of infiltration (Figure 8, A and B).

Within 6 hours after disease induction, neutrophils had infiltrated the bronchoalveolar space of mice undergoing AAPV and to a similar level in mice treated with only fMLP+LPS (Figure 8, C). AAPV induction resulted in a further increase, with neutrophils peaking at day 3 when they dominated the cellular infiltrate, followed by a decline in their numbers by day 7 when mice were recovering from lung hemorrhages. A similar pattern was observed for other myeloid cells like eosinophils (Figure 8, D) and monocytes (Figure 8, E). Interestingly, tissue-resident alveolar macrophage (AM) numbers initially decreased upon administration of fMLP+LPS, independently of anti-MPO injection. However, their numbers progressively recovered and increased around 10-fold in mice with AAPV by day 7 (Figure 8, F). We observed another macrophage population infiltrating the bronchoalveolar space from day 3 after disease onset, which remained at least until day 7. Although to a lesser extent, this population was also present upon fMLP+LPS treatment (Figure 8, G). These macrophages were *Ccr2*-dependent, indicating a monocytic origin, and will be further discussed in Results section 3.3.1..

When investigating the lymphoid compartment infiltrating the BAS, we quantified a more than 10-fold increase in NK cells (Figure 8, H) and B cells (Figure 8, I) one day after AAPV induction that lasted for at least 7 days. Conventional T cell counts also

increased, although this was specific to fMLP+LPS treatment, with only a minor increase due to AAPV progression (Figure 8, J). Altogether, AAPV provoked a stronger immune cell infiltration than fMLP+LPS treatment, which was dominated by neutrophils and macrophages.

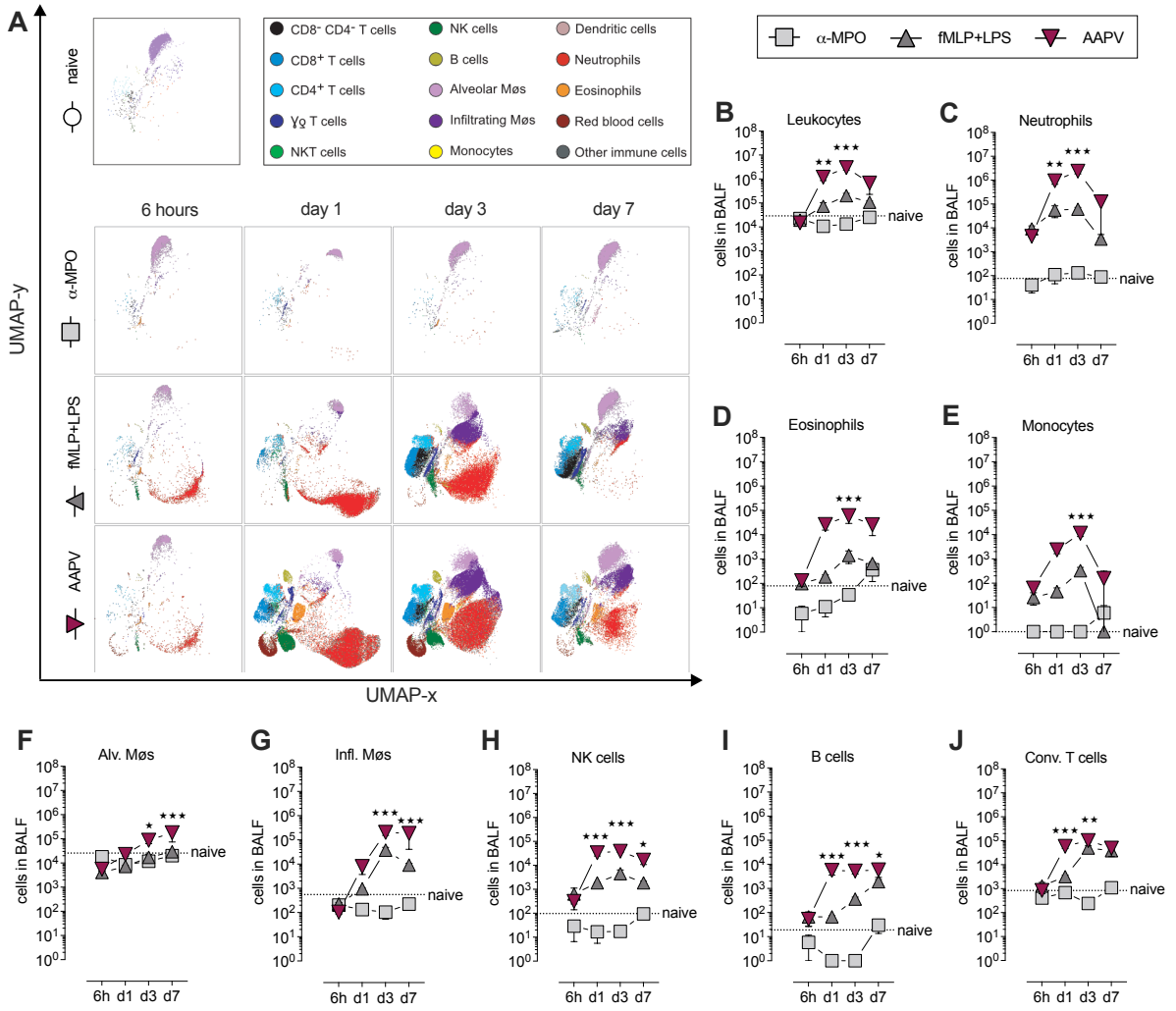

Figure 8: Immune cell infiltration in the bronchoalveolar space during AAPV disease. On day 0, female mice were given either 10 µg fMLP + 10 µg LPS in 50 µl PBS i.t, 1 mg anti-MPO antibody i.p. (0.5 mg of each clone 6D1 and 6G4), or the combination. Mice were painlessly killed after 6 hours and 1, 3, and 7 days later. Bronchoalveolar lavage fluid was taken, and specific immune cells were quantified by flow cytometry. (**A**) UMAP analysis was performed using FlowJo software. (**B-J**) Quantification of immune cell populations overtime of the indicated groups - leukocytes (B), neutrophils (C), eosinophils (D), monocytes (E), alveolar macrophages (Møs) (F), infiltrating macrophages (G), NK cells (H), B cells (I) and conventional T cells (J). Dotted line indicates cell numbers in untreated naive mice. Gating strategy for cell identities is shown in Appendix Figure 35. Shown is a representative of at least 3 independent experiments with 5 mice per group. Mean ± SEM; each symbol represents a mouse. One-way ANOVA, *p<0.05; **p<0.01; ***p<0.001. For simplicity, only statistically-significant changes in AAPV compared to fMLP+LPS are indicated. The experiment was performed with the assistance of Dr. Susanne F. Viehmann, University of Bonn.

3.1.3.Identification of Siglec-F$^+$ neutrophils in AAPV disease

Neutrophils express high levels of MPO, the target of the antibodies used in this study and one of the main targets considered to drive clinical ANCA-associated vasculitis [85]. Although the exact mechanism underlying the clinical phase of AAV remains to be elucidated, several studies have demonstrated that neutrophils are required for disease pathogenesis [23]. Having seen a major contribution of neutrophils to the cellular infiltrate upon AAPV induction (Figure 8, A and C), we aimed to characterize neutrophils phenotypically as well as functionally. Therefore, we initially investigated the phenotype of polymorphonuclear leukocytes (PMNs) in the bronchoalveolar lavage of mice with AAPV (Figure 9, A). As expected, we identified classical Ly-6G$^-$ Siglec-F$^+$ eosinophils and classical Ly-6G$^+$ Siglec-F$^-$ neutrophils by flow cytometry (Figure 9, B). Surprisingly, we also identified a major Ly-6G and Siglec-F double-positive population infiltrating the lung after disease induction (Figure 9, B). Siglec-F$^+$ Ly-6G$^+$ cells displayed similar size and granularity as classical neutrophils identified by forward scatter (FSC) / sideward scatter (SSC) using FACS (Figure 9, C). This was distinct from eosinophils, which had a higher granularity (Figure 9, C). Morphological analysis of these populations using Giemsa staining after FACS sorting revealed that Siglec-F$^+$ Ly-6G$^-$ cells contained eosinophilic granules and a less segmented nucleus that are characteristic of eosinophils (Figure 9, D, left panel). In contrast, Siglec-F$^-$ Ly-6G$^+$ cells had the neutral cytoplasm and polymorphic nucleus characteristic of classical neutrophils (Figure 9, D, middle panel). Siglec-F$^+$ Ly-6G$^+$ cells contained neutral granules resembling neutrophils, albeit with a more condensed nucleus revealed by Giemsa staining (Figure 9, D, right panel). Thus, hereafter these double-positive cells are named Siglec-F$^+$ neutrophils. Chromatin condensation is a hallmark of neutrophil maturation [195], suggesting Siglec-F$^+$ neutrophils are terminally differentiated.

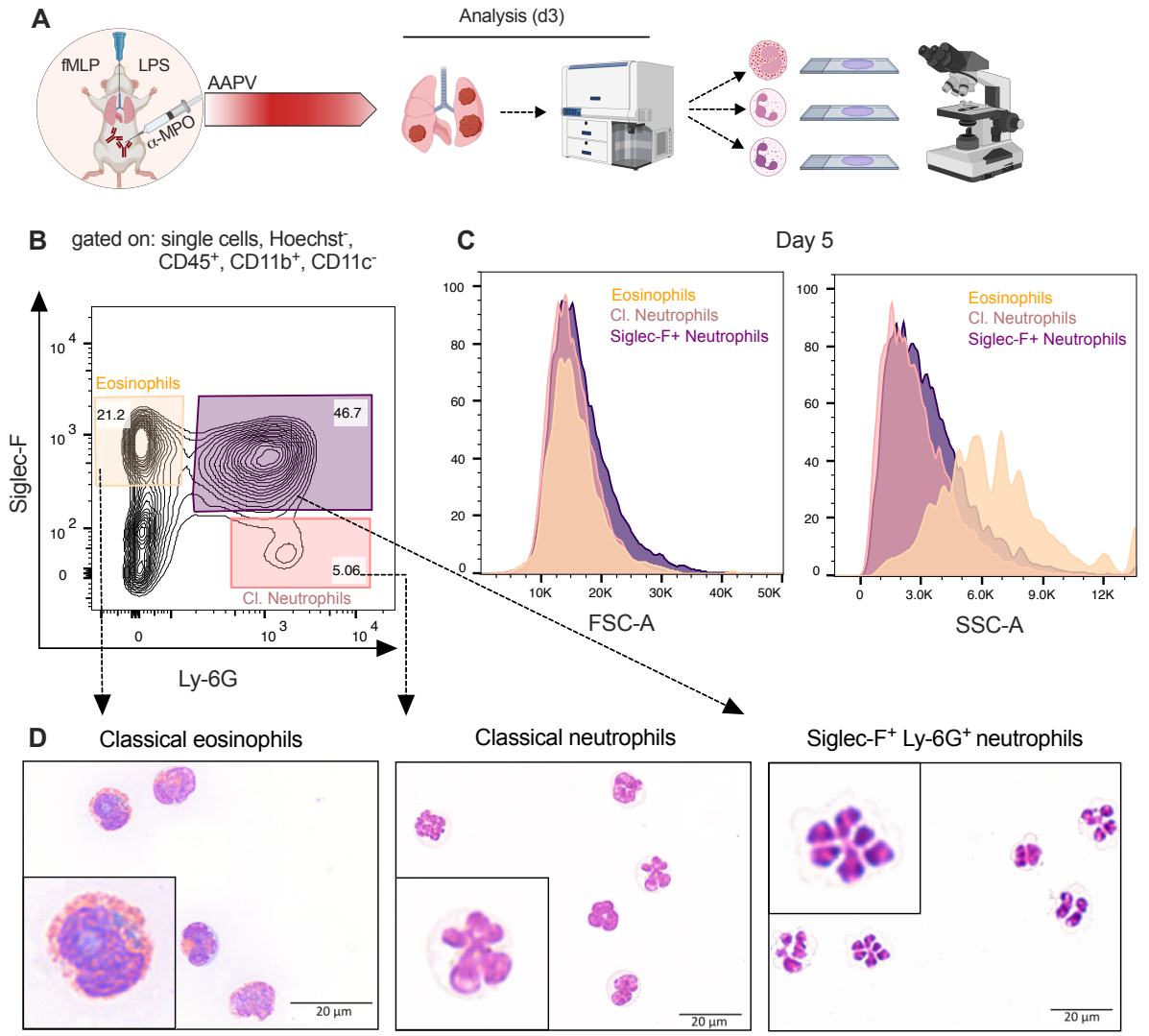

Figure 9: Identification of Siglec-F⁺ neutrophils in AAPV disease. (**A**) Schematic representation of experimental setup. On d0, AAPV was induced in female C57BL/6J mice by applying 10 µg fMLP + 10 µg LPS in 50 µl PBS i.t. and 1 mg anti-MPO antibody i.p. (0.5 mg of each clone 6D1 and 6G4). The mice were painlessly killed five days later, and the bronchoalveolar lavage fluid was collected. FACS analysis was performed, and the indicated PMN populations were sorted. Afterwards, cytospins were made and stained with Giemsa. Cytospins were analyzed using a light microscope. (**B**) FACS sorting gates of the cells of interest as indicated. (**C**) FSC and SSC FACS histogram of PMNs. (**D**) Representative images of Giemsa staining of sorted populations spun on glass slides and zoom in. Scale bar = 20 µm. Data is representative of two independent experiments. The experiment was performed with the assistance of Ms. Karola Mai, University of Bonn.

3.1.4.Neutrophils up-regulate Siglec-F in the lung environment

Having identified a phenotypically distinct neutrophil subset with unconventional expression of Siglec-F, we aimed to characterize this subset in detail. First, we investigated whether Siglec-F$^+$ neutrophils are specific to the lung environment of mice with AAPV and develop throughout the disease course or whether they are already present in the systemic circulation (Figure 10, A). Detailed analysis of Siglec-F$^+$ neutrophil abundance in the lung during AAPV revealed that in the initiation phase of the disease up to day 1, classical neutrophils were more prevalent than Siglec-F$^+$ neutrophils (Figure 10, B and D). However, Ly-6G$^+$ neutrophils seemed to up-regulate Siglec-F at the disease peak (day 3) (Figure 10, B), leading to a predominance of Siglec-F$^+$ neutrophils during the recovery phase at day 7 (Figure 10, B and D). In contrast, fMLP+LPS treatment alone did not result in a clear expression of Siglec-F by neutrophils at any time point (Figure 10, B and C).

To elucidate whether Siglec-F was up-regulated by neutrophils already in systemic circulation, we stained neutrophils in the blood throughout the disease course. Siglec-F$^+$ neutrophils were not detectable in blood 1 or 5 days after AAPV induction (Figure 10, E and F), suggesting that classical neutrophils up-regulated Siglec-F as they terminally differentiated in the lung. Additionally, we observed cytopenia of classical neutrophils by day 5 in the blood (Figure 10, F), which is also observed in patients with ANCA-associated vasculitis [196]. Although the underlying mechanism remains to be elucidated, our data indicate that Siglec-F is up-regulated on neutrophils upon recruitment into the inflamed lung.

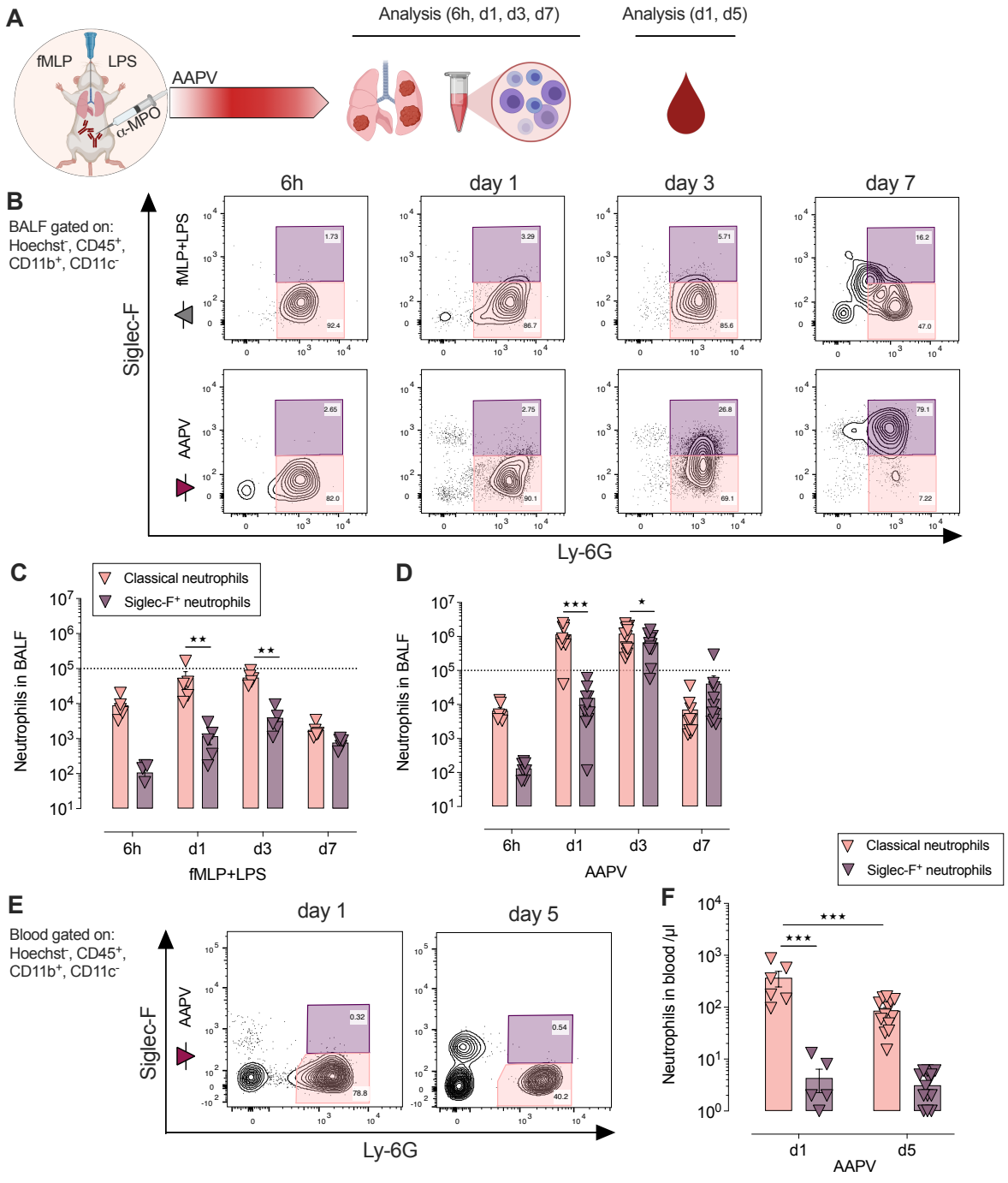

Figure 10: Neutrophils up-regulate Siglec-F in the lung environment. (**A**) Schematic representation of experimental setup. On d0, mice were treated with 10 µg fMLP + 10 µg LPS in 50 µl PBS i.t. with or without injecting 1 mg anti-MPO antibody i.p. (0.5 mg of each clone 6D1 and 6G4). 6 hours and 1, 3, 5, or 7 days later, mice were painlessly killed, blood and bronchoalveolar lavage fluid were collected, and neutrophils were quantified by FACS. (**B**) Representative FACS plots of PMNs in BALF of fMLP+LPS and mice with AAPV at the indicated time points. (**C** and **D**) Neutrophil counts in BALF of fMLP+LPS treated mice (C) and mice with AAPV (D) after 6 hours, 1, 3, and 7 days after disease induction. (**E**) Representative FACS plots of PMNs in the blood of mice with AAPV at the indicated time points. (**F**) Neutrophil counts in mice with AAPV in blood 1 and 5 days after disease induction. Pooled data from two independent experiments (B-D) and representative data (E and F). Mean ± SEM; each symbol represents one mouse. Two-way ANOVA, *p<0.05; **p<0.01; ***p<0.001.

3.1.5. Siglec-F$^+$ neutrophils acquire a distinct transcriptomic profile indicating terminal differentiation

In the microscopical analysis of the two neutrophil subsets, the chromatin of Siglec-F$^+$ neutrophils appeared to be more condensed than that of classical neutrophils (Figure 9, D), suggesting lower transcriptional activity and a terminally differentiated phenotype. Therefore, we investigated whether classical and Siglec-F$^+$ neutrophils exhibit distinct gene expression profiles. For this purpose, we analyzed mRNA expression using NanoString analysis 6 days after disease induction (Figure 11, A). Out of 317 analyzed genes, 123 differentially expressed genes in Siglec-F$^+$ neutrophils compared to classical neutrophils reached statistical significance. Of those, 107 genes were down-regulated while only 16 were up-regulated, demonstrating a lower transcriptional activity in Siglec-F$^+$ neutrophils compared to their classical counterparts in the selected list of genes investigated (Figure 11, B). *Camp*, *Bcl6*, *Il-15,* or *Il-33* were amongst the top ten down-regulated genes in Siglec-F$^+$ neutrophils (Figure 11, C; complete list in Appendix Table 9). LL-37, which is encoded by *Camp,* controls the release of inflammatory mediators, and BCL6 mediates anti-apoptotic properties and is important for neutrophil survival, whereas IL-15 and IL-33 are involved in activating other immune cells like T cells, NK cells, or eosinophils. Within the up-regulated genes in Siglec-F$^+$ neutrophils, *Cdkn1a*, and *Ski*, were amongst the top ten (Figure 11, D; complete list in Appendix Table 10), which are potent suppressors of NETosis [197] and ROS production [198], respectively.

Further pathway analysis revealed that genes associated with response to DNA damage or nuclear matrix were up-regulated in Siglec-F$^+$ neutrophils. In contrast, pathways related to anti-apoptosis, inflammatory response, or cytokine activity were down-regulated (Figure 11, E).

Consistently with the temporal dynamics of classical and Siglec-F$^+$ neutrophils, these results suggest that classical neutrophils contribute relatively more to the inflammatory phase of the disease, whereas Siglec-F$^+$ neutrophils have fulfilled their effector function and reached the end of their lifespan as they down-regulate genes associated with cytokine pathways and anti-apoptosis.

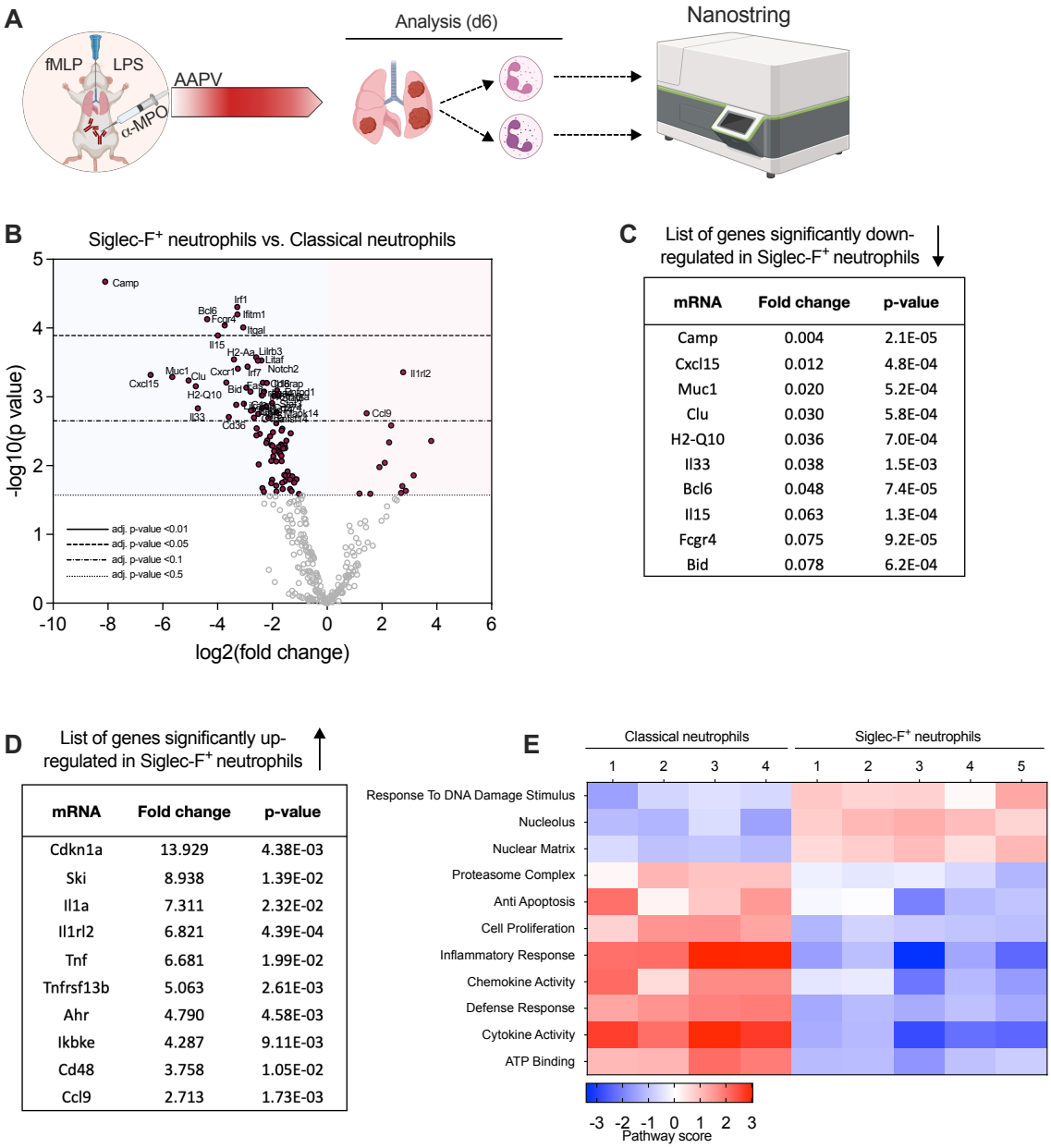

mRNA	Fold change	p-value
Camp	0.004	2.1E-05
Cxcl15	0.012	4.8E-04
Muc1	0.020	5.2E-04
Clu	0.030	5.8E-04
H2-Q10	0.036	7.0E-04
Il33	0.038	1.5E-03
Bcl6	0.048	7.4E-05
Il15	0.063	1.3E-04
Fcgr4	0.075	9.2E-05
Bid	0.078	6.2E-04

mRNA	Fold change	p-value
Cdkn1a	13.929	4.38E-03
Ski	8.938	1.39E-02
Il1a	7.311	2.32E-02
Il1rl2	6.821	4.39E-04
Tnf	6.681	1.99E-02
Tnfrsf13b	5.063	2.61E-03
Ahr	4.790	4.58E-03
Ikbke	4.287	9.11E-03
Cd48	3.758	1.05E-02
Ccl9	2.713	1.73E-03

Figure 11: Siglec-F+ neutrophils acquire a distinct transcriptomic profile indicating terminal differentiation. (**A**) Schematic representation of experimental setup. On d0, AAPV was induced in C57BL/6J mice by applying 10 µg fMLP + 10 µg LPS in 50 µl PBS i.t. and 1 mg anti-MPO antibody i.p. (0.5 mg of each clone 6D1 and 6G4). 6 days after disease induction, mice were painlessly killed, single-cell suspensions prepared from the lungs, and the indicated neutrophil populations FACS-sorted for NanoString analysis. (**B**) Differentially expressed genes in Siglec-F+ neutrophils in comparison to classical neutrophils. (**C**) Top 10 down-regulated genes in Siglec-F+ neutrophils. (**D**) Top 10 up-regulated genes in Siglec-F+ neutrophils. (**E**) Pathway analysis of data shown in B. Data shown are representative of two independent experiments. The experiment was performed with the assistance of Ms. Karola Mai, University of Bonn.

3.1.6.Siglec-F^{+} neutrophils produce more NADPH-dependent ROS

Our results identified dynamic changes in the proportion of classical and Siglec-F^{+} neutrophils in the lung during AAPV progression expressing different transcriptional programs. Therefore, we investigated whether those two neutrophil subsets fulfill different functions during AAPV progression. One of neutrophils' main effector mechanisms is the production of superoxide radicals by the NADPH-oxidase complex (NADPHox), which in turn are critical regulators of neutrophil functions [199] and contribute to inflammation and tissue injury (reviewed in [200]). Therefore, we quantified the production of ROS three days after disease induction by flow cytometry using the ROS-dependent fluorescent dye dihydrorhodamine 123 (DHR123) (Figure 12, A and B). Classical neutrophils from C57BL/6J mice undergoing AAPV produced only residual amounts of spontaneous ROS compared to their NADPHox-deficient gp91phox$^{-/null}$ counterparts in terms of proportion of ROS-producing cells (Figure 12, B and C) and the amount produced (Figure 12, D). However, we detected a substantial increase in spontaneous and PMA-induced maximal ROS production by Siglec-F^{+} neutrophils (Figure 12, C and D). In contrast, Siglec-F^{+} neutrophils from gp91phox$^{-/null}$- mice undergoing AAPV had similar low levels of ROS production to those from C57BL/6J mice (Figure 12, B-D), indicating that non-NADPHox-derived ROS (primarily mitochondrial) was residual and not differentially expressed by these two neutrophil subpopulations. Taken together, we demonstrate that Siglec-F^{+} neutrophils produced more NADPH oxidase-dependent ROS during AAPV than their classical counterparts.

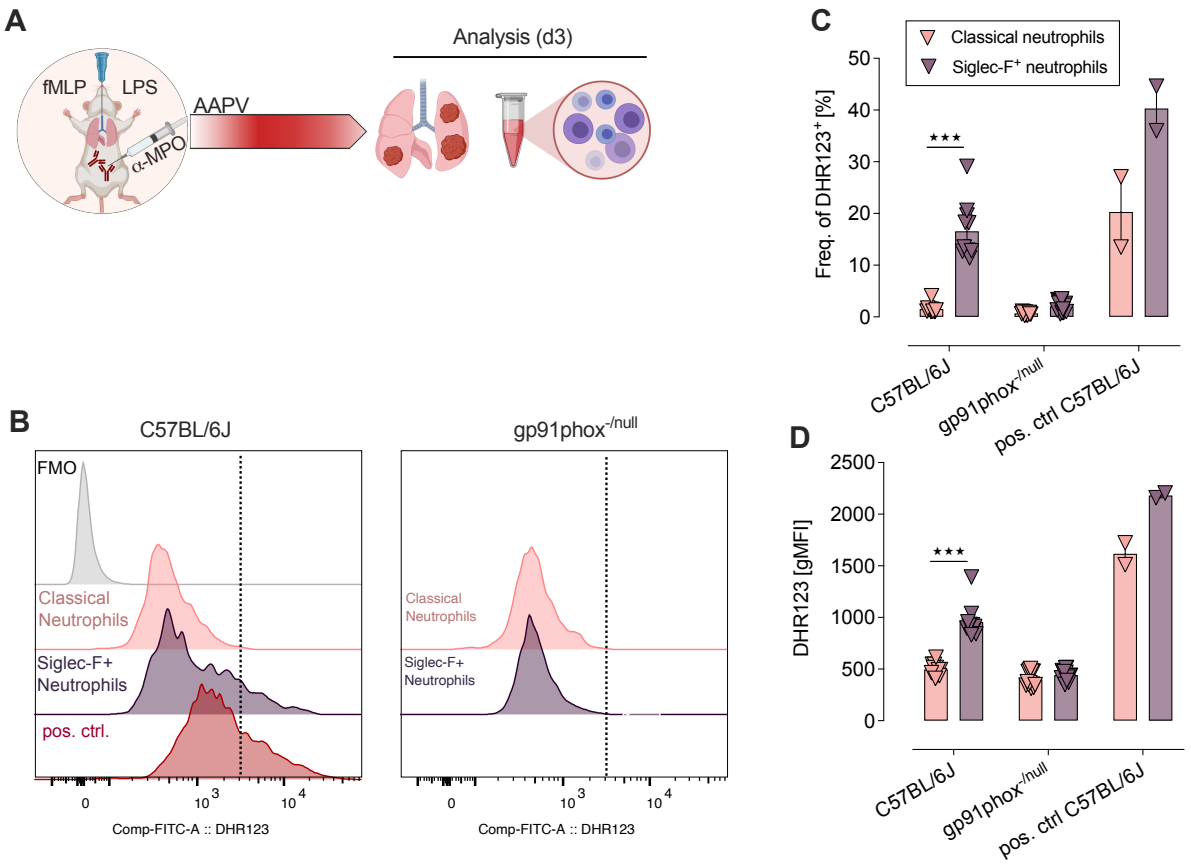

Figure 12: Siglec-F+ neutrophils produce more NADPH-dependent ROS. (**A**) Schematic representation of experimental setup. On d0, AAPV was induced in C57BL/6J and gp91phox$^{-/null}$ mice by applying 10 µg fMLP + 10 µg LPS in 50 µl PBS i.t. and 1 mg anti-MPO antibody i.p. (0.5 mg of each clone 6D1 and 6G4). Three days after disease induction, mice were painlessly killed, the bronchoalveolar lavage fluid was collected, and ROS production in neutrophils was quantified using FACS. As a positive control, cells were stimulated with 1 µg/mL PMA at 37°C for 20 mins before ROS staining. (**B**) Representative histograms of DHR123 fluorescence intensity in BALF neutrophils of C57BL/6J and gp91phox$^{-/null}$ mice three days after AAPV induction. Pos. Ctrl., neutrophils treated with PMA. (**C**) Quantification of the frequency of ROS-producing neutrophils. (**D**) gMFI quantification of ROS production by the indicated BALF neutrophil populations. The data shown are pooled from two independent experiments. Mean ± SEM; each symbol represents one mouse. Two-way ANOVA comparing classical vs. Siglec-F+ neutrophils within each group, ***p<0.001. The experiment was performed with the assistance of Ms. Karola Mai, University of Bonn.

3.1.7.NADPH-oxidase-derived ROS drives pulmonary hemorrhages

Several neutrophil-mediated inflammatory processes, such as NETosis and even neutrophil death, have been shown to depend on NADPH-oxidase-generated ROS [31]. We, therefore, investigated whether vasculitis severity is altered in gp91phox-deficient mice (Figure 13, A). Although gp91phox$^{-/null}$ mice showed no differences in weight loss (Figure 13, B), they had lower pulmonary hemorrhages as quantified by hemoglobin content (Figure 13, C) and red blood cell counts in the BALF (Figure 13, D) at the peak of disease, suggesting a potential pathogenic role of NADPH-oxidase derived ROS in AAPV. However, there were no differences in the overall leukocyte infiltration (Figure 13, E), particularly classical and Siglec-F^{+} neutrophils (Figure 13, F and G) in NADPHox-deficient mice. Interestingly, alveolar macrophages were strongly decreased (Figure 13, H), while an infiltrating population of macrophages (which will be further discussed in Results section 3.3.1.) was not affected (Figure 13, I). However, these results should be considered preliminary as experiment was performed only once, and further investigations are needed to confirm that NADPH-oxidase-derived ROS regulates lung hemorrhages but not the immune cell compartment.

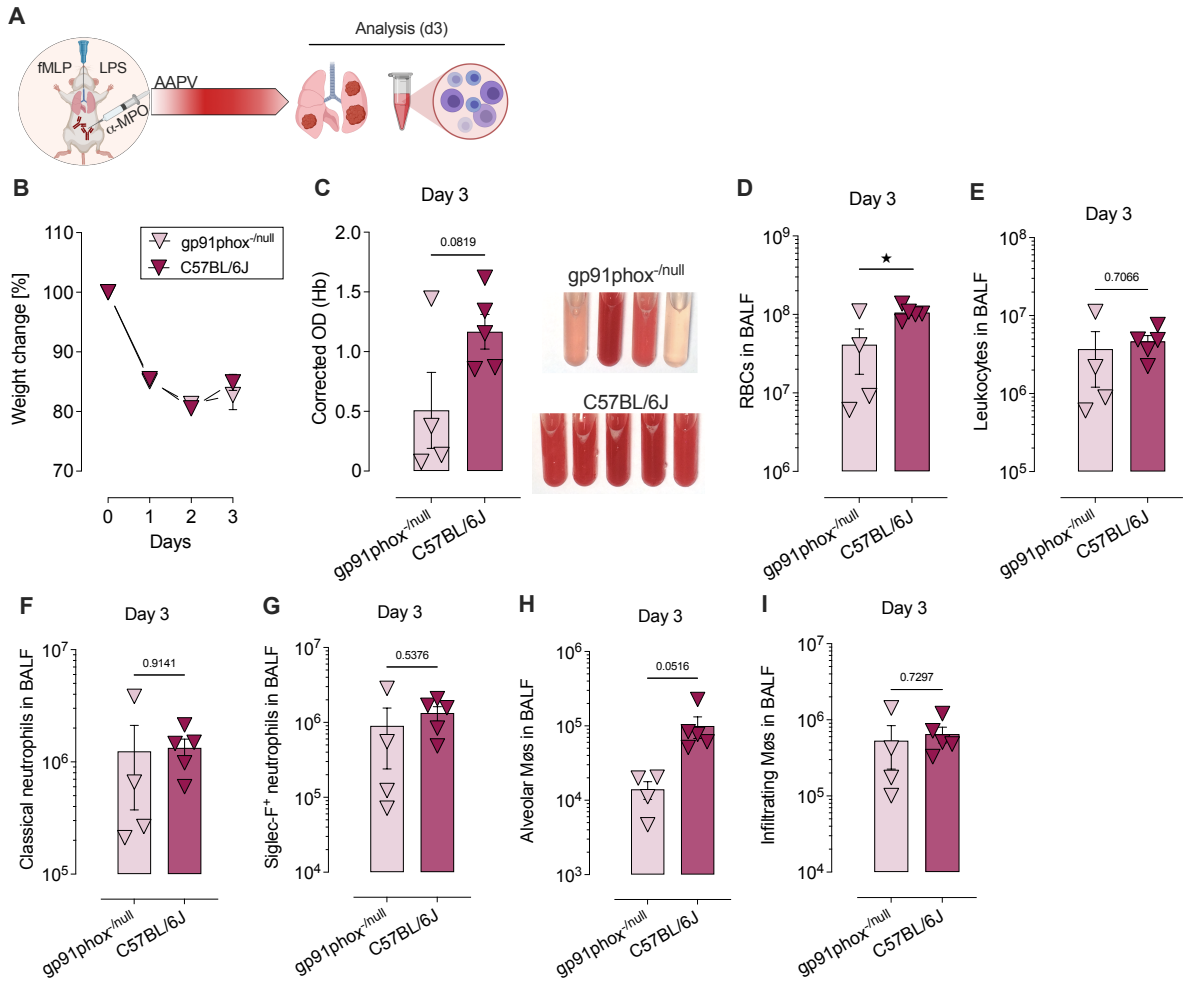

Figure 13: NADPH-oxidase-derived ROS drives pulmonary hemorrhages. (**A**) Schematic representation of experimental setup. On d0, AAPV was induced in C57BL/6J and gp91phox$^{-/null}$ mice by applying 10 µg fMLP + 10 µg LPS in 50 µl PBS i.t. and 1 mg anti-MPO antibody i.p. (0.5 mg of each clone 6D1 and 6G4). Three days after disease induction, mice were painlessly killed, the bronchoalveolar lavage fluid was collected, and hemorrhages and immune cell infiltration were quantified using FACS. (**B**) Weight changes over time in C57BL/6J and gp91phox$^{-/null}$ mice with AAPV. (**C**) Quantification and representative images of hemoglobin in BALF after three days. (**D-I**) FACS quantification of RBCs (D), leukocytes (E), classical neutrophils (F), Siglec-F^{+} neutrophils (G), alveolar Møs (H), and infiltrating Møs (I) in BALF of C57BL/6J and gp91phox$^{-/null}$ mice with AAPV. Data are shown from one experiment. Mean ± SEM; each symbol represents one mouse. Unpaired student's *t*-test, *p<0.05. The experiment was performed with the assistance of Ms. Karola Mai, University of Bonn.

3.2.Nucleic acid-sensing promotes ANCA-associated vasculitis

3.2.1.Extracellular DNA accumulates in the lungs upon inflammation

In patients with AAV, increased levels of extracellular DNA were found in serum as well as at the side of lesions [24, 26]. Kessenbrock et al. suggested that NETosis is a potential disease trigger, as they observed NETs formation in kidney biopsy of patients undergoing small-vessel vasculitis [24]. However, whether extracellular DNA accumulation is simply casual or pathogenic and involved in disease progression remains to be elucidated. Hence, we investigated the role of DNA in disease pathogenesis. First, we quantified extracellular DNA in the BALF of mice throughout the disease course (Figure 14, A). In our mouse model, treating mice with fMLP+LPS was sufficient to provoke extracellular DNA accumulation in the BALF one day after application, which increased further on day 3. This increase was independent of AAPV disease progression (Figure 14, B). However, only the combination of fMLP+LPS with anti-MPO antibodies provoked pulmonary hemorrhages (Figure 14, C and D). By day 7, when mice recovered from disease and hemorrhages were partially cleared (Figure 14, C and D), extracellular DNA levels returned to basal level (Figure 14, B). Interestingly, anti-MPO antibodies alone did not induce any release of DNA. All in all, our data suggest that fMLP+LPS are sufficient to promote extracellular DNA accumulation, but only the combination of extracellular DNA and anti-MPO antibodies induces pulmonary hemorrhages.

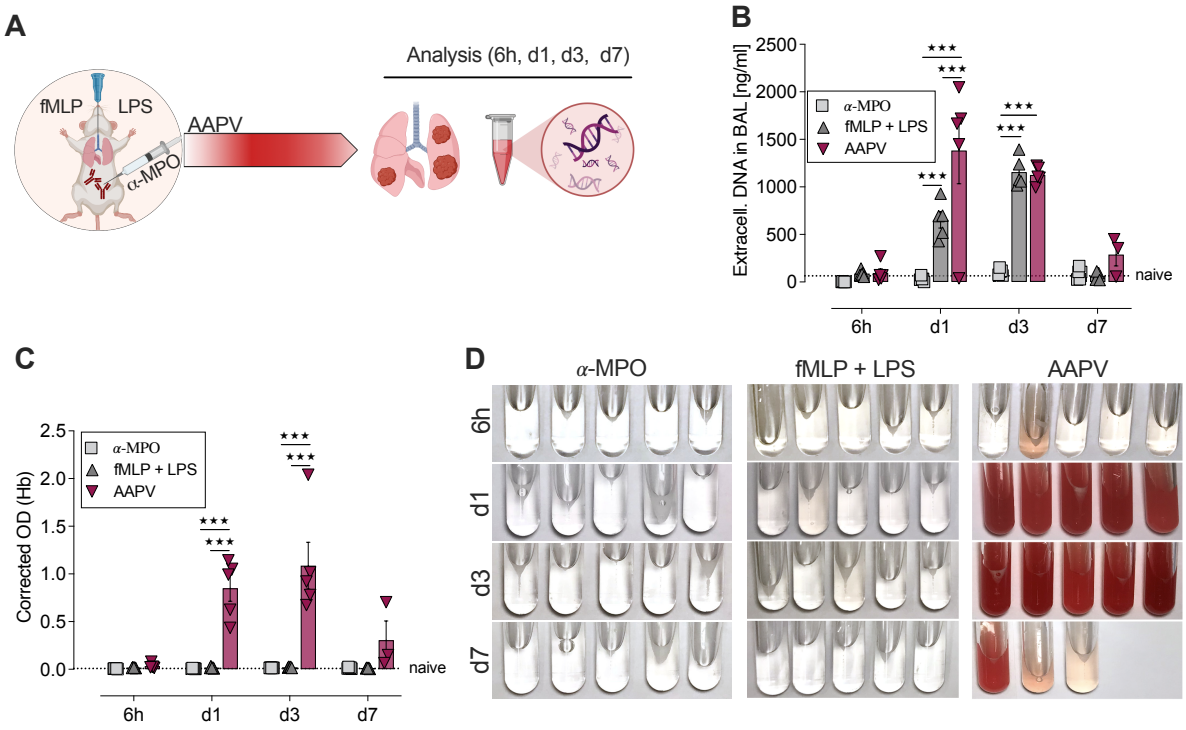

Figure 14: Extracellular DNA accumulates in the lungs upon inflammation. (**A**) Schematic representation of experimental setup. On day 0, female mice were given either 10 µg fMLP + 10 µg LPS in 50 µl PBS i.t, 1 mg anti-MPO antibody i.p. (0.5 mg of each clone 6D1 and 6G4), or the combination. Mice were painlessly killed after 6 hours and after 1, 3, and 7 days. Bronchoalveolar lavage fluid was taken, and extracellular DNA levels and hemorrhages were quantified. (**B**) Extracellular DNA in BALF of mice treated either with anti-MPO, fMLP+LPS, or combinatory treatment at the indicated time points. (**C**) Quantification of hemoglobin in BALF at the indicated time points. (**D**) Representative images of BALF. Data in (C and D) were already shown in Figure 7 (J and K) and are included here for a comparison of kinetics with (B). Shown is a representative of at least 3 independent experiments. Mean ± SEM; each symbol represents a mouse. Two-way ANOVA, **p<0.01; ***p<0.001. The experiment was performed with the assistance of Mr. Calvin Krollmann, UKB, and Dr. Susanne F. Viehmann, University of Bonn.

3.2.2.STING-deficiency does not prevent AAPV onset

Having identified increased extracellular DNA in the bronchoalveolar space of mice with AAPV, we questioned whether nucleic acid sensors trigger an inflammatory response that drives disease pathogenesis. As the cGAS-STING-type-I IFN pathway is a major nucleic acid sensing pathway of double-stranded DNA, we investigated whether STING-deficiency can prevent disease development (Figure 15, A). For this, we used Tmem173^{gt}/J mice lacking functional STING, hereafter referred to as STING$^{-/-}$. Although pulmonary hemorrhages were only slightly weaker in STING-deficient mice one day after disease induction (Figure 15, B), the number of infiltrating leukocytes was significantly reduced compared to C57BL/6J mice (Figure 15, C). Especially, neutrophils, which make up most of the infiltrating immune cells by day one, were significantly reduced in STING$^{-/-}$ mice (Figure 15, D). One of the downstream signaling pathways of cGAS/STING activation is the production of type-I IFN. Therefore, we investigated the expression of *Ifn-β* in the lungs of wild-type and STING$^{-/-}$ mice. Consistent with our results on lung hemorrhages, we couldn't detect any differences on day 1 (Figure 15, E). In summary, STING-deficiency does not prevent induction of pulmonary hemorrhages despite accumulation of extracellular DNA at that time.

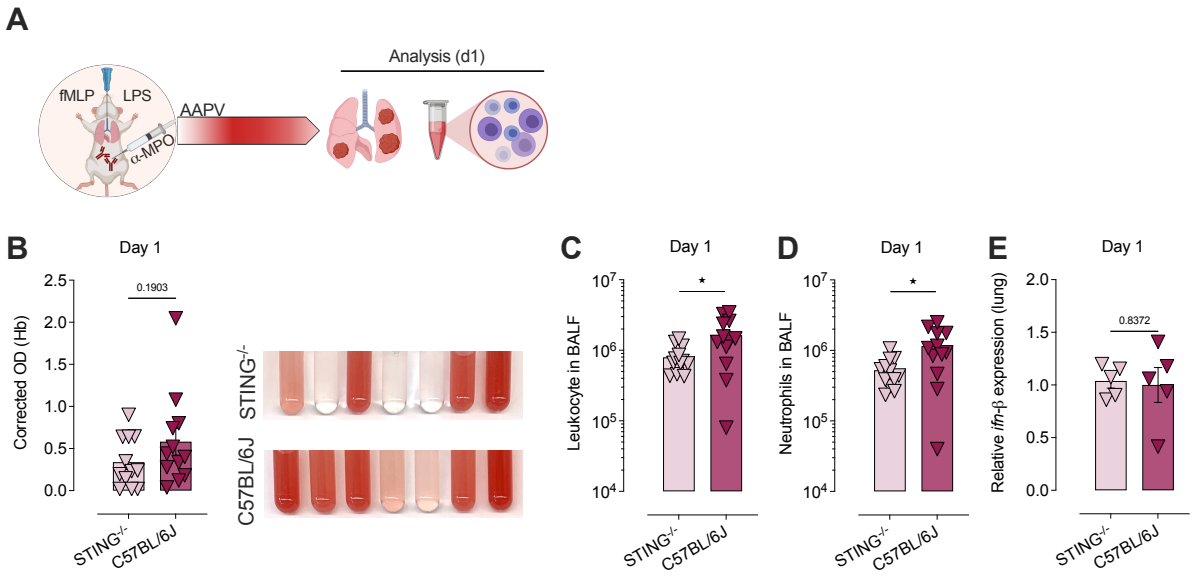

Figure 15: STING-deficiency does not prevent AAPV onset. (**A**) Schematic representation of experimental setup. On day 0, female STING$^{-/-}$ and C57BL/6J mice were given 10 µg fMLP + 10 µg LPS in 50 µl PBS i.t. and 1 mg anti-MPO antibody i.p. (0.5 mg of each clone 6D1 and 6G4). Mice were painlessly killed 1 day later. Bronchoalveolar lavage fluid or whole lung was taken to quantify hemorrhages, immune cell infiltration, and *Ifn-β* expression. (**B**) Quantification of hemoglobin and representative images of BALF of the indicated mice with AAPV. (**C** and **D**) FACS quantification of total leukocytes (C) and absolute neutrophils (D) in BALF of the indicated groups with AAPV. (**E**) Relative *Ifn-β* expression in lungs of the indicated groups with AAPV. RNA from whole lung tissue was isolated, and *Ifn-β* mRNA expression was quantified by Dr. Hella Luksch, TU Dresden. Data are pooled from two independent experiments (B-D) and one experiment (E). Mean ± SEM; each symbol represents a mouse. Unpaired student's *t*-test; *p<0.05.

3.2.3.STING-deficiency ameliorates disease progression *in vivo*

Apparently, STING activation is not necessary for disease induction because STING-deficient mice developed pulmonary hemorrhages similarly to wild-type mice during the initiation phase. However, we could already identify a slight reduction of hemorrhages and immune cell infiltration by day 1. Therefore, we aimed to investigate whether STING is required to prevent further disease progression at later time points. Consequently, we investigated disease severity in STING-deficient and wild-type mice (Figure 16, A). We observed that STING$^{-/-}$ mice recovered faster from weight loss than C57BL/6J (Figure 16, B). Moreover, they displayed statistically significant lower pulmonary hemorrhages on day 3, quantified by hemoglobin (Figure 16, C) and RBC counts (Figure 16, D) in the BALF. Although overall leukocyte infiltration was only slightly reduced (Figure 16, E), neutrophil numbers strongly decreased upon STING-deficiency (Figure 16, F).

Investigating the kinetics of *Ifn-β* gene expression over time course of AAPV revealed a progressive but transient increase that peaked at day 3 (Figure 16, G), which mirrors progression of hemorrhages (previous Figure 7, J). When comparing *Ifn-β* expression in STING$^{-/-}$ and C57BL/6J mice three days after disease induction, we could see that STING-deficiency prevented up-regulation of *Ifn-β* (Figure 16, H). Interestingly, STING$^{-/-}$ mice had slight increased *Ifn-β* expression in comparison to fMLP+LPS treated control mice (Figure 16, H). Thus, STING-signaling is required for disease progression but might not be the only activated signaling pathway resulting in IFN-β production during AAPV.

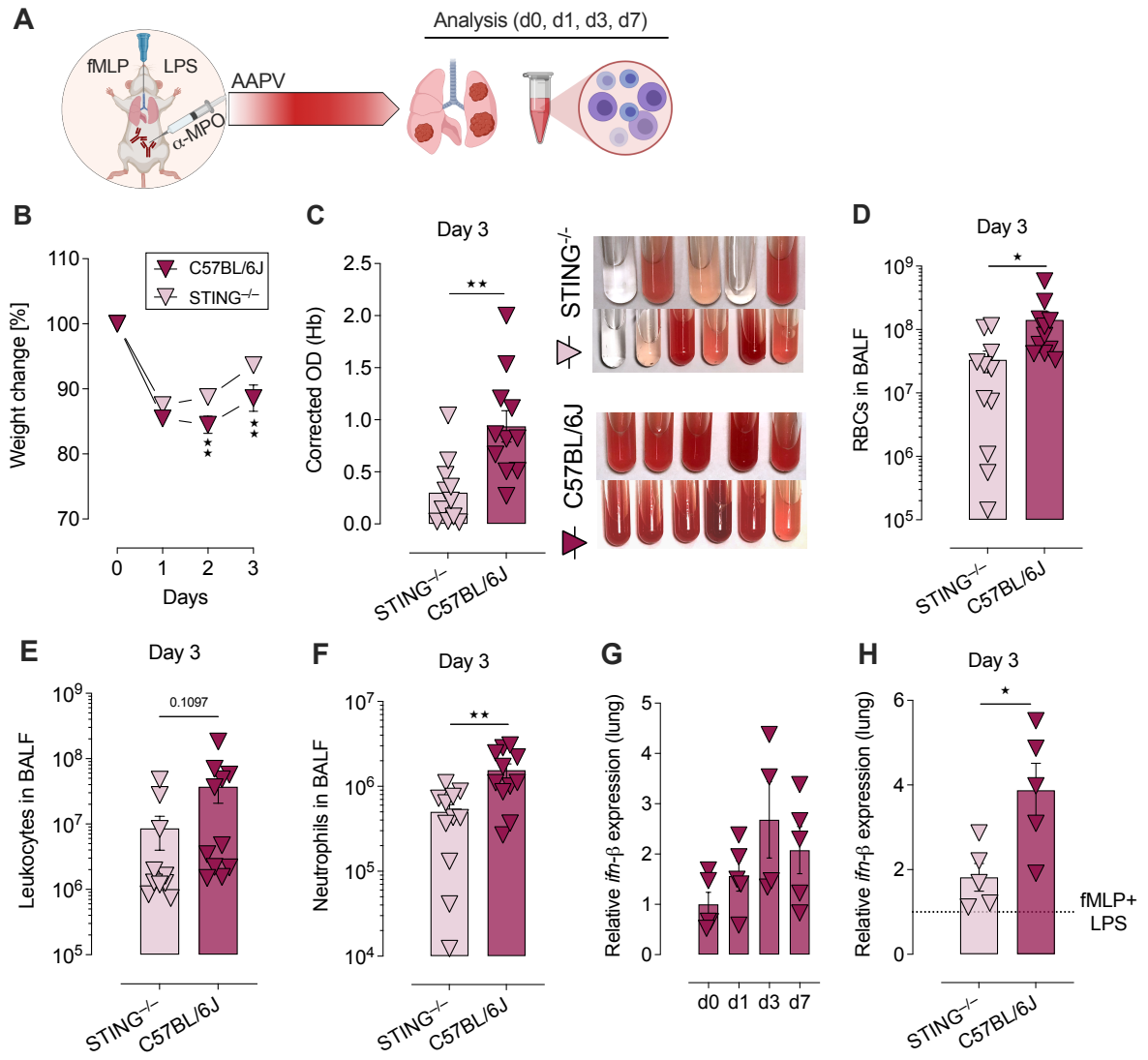

Figure 16: STING-deficiency ameliorates disease progression *in vivo*. (**A**) Schematic representation of experimental setup. On day 0, female STING$^{-/-}$ and C57BL/6J mice were given 10 µg fMLP + 10 µg LPS in 50 µl PBS i.t. and 1 mg anti-MPO antibody i.p. (0.5 mg of each clone 6D1 and 6G4). Mice were painlessly killed three days after disease induction. Bronchoalveolar lavage fluid was taken, and hemorrhages, immune cell infiltration, and *ifn-β* expression in the lungs were quantified. (**B**) Weight change over time of the indicated groups undergoing AAPV. (**C**) Quantification of hemoglobin of the indicated groups. (**D-F**) FACS quantification of RBCs (D), total leukocytes (E), and total neutrophils (F) in BALF of the indicated groups with AAPV. (**G** and **H**) Relative *Ifn-β* expression in lungs of wild-type mice with AAPV over time (G) and in STING$^{-/-}$ and C57BL/6J mice (H) with AAPV on day 3. RNA from whole lung tissue was isolated, and *Ifn-β* expression was quantified by Dr. Hella Luksch, TU Dresden. Data are pooled from two independent experiments (B-F) and one experiment (G and H). Mean ± SEM; each symbol represents a mouse. Unpaired student's *t*-test, *p<0.05; **p<0.01. The experiment was performed with the assistance of Dr. Susanne F. Viehmann, University of Bonn.

3.2.4.IFNAR-1 blockage ameliorates disease progression *in vivo*

STING-signaling normally results in type-I interferon production, which, in turn, triggers a pro-inflammatory reaction. Having identified increased STING-dependent disease progression as well as *Ifn-β* gene expression in lungs during AAPV in mice, we next investigated whether blocking type-I IFN signaling ameliorates disease progression. For this purpose, we treated C57BL/6J mice with an anti-IFNAR-1 blocking antibody or the respective isotype control and analyzed disease progression on day 3. Control mice were treated with fMLP+LPS only (Figure 17, A). Inhibiting type-I IFN signaling prevented AAPV-induced weight loss compared to the respective isotype control-treated mice (Figure 17, B). Additionally, pulmonary hemorrhages quantified by hemoglobin (Figure 17, C) and RBCs (Figure 17, D) were significantly reduced upon IFNAR-1 blockade. Similarly, leukocyte counts (Figure 17 E), in particular, the number of infiltrating neutrophils were decreased (Figure 17, F), whereas those of tissue-resident alveolar macrophages were not affected (Figure 17, G). Although some mice still developed pulmonary hemorrhages upon anti-IFNAR-1-treatment, weight change and leukocyte counts were comparable to the control group treated with fMLP+LPS only (Figure 17, B, E and F). These data indicate that IFNAR-1 blockade partially protects from pulmonary vasculitis and suggests that targeting IFNAR-1 signaling may be of therapeutic advantage.

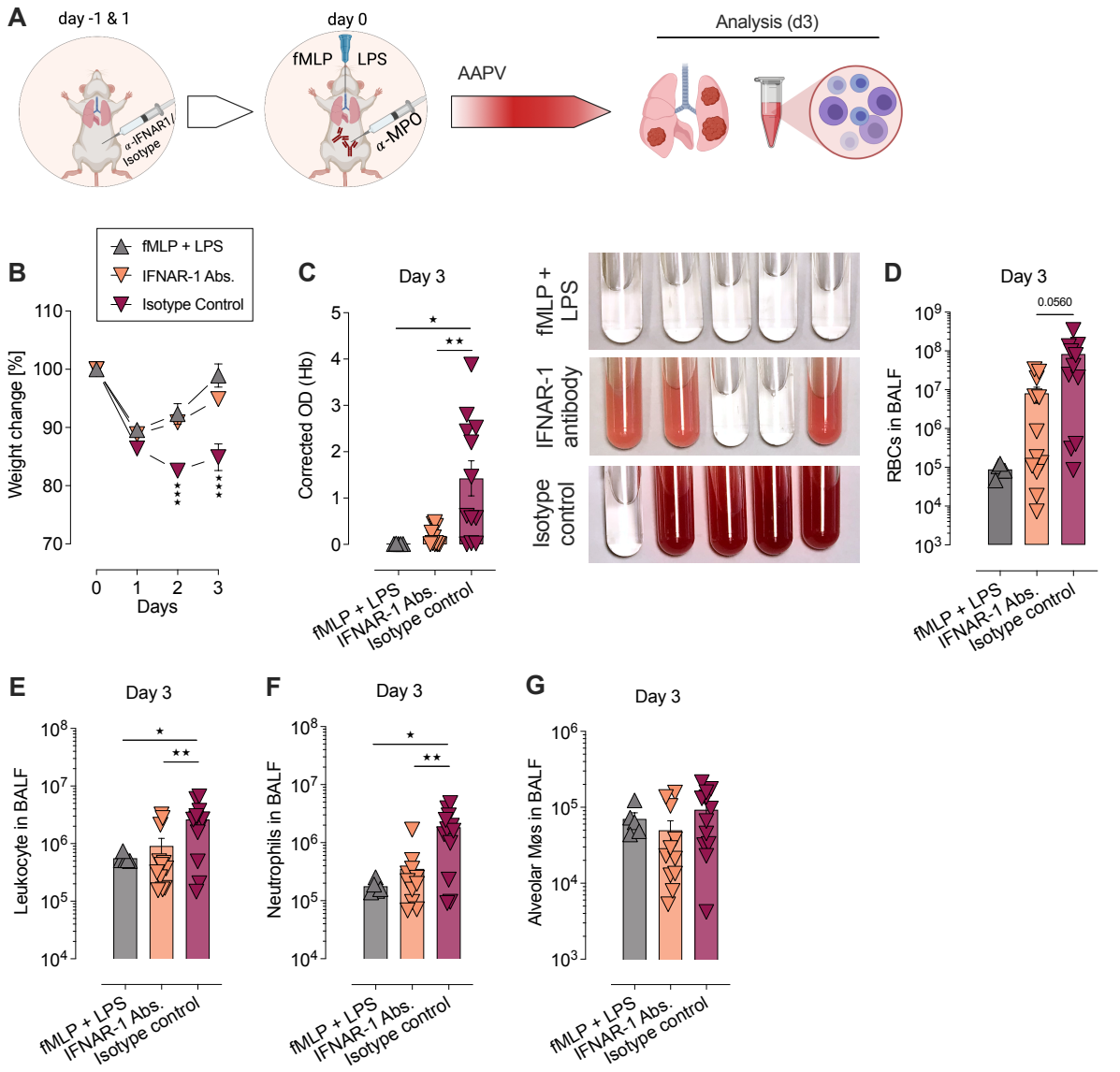

Figure 17: IFNAR-1 blockage ameliorates disease progression *in vivo*. (A) Schematic representation of experimental setup. On days -1 and d1, female C57BL/6J mice were given 250 µg of anti-IFNAR-1 blocking antibody or the respective isotype control i.p.. On d0, AAPV was induced by applying 10 µg fMLP + 10 µg LPS in 50 µl PBS i.t. and 1 mg anti-MPO antibody i.p. (0.5 mg of each clone 6D1 and 6G4). The control group received only fMLP+LPS on d0. Mice were painlessly killed 3 days after disease induction. Bronchoalveolar lavage fluid was taken, and hemorrhages and immune cell infiltration were quantified. (**B**) Weight changes over time. (**C**) Quantification of hemoglobin and representative pictures of BALF of the indicated groups. (**D-G**) FACS quantification of RBCs (D), leukocytes (E), neutrophils (F), and alveolar macrophages (G) in BALF of the indicated groups. Data are pooled from two independent experiments (B-G). Mean ± SEM; each symbol represents a mouse. One-way ANOVA, *p<0.05; **p<0.01; ***p<0.001. The experiment was performed with the assistance of Dr. Susanne F. Viehmann, University of Bonn.

3.2.5.STING inhibitor H151 ameliorates AAPV *in vivo*

The group of Andrea Ablasser recently developed a small molecule STING inhibitor that can be used in humans and mice [201]. Having identified the STING/IFN-I signaling pathway to drive AAPV progression, we aimed to test whether this STING inhibitor can be used as a pharmacological intervention in autoimmune vasculitis. For this purpose, C57BL/6J mice were treated with H151 or the respective vehicle control daily starting on the day of AAPV induction (d0), and disease progression was analyzed after three days (Figure 18, A). Mice treated with H151 recovered faster from weight loss (Figure 18, B), and they developed significantly weaker pulmonary hemorrhages, quantified by hemoglobin (Figure 18, C) and numbers of RBCs (Figure 18, D) in the BALF. This was further confirmed by quantification of infiltrating immune cells by FACS, which demonstrated substantially fewer overall leukocytes upon STING inhibition (Figure 18, E). Especially the influx of neutrophils was prevented (Figure 18, F). Infiltrating macrophages were statistical significantly decreased upon STING inhibition (Figure 18, G), whereas resident alveolar macrophages were unaffected (Figure 18, H). Reduced immune cell infiltration was further depicted by histopathological scoring, which significantly reduced upon STING inhibition (Figure 18, I). Thus, targeting the STING signaling pathway using small molecule inhibitors may be a potential pharmacological intervention for patients with AAV.

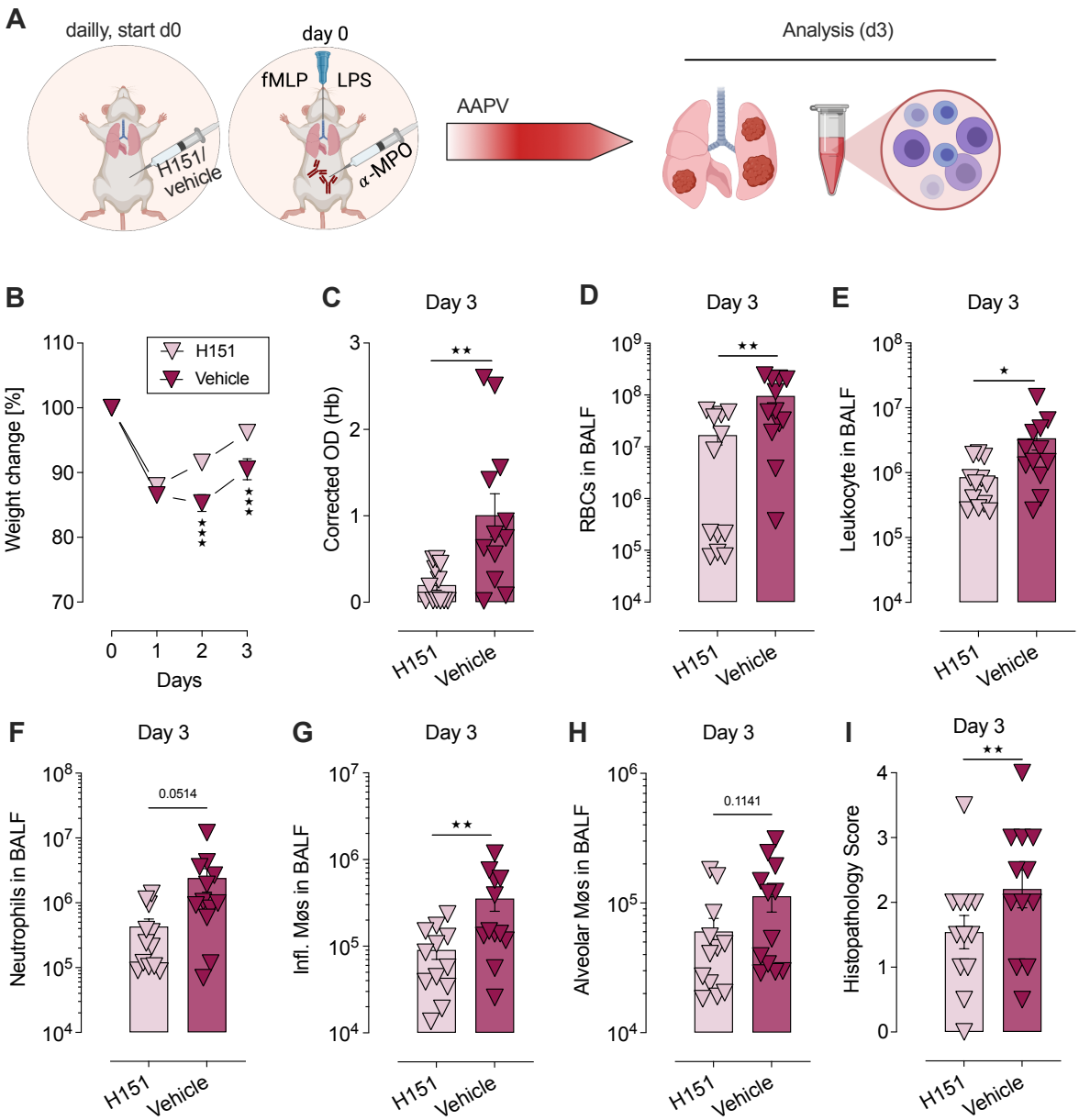

Figure 18: STING inhibitor H151 ameliorates AAPV *in vivo*. (**A**) Schematic representation of experimental setup. Starting on day 0, female C57BL/6J mice were given 750 nmol of H151 or the respective vehicle control (i.p.). On the same day, AAPV was induced by applying 10 µg fMLP + 10 µg LPS in 50 µl PBS i.t. and 1 mg anti-MPO antibody i.p. (0.5 mg of each clone 6D1 and 6G4). Mice were painlessly killed 3 days after disease induction. Bronchoalveolar lavage fluid was taken, and hemorrhages and immune cell infiltration were quantified. (**B**) Weight changes over time. (**C**) Quantification of hemoglobin in the BALF of the indicated groups. (**D-H**) FACS quantification of RBCs (D), leukocytes (E), neutrophils (F), infiltrating macrophages (G), and alveolar macrophages (H) in BALF of the indicated groups. (**I**) Histopathology score of lungs from mice with AAPV. Data are pooled from two independent experiments. Mean ± SEM; each symbol represents a mouse. Unpaired student's *t*-test, *p<0.05; **p<0.01; ***p<0.001. The experiment was performed with the assistance of Dr. Susanne F. Viehmann, University of Bonn.

3.3. Dual role of macrophage subsets in ANCA-associated vasculitis

3.3.1. Monocyte-derived macrophages infiltrate the bronchoalveolar space during AAPV progression

After identifying the STING/type-I interferon pathway to promote pathogenesis of vasculitis, we were interested in identifying the cell type sensing DNA and producing type-I interferon. Investigating immune cell infiltration at the peak of the disease (Figure 19, A) revealed a population of macrophages infiltrating the bronchoalveolar space upon disease induction that were phenotypically distinct from tissue-resident alveolar macrophages (Figure 19, B). Infiltrating macrophages accumulated strongly in the lungs in mice with vasculitis in comparison to fMLP+LPS-treated mice (Figure 19, C). Moreover, they become more prominent than resident alveolar macrophages at the peak of the disease in terms of cell numbers (day 3) (Figure 19, C).

Several findings indicated that monocytes gave rise to the infiltrating macrophage subset. Phenotypically, infiltrating macrophages displayed enhanced Ly-6C expression similar to monocytes and contrary to resident alveolar macrophages and neutrophils (Figure 19, D left panel and E). Additionally, infiltrating macrophages expressed F4/80, a macrophage marker not yet expressed on monocytes indicating their advanced differentiation (Figure 19, D right panel and F). Furthermore, expression of CCR2, which promotes monocytes egress from bone marrow and thus infiltration into inflamed tissues [202], was required to generate a normal size of infiltrating macrophages at the disease peak, as demonstrated in CCR2-deficient ($CCR2^{-/-}$) mice (Figure 19, G and H). Therefore, we conclude that monocyte-derived macrophages infiltrate the lung during AAPV to become the dominant macrophage population.

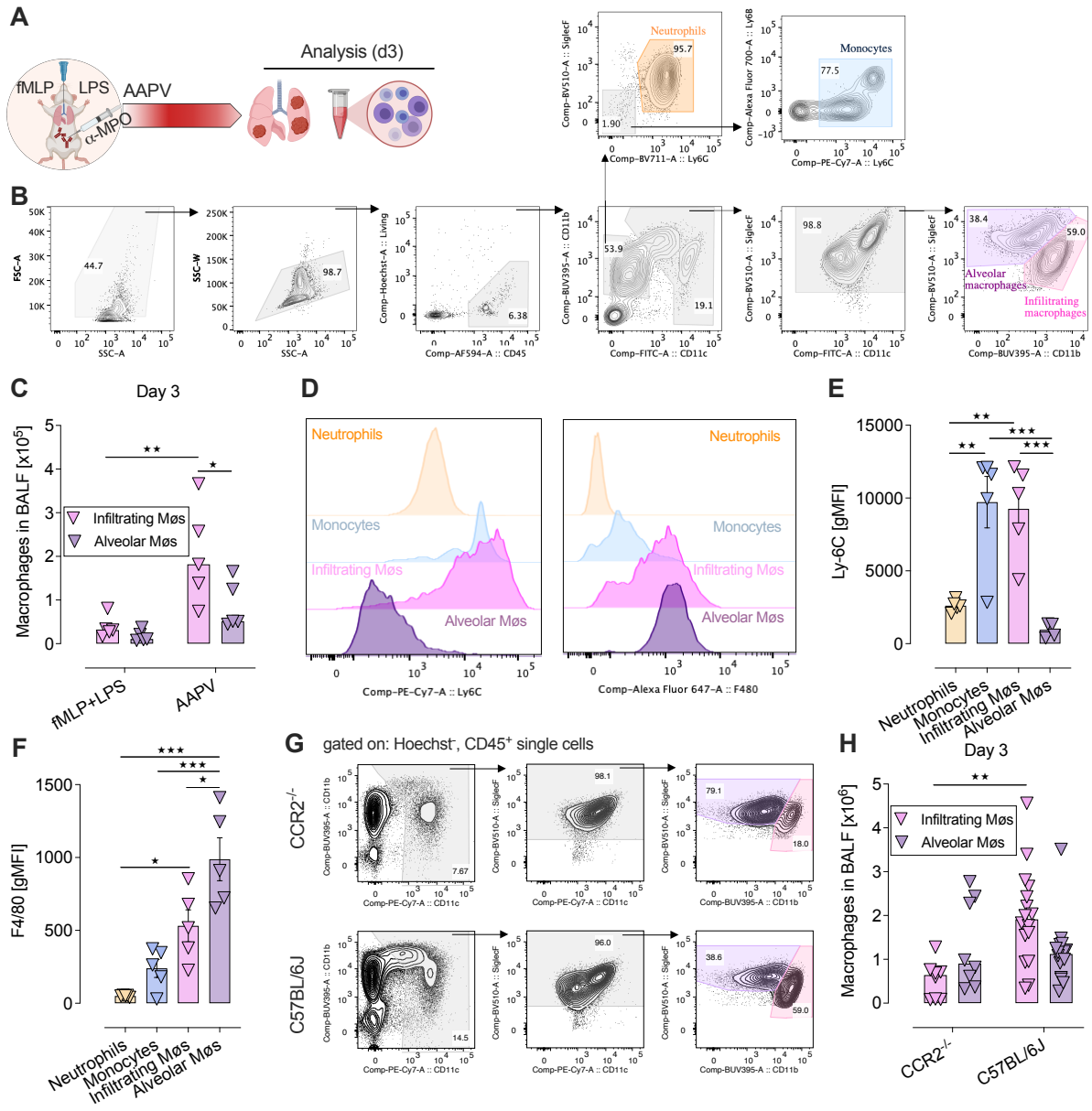

Figure 19: Monocyte-derived macrophages infiltrate the bronchoalveolar space during AAPV progression. (**A**) Schematic representation of experimental setup. On d0, AAPV was induced in C57BL/6J and CCR2-deficient mice by applying 10 µg fMLP + 10 µg LPS in 50 µl PBS i.t. and 1 mg anti-MPO antibody i.p. (0.5 mg of each clone 6D1 and 6G4). Mice were painlessly killed three days after disease induction, the bronchoalveolar lavage fluid was collected, and macrophage subsets were analyzed using FACS. (**B**) Gating strategy to identify distinct macrophage populations in female C57BL/6J mice after 3 days of AAPV induction. (**C**) FACS quantification of macrophages in BALF of mice treated with fMLP+LPS or AAPV. (**D**) Representative histograms of Ly-6C and F4/80 expressions of neutrophils, monocytes, infiltrating, and alveolar macrophages. (**E** and **F**) Quantification of geometric mean fluorescence intensity (gMFI) of Ly-6C (E) and F4/80 (F). (**G**) Gating strategy of macrophage subsets in female C57BL/6J and CCR2$^{-/-}$ mice after 3 days of AAPV progression. (**H**) FACS quantification of macrophages in BALF of the indicated groups. The data shown are representative of at least two independent experiments. Mean ± SEM; each symbol represents one mouse. One-way (E,F) or Two-way (C,H) ANOVA, *p<0.05; **p<0.01; ***p<0.001. The experiment was performed with the assistance of Ms. Katharina M. Kirschner, University of Bonn (A-F).

3.3.2. Monocyte-derived macrophages are main IFN-β producers of mice with active AAPV

To further investigate the role of type-I IFN promoting AAPV progression, we aimed to identify the IFN-β-producing cells. For this purpose, we used IFN-β reporter mice which produce the luciferase enzyme upon *Ifn-β* promoter activation (Figure 20, A). After AAPV induction, mice had increased luminescence signal in the lungs compared to naive mice, quantified using non-invasive In Vivo Imaging Systems (IVIS), confirming our previous findings (Figure 20, B). When sorting our candidates of interest (gating strategy and purity control shown in Appendix Figure 37) and quantifying luminescence *ex vivo*, we could identify infiltrating monocyte-derived macrophages as the main producers of IFN-β after AAPV induction. In contrast, alveolar macrophages produced only small amounts, and lymphoid cells, epithelial and endothelial cells, as well as neutrophils did not express detectable IFN-β-luciferase levels (Figure 20, C). These data suggest that infiltrating macrophages are a main source of pathogenic IFN-β in the lung during AAPV.

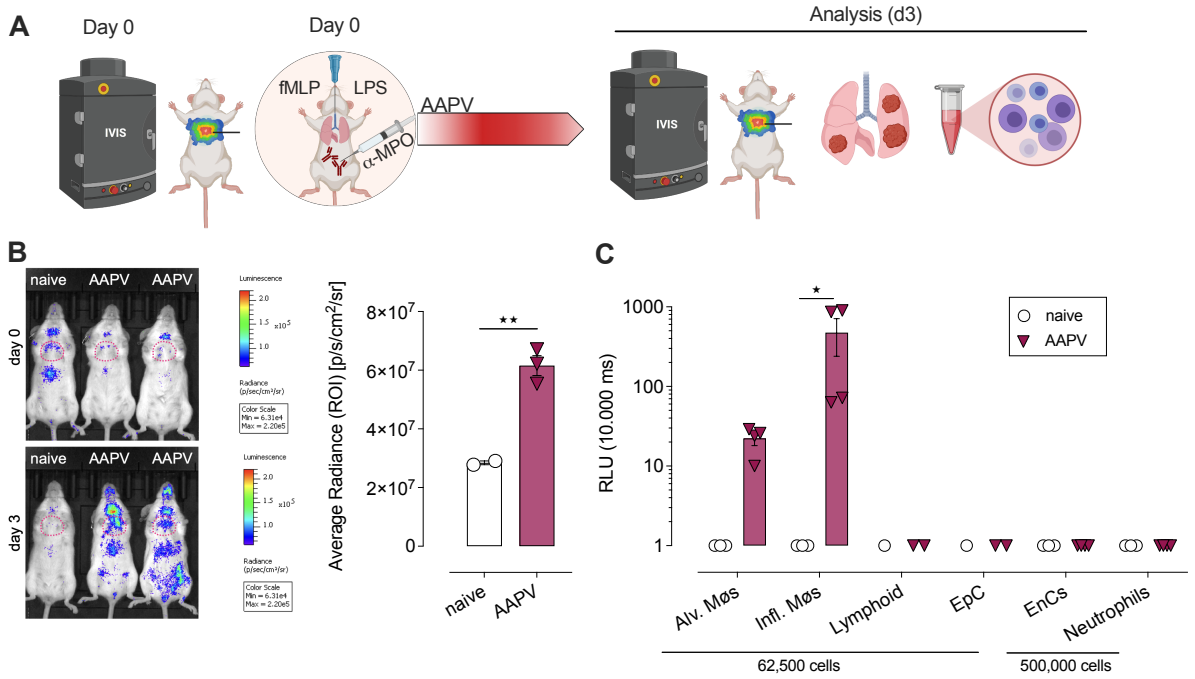

Figure 20: Monocyte-derived macrophages are main IFN-β producers of mice with active AAPV. (**A**) Schematic representation of experimental setup. On d0, AAPV was induced in IFN-β reporter mice by applying 10 µg fMLP + 10 µg LPS in 50 µl PBS i.t. and 1 mg anti-MPO antibody i.p. (0.5 mg of each clone 6D1 and 6G4). IFN-β production was quantified *in vivo* using In Vivo Imaging Systems (IVIS) at d0 and three days after disease induction. On day 3, mice were painlessly killed, the lungs were collected, cells of interest were sorted, and IFN-β production was quantified *ex vivo*. Naive mice served as control. (**B**) Representative images and quantification of luminescence in mouse lungs *in vivo* before and after AAPV-induction. Dotted circle indicates the region of interest (ROI) where lungs are located. (**C**) Quantification of luminescence of sorted cell *ex vivo.* FACS gating strategy of mice with AAPV and sort purity are shown in Appendix Figure 37. RLU, relative light units. Pooled data are shown from two independent experiments. Mean ± SEM; each symbol represents one mouse. Unpaired student's *t*-test (B) or two-way ANOVA (C), *p<0.05; **p<0.01; ***p<0.001. IFN-β reporter mice were kindly provided by Prof. Rayk Behrendt, TU Dresden.

3.3.3.CCR2-deficiency ameliorates disease progression

To investigate whether IFN-β production by monocyte-derived infiltrating macrophages is sufficient to cause vasculitis pathogenesis, we induced AAPV in mice deficient for CCR2, lacking monocytes, and the identified monocyte-derived infiltrating macrophages (Figure 21, A). We previously quantified that CCR2-knockout mice ($CCR2^{-/-}$) had reduced numbers of infiltrating macrophages after AAPV-induction in comparison to wild-type ($CCR2^{+/+}$) mice at the peak of the disease (day 3). In contrast, tissue-resident alveolar macrophages were unchanged (previous Figure 19, G and H). When investigating C57BL/6J mice with functional CCR2 (($CCR2^{+/+}$) and heterozygous ($CCR2^{+/-}$)), we did not observe any differences in terms of monocyte and macrophage numbers as well as in all disease read-outs (Appendix Figure 38). Therefore, for simplicity, we pooled the data obtained using those two mouse strains and labeled it as CCR2-WT. When elucidating disease progression in CCR2-deficient ($CCR2^{-/-}$) mice, we observed faster recovery from weight loss (Figure 21, B) and significantly decreased pulmonary hemorrhages (Figure 21, C) in comparison to their CCR2-WT littermates. However, leukocyte and neutrophil counts did not differ (Figure 21, D and E), while we confirmed a statistically significant reduction of monocytes in CCR2-deficient mice (Figure 21, F). Thus, infiltrating macrophages drive the development of pulmonary hemorrhages, most likely by sensing DNA and subsequently producing pathogenic type-I IFN.

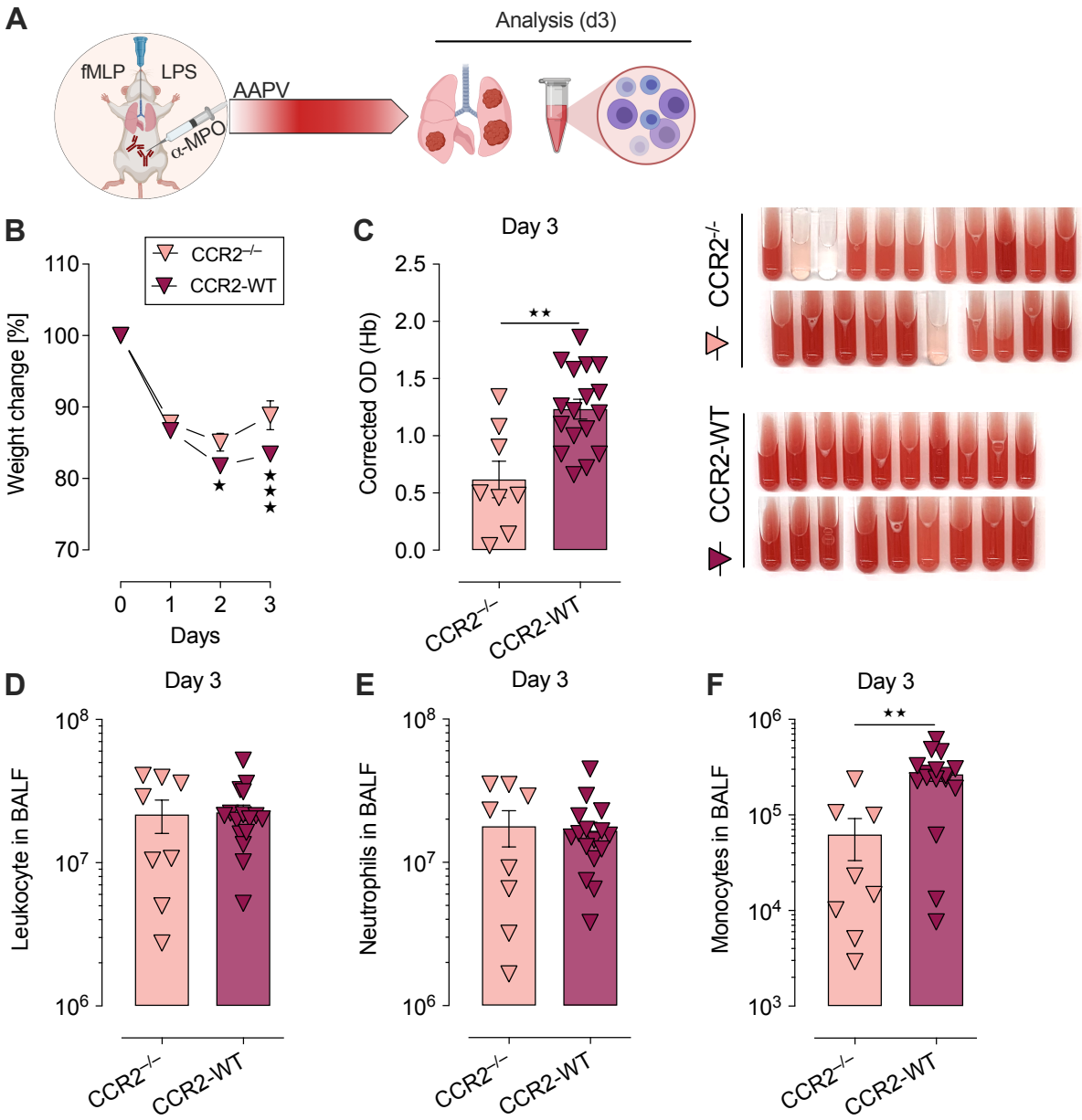

Figure 21: CCR2-deficiency ameliorates disease progression. (**A**) Schematic representation of experimental setup. On d0, AAPV was induced in CCR2$^{-/-}$, CCR2$^{+/-}$, and CCR2$^{+/+}$ mice (data from the respective two were pooled for this figure and mice labeled as CCR2-WT) by applying 10 µg fMLP + 10 µg LPS in 50 µl PBS i.t. and 1 mg anti-MPO antibody i.p. (0.5 mg of each clone 6D1 and 6G4). Mice were painlessly killed after three days, and the BALF was collected to quantify pulmonary hemorrhages and immune cell infiltration. (**B**) Weight changes over time in the indicated groups. (**C**) Quantification of hemoglobin in BALF and representative images. (**D-F**) Quantification of leukocytes (D), neutrophils (E), and monocytes (F) in the BALF of mice with AAPV. The data shown are representative of two independent experiments. Mean ± SEM; each symbol represents one mouse. One-way ANOVA, *p<0.05; **p<0.01; ***p<0.001.

3.3.4.IFN-β production by alveolar macrophages does not promote AAPV pathogenesis

Having observed that tissue-resident AMs produced small amounts of IFN-β, we wanted to investigate whether AMs contributed to disease pathogenesis. Therefore, we depleted alveolar macrophages two days before disease induction by applying Clodronate-loaded Liposomes intratracheally and investigated disease progression on day 3 (Figure 22, A). FACS analysis and cell counts proved the reduction of $CD11b^{-}$ $Siglec\text{-}F^{+}$ tissue-resident alveolar macrophages on day 0 compared to the application of PBS-Liposomes or PBS alone (Figure 22, B and C). Analysis of disease progression revealed that despite slightly more weight loss in mice deficient in alveolar macrophages (Figure 22, D), there were no differences in pulmonary hemorrhages between clodronate liposome-treated mice and the respective control group at the peak of the disease (Figure 22, E). Interestingly, monocyte-derived macrophages increased dramatically after the depletion of alveolar macrophages (Figure 22, F), likely due to an empty macrophage niche in the lung. However, further mechanistic research is required to elucidate why monocyte-derived macrophages increase so strongly. These data thus demonstrate that alveolar macrophages are not required for disease onset and suggest they may be involved in dampening further inflammation by limiting the size of the infiltrating macrophage compartment.

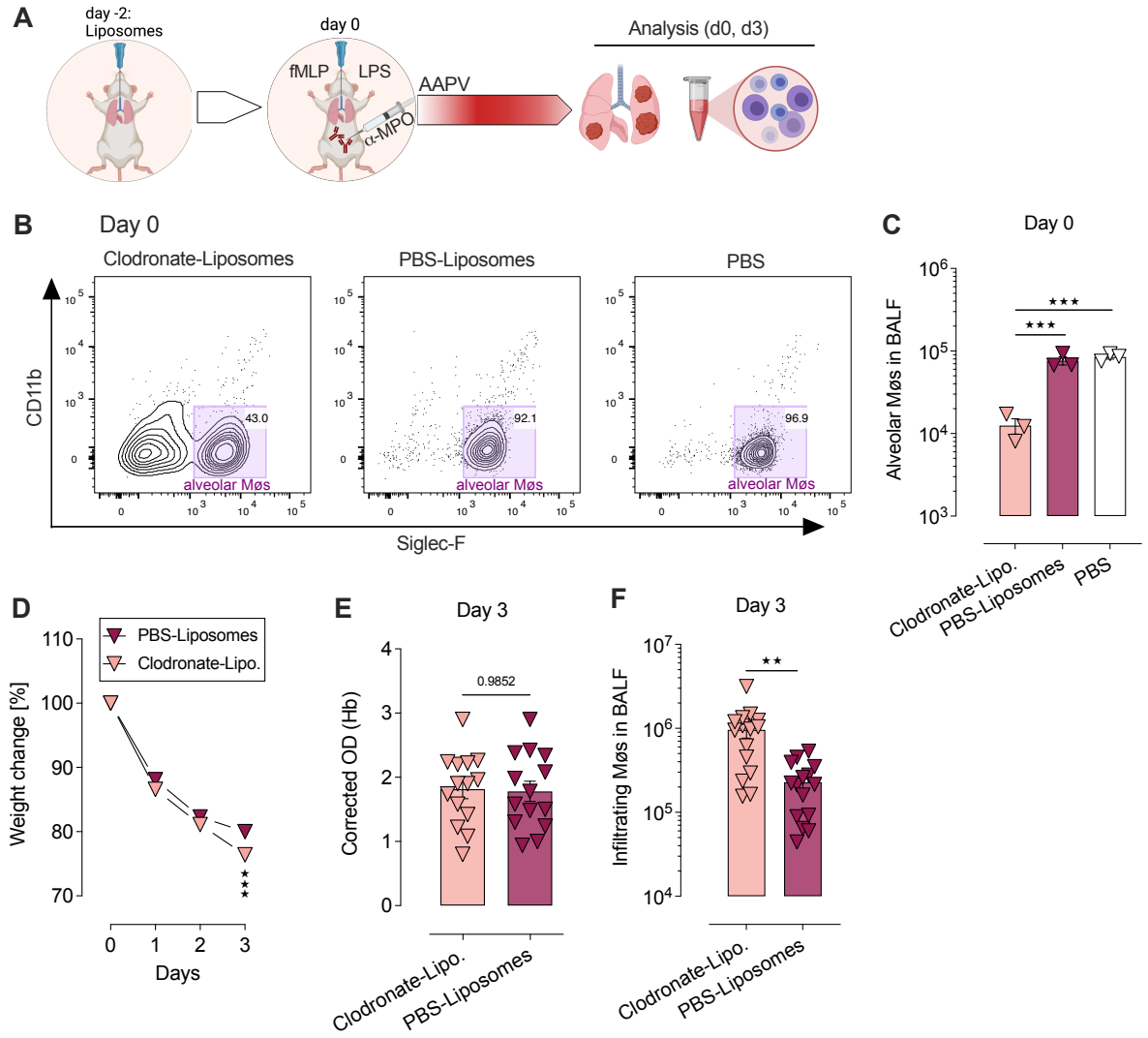

Figure 22: IFN-β production by alveolar macrophages does not promote AAPV pathogenesis. (**A**) Schematic representation of experimental setup. Two days before AAPV induction, mice received either Clodronate- or PBS-Liposomes or PBS (50 µl) i.t.. On d0, AAPV was induced by applying 10 µg fMLP + 10 µg LPS in 50 µl PBS i.t. and 1 mg anti-MPO antibody i.p. (0.5 mg of each clone 6D1 and 6G4). Mice were painlessly killed on day 0 or after three days, and the BALF was collected to quantify pulmonary hemorrhages and immune cell infiltration. (**B**) Representative FACS plots of alveolar macrophages in the BALF of the indicated groups 2 days after Liposome application (day 0). (**C**) Quantification of $CD11b^-$ $Siglec\text{-}F^+$ alveolar macrophages in the BALF on day 0. (**D**) Weight changes over time. (**E**) Quantification of hemoglobin in BALF. (**F**) FACS quantification of infiltrating macrophages in BALF on day 3. The data shown are representative of two experiments (B and C) or pooled data from two independent experiments (D-F). Mean ± SEM; each symbol represents one mouse. One-way ANOVA (C) or unpaired student's *t*-test (D-F), **p<0.01; ***p<0.001.

3.3.5. Alveolar macrophages remove extravascular red blood cells during AAPV

While investigating the role of resident alveolar macrophages in AAPV progression, we identified large phagocytes in the lung of mice with AAPV that had internalized red blood cells (hereafter referred to as hemophagocytes) (Figure 23, A). We were interested in which cell type takes up RBCs in the lung. CD206 expression of macrophages is important for phagocytosis of red blood cells in sickle cell anemia and malaria [203]. Investigation of CD206 expression by phagocytes after AAPV induction revealed that alveolar but not infiltrating macrophages, neutrophils, or monocytes highly expressed this marker (Figure 23, B and C). In line with this, hemophagocytes were absent after alveolar macrophage depletion by Clodronate-Liposomes application, as revealed by Giemsa staining of BALF cytospins (Figure 23, D and E).

To identify the specific phagocytic population taking up extravascular RBCs, phagocytes were sorted (alveolar macrophages, infiltrating macrophages, and neutrophils), and iron staining was performed. Only alveolar macrophages had internalized red blood cells during AAPV progression, indicated by blue iron staining (Figure 23, F). In contrast, neither infiltrating macrophages (Figure 23, G) nor neutrophils (Figure 23, H) showed RBC uptake. These results demonstrate that alveolar macrophages are the main cells clearing extravascular RBCs resulting from hemorrhages in the lung upon AAPV.

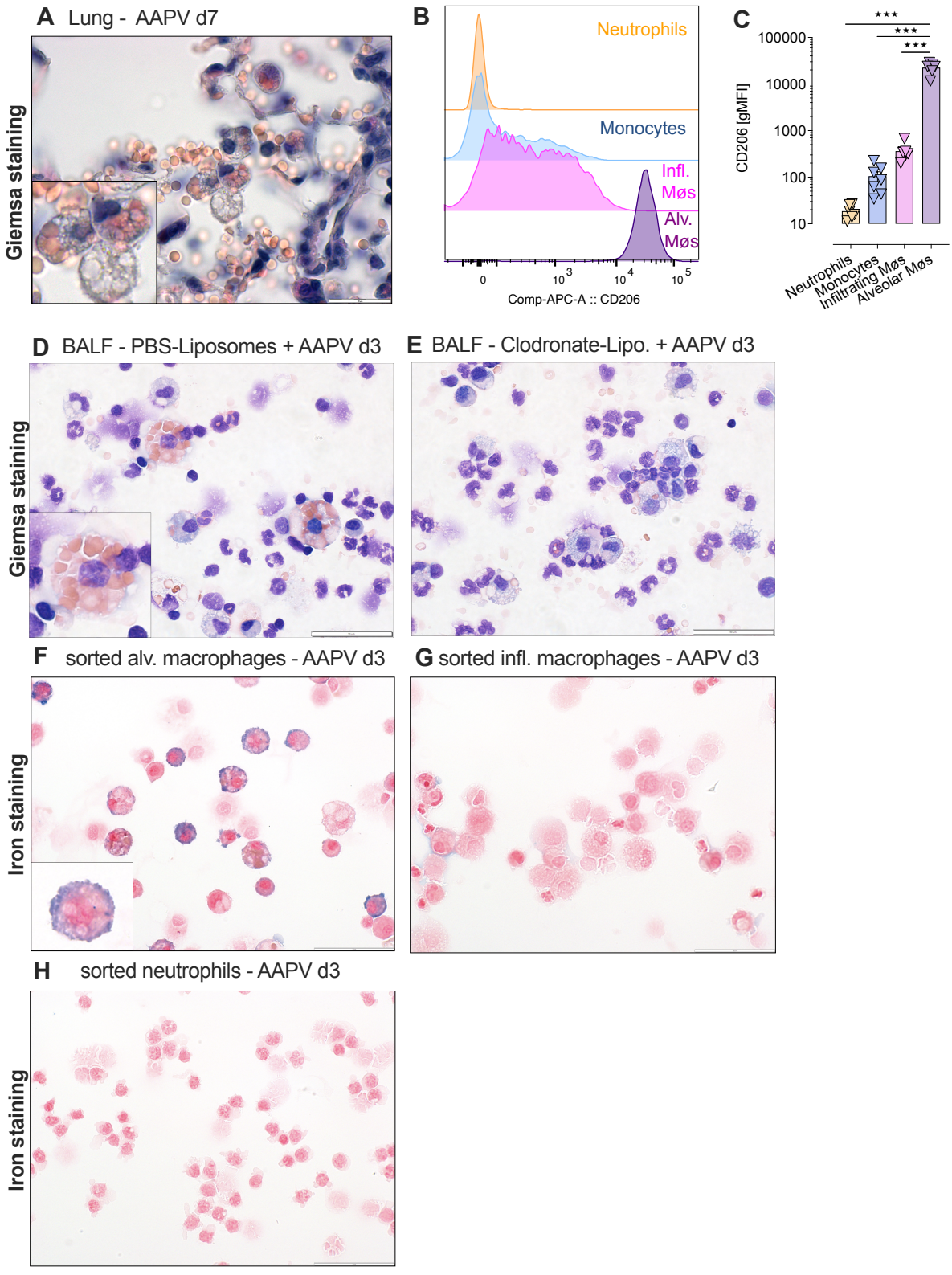

Figure 23: Alveolar macrophages remove red blood cells after AAPV induction. Two days prior to AAPV induction, mice received either Clodronate- or PBS-Liposomes i.t. (50 µl). On d0, AAPV was induced by applying 10 µg fMLP + 10 µg LPS in 50 µl PBS i.t. and 1 mg anti-MPO antibody i.p. (0.5 mg of each clone 6D1 and 6G4). Mice were painlessly killed after five or seven days, and the lungs and BALF were collected. Lung sections were stained with H&E, and cytospins were stained with Giemsa and iron. Additionally, BALF cells were stained for FACS. (**A**) H&E staining of lung sections of mice seven days after

AAPV induction and zoom-in. Image was kindly provided by Prof. Natalio Garbi. (**B-C**) Histogram of CD206 expression by indicated cell population (B) and quantification (C). (**D** and **E**) Giemsa staining of BALF cytospins of the indicated groups. (**F-H**) Iron staining of sorted alveolar macrophages (F), infiltrating macrophages (G), and neutrophils (H). Representative images of at least two independent experiments. (A, D-H) 60x magnification. Scale bar = 20 µm (A) and 50 µm (D-H). Insets show magnified exemplary cells from the original 60x image. The data shown are representative of at least two independent experiments. Mean ± SEM; each symbol represents one mouse. One-way ANOVA, ***$p<0.001$. Experiment was performed with the assistance of Ms. Katharina M. Kirschner, University of Bonn (B-H).

3.3.6. Depletion of alveolar macrophages prolongs AAPV progression

Extracellular heme released by lysed RBCs is a well-known pro-inflammatory danger-associated molecular pattern (DAMP) [204, 205] and, thus, may contribute to inflammation in vasculitis. To elucidate whether removal of extravascular RBCs (hemophagocytosis) by alveolar macrophages contributes toward tissue homeostasis during the recovery phase of AAPV, we depleted AMs by applying Clodronate-Liposomes and investigated disease severity five days after AAPV induction (Figure 24, A). Mice lacking alveolar macrophages (Figure 24, B) had a stronger weight loss than their control counterparts and recovered slower (Figure 24, C). Interestingly, AM-deficiency led to stronger pulmonary hemorrhages on day 5 compared to most mice treated with PBS-Liposomes (Figure 24, D). Contrary to results on day 3 (Figure 22), numbers of monocyte-derived macrophages in the BALF were only slightly increased during the recovery phase (d5) following AM depletion before disease induction (Figure 24, E), suggesting that AMs transiently reduced the size of the monocyte-derived macrophage compartment at the peak of disease. Thus, alveolar macrophages fulfill an anti-inflammatory role during AAPV progression, clearing extravascular RBCs and dampening inflammation in the lung.

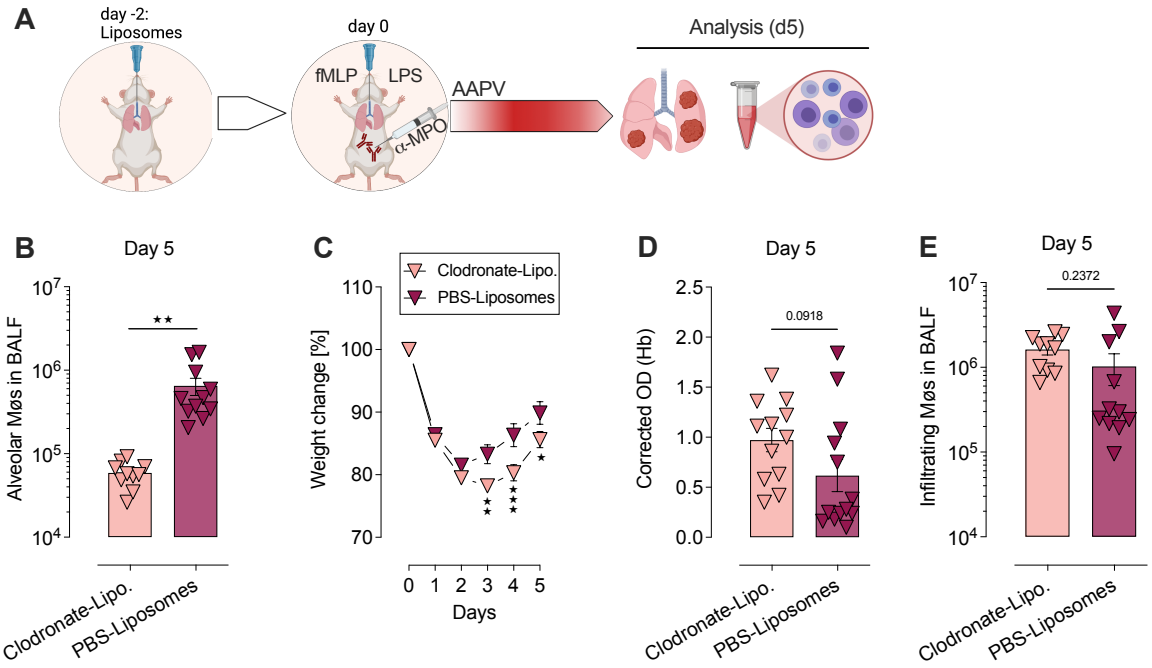

Figure 24: Depletion of alveolar macrophages prolongs AAPV progression. (**A**) Schematic representation of experimental setup. Two days prior to AAPV induction, mice received either Clodronate- or PBS-Liposomes i.t. (50 µl). On d0, AAPV was induced by applying 10 µg fMLP + 10 µg LPS in 50 µl PBS i.t. and 1 mg anti-MPO antibody i.p. (0.5 mg of each clone 6D1 and 6G4). Mice were painlessly killed after five days, the BALF was collected, and hemorrhages and immune cell infiltration were analyzed. (**B**) FACS quantification of alveolar macrophages in BALF of the indicated groups. (**C**) Weight changes over time in the indicated groups. (**D**) Quantification of hemoglobin in BALF. (**E**) FACS quantification of infiltrating macrophages (E) in BALF of the indicated groups. Pooled data are shown from two independent experiments. Mean ± SEM; each symbol represents one mouse. Unpaired student's *t*-test, *p<0.05;**p<0.01; ***p<0.001.

3.3.7. Depletion of alveolar macrophages prolongs AAPV progression in a STING-independent manner

Our results indicate that monocyte-derived infiltrating macrophages are major producers of IFN-β and drive disease pathogenesis. Because these macrophages massively infiltrate the lung upon depletion of alveolar macrophages, we wanted to investigate whether mice lacking AMs develop more pronounced disease progression because of increased nucleic acid sensing by infiltrating macrophages rather than the missing clearance of extracellular RBCs by AMs. Therefore, we depleted alveolar macrophages in STING-deficient mice and investigated disease progression after four days (Figure 25, A). As expected, alveolar macrophages were significantly decreased compared to mice receiving PBS-Liposomes (Figure 25, B). Similar to what we previously observed in wild-type mice, alveolar macrophage-deficiency in STING$^{-/-}$ mice led to severe weight loss (Figure 25, C) and increased pulmonary hemorrhages (Figure 25, D). Additionally, overall leukocyte counts were significantly increased (Figure 25, E), especially infiltrating neutrophils (Figure 25, F). Interestingly, infiltrating macrophages were also increased (Figure 25, G), similar to the results obtained in wild-type mice. Our data suggest that alveolar macrophages contribute to tissue clearance by hemophagocytosis and dampening immune cell infiltration independent of STING/IFN signaling. However, we cannot formally rule out that infiltrating macrophages contribute to inflammation in a STING-independent manner.

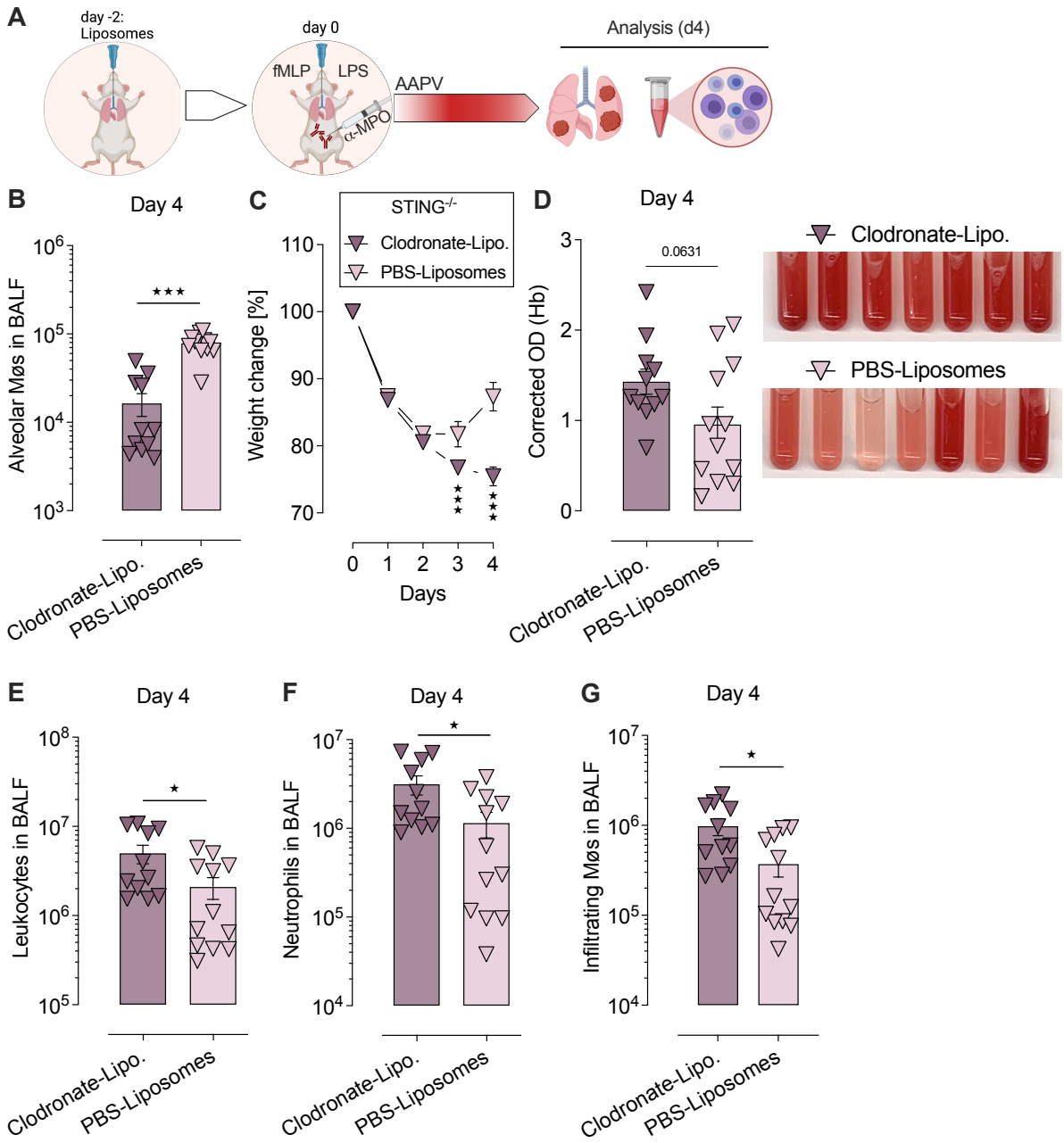

Figure 25: Depletion of alveolar macrophages prolongs AAPV progression in a STING-independent manner. (**A**) Schematic representation of experimental setup. Two days prior to AAPV induction, STING-deficient mice were given either Clodronate- or PBS-Liposomes i.t. (50 µl). On d0, AAPV was induced by applying 10 µg fMLP + 10 µg LPS in 50 µl PBS i.t. and 1 mg anti-MPO antibody i.p. (0.5 mg of each clone 6D1 and 6G4). Mice were painlessly killed after four days, the BALF was collected, and hemorrhages and immune cell infiltration were analyzed. (**B**) FACS quantification of alveolar macrophages. (**C**) Weight changes over time in the indicated groups. (**D**) Quantification and representative images of hemoglobin in BALF. (**E-G**) FACS quantification of leukocytes (E), neutrophils (F), and infiltrating macrophages (G) in the BALF of the indicated groups. Pooled data are shown from two independent experiments. Mean ± SEM; each symbol represents one mouse. Unpaired student's *t*-test, *p<0.05;**p<0.01; ***p<0.001.

3.4.Female sex hormone estradiol ameliorates AAPV progression

3.4.1.Females sustain AAPV longer and have higher disease variability compared to male mice

Autoimmune diseases often occur more frequently in women than men [136], likely because of genetic or hormonal differences. Although overall vasculitis does not present a sex bias, MPO-AAV is slightly more prevalent in women [5]. We, therefore, employed our animal model to investigate a potential sex bias in AAPV disease by directly comparing disease progression in male and female mice (Figure 26, A).

Although female mice lost more weight (Figure 26, B), we did not observe a sex-dependent difference in the average severity of hemorrhages at the peak of the disease (day 3) (Figure 26, C). However, hemorrhages in female mice recovered slower than in males (Figure 26, D and E). In addition, the F-test indicated higher variability in disease severity amongst female mice than male mice during the recovery phase (Figure 26, D and E). Infiltrating leukocytes, however, were unchanged comparing female and male mice throughout the disease (Figure 26, F-H).

These data demonstrate that female mice have higher variability in disease severity and sustain lung hemorrhages for longer periods than their male counterparts. Based on the high variability in disease severity in female mice, our results suggest that hormonal changes rather than other genetic differences between female and male mice more likely contribute to differential disease progression because a genetic impact would rather result in a less variable worsening or amelioration of disease outcome.

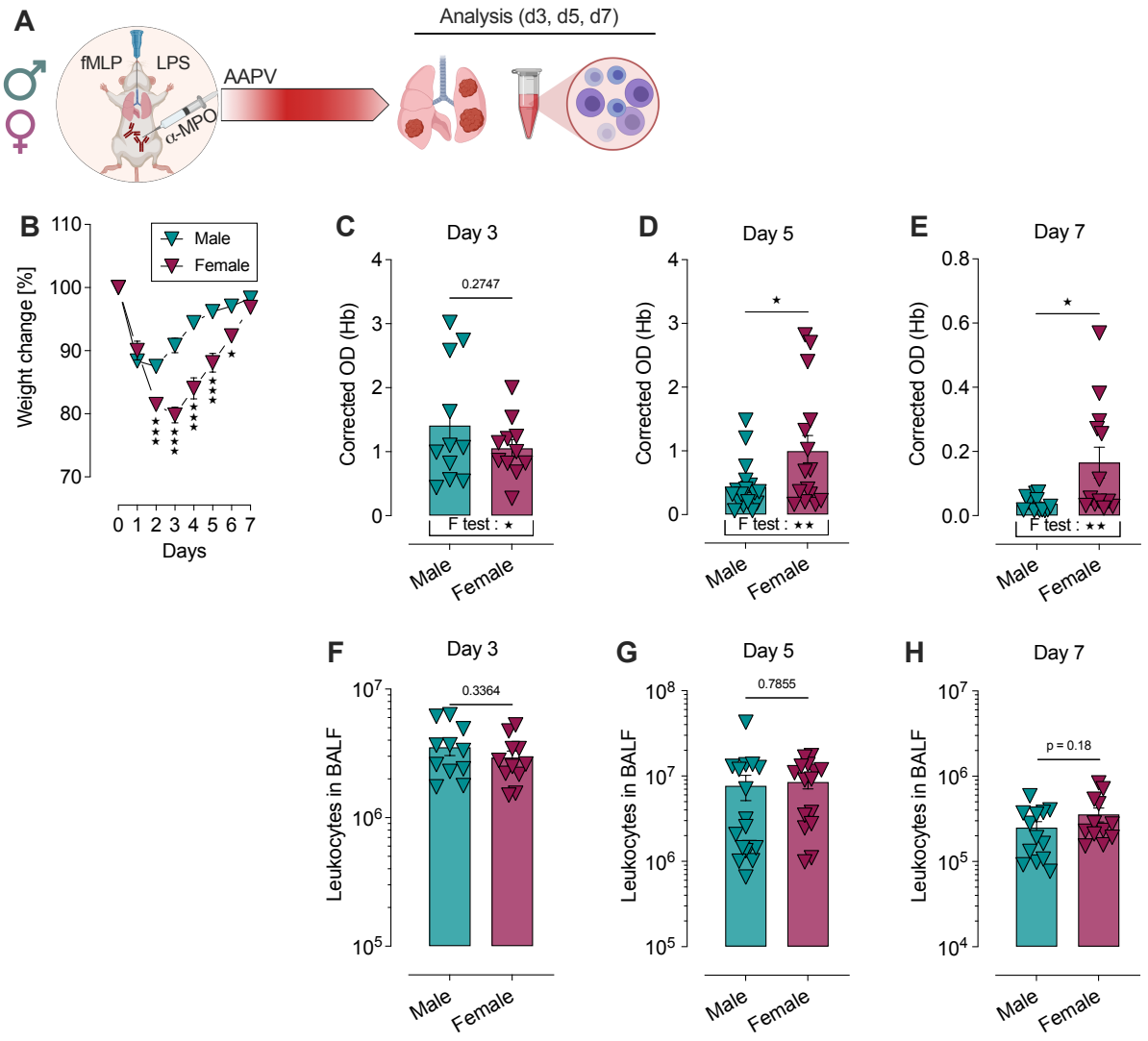

Figure 26: Females sustain AAPV longer and have higher disease variability compared to male mice. (**A**) Schematic representation of experimental setup. On d0, AAPV was induced in female and male C57BL/6J mice by applying 10 µg fMLP + 10 µg LPS in 50 µl PBS i.t. and 1 mg anti-MPO antibody i.p. (0.5 mg of each clone 6D1 and 6G4). Mice were painlessly killed after 3, 5, and 7 days, BALF was collected, and hemorrhages and immune cell infiltration were quantified. (**B**) Weight changes over time in the indicated groups. (**C-E**) Quantification of hemoglobin in BALF on days 3 (C), 5 (D), and 7 (E). (**F-H**) FACS quantification of leukocytes in BALF on days 3 (F), 5 (G), and 7 (H). Pooled data are shown from two independent experiments. Mean ± SEM; each symbol represents one mouse. Unpaired student's *t*-test, *p<0.05; **p<0.01; ***p<0.001.

3.4.2. Disease severity directly correlates with progesterone levels and neutrophil abundance

As we observed a higher variability in disease severity in female compared to male mice, we first investigated whether AAPV severity correlated to the estrus cycle at the time of disease induction. Compared to humans, the equivalent estrus cycle in mice is only 4-5 days long. It can be divided into 4 phases [206]: proestrus, estrus, metestrus, and diestrus - each lasting for about one day (Figure 27, A). Proestrus represents the initial phase of the estrus cycle in which estrogen levels rise and progesterone levels are low. When estrogen levels decrease, and mice ovulate, they enter the estrus phase, at which hormone concentrations are low in the blood. Within metestrus, progesterone levels rise, reaching a peak in diestrus. The specific estrus cycle phase, as determined by cellular analysis of vaginal washes stained with Giemsa (Figure 27, B) (representative images are shown in Appendix Figure 34), revealed no significant correlation with AAPV severity on day 5 (Figure 27, C). Because determining the estrus cycle phase is relatively subjective, we next quantified progesterone levels in the plasma of mice 5 days after AAPV induction, demonstrating a statistically significant correlation with severity of pulmonary hemorrhages (Figure 27, D). Moreover, disease severity correlated with neutrophil abundance in the BALF (Figure 27, E), and higher neutrophil counts in the BALF correlated with higher circulating progesterone levels (Figure 27, F). Thus, our data indicate that disease severity positively correlates with neutrophil infiltration and progesterone concentration in circulation. However, estrogen ELISA was not sensitive enough to quantify hormone concentration in female mice. Thus it remains open whether estrogen levels correlate with disease severity as well.

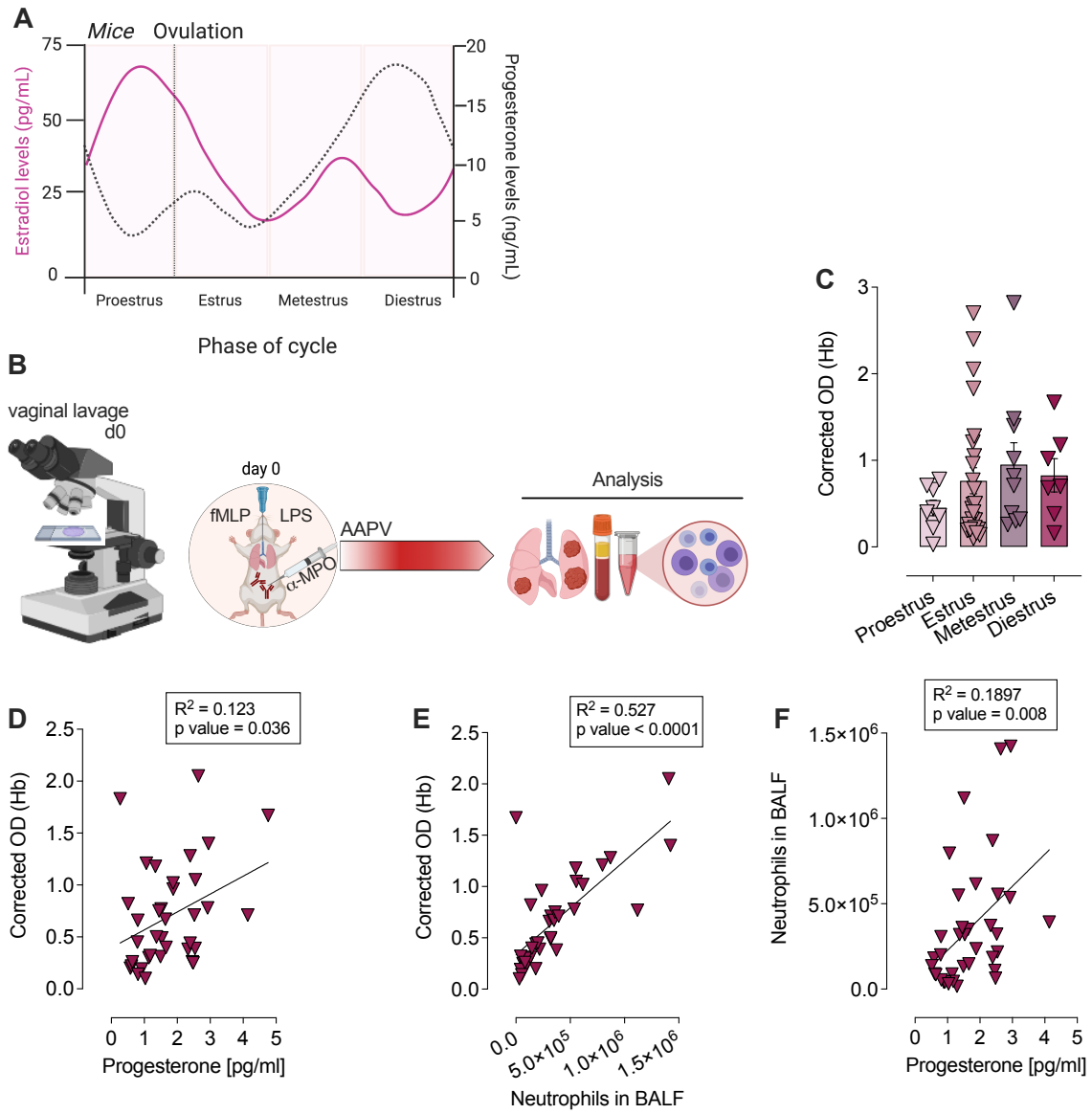

Figure 27: Disease severity directly correlates with progesterone levels and neutrophil abundance. (**A**) Schematic representation of estrogen and progesterone levels during estrus cycle. (**B**) Schematic representation of experimental setup. On d0, vaginal lavage was performed by pipetting PBS on the vaginal opening. Collected cells were transferred to a glass slide and stained with Giemsa, and the estrus cycle phase was determined using a light microscope. Subsequently, AAPV was induced in female C57BL/6J mice by applying 10 µg fMLP + 10 µg LPS in 50 µl PBS i.t. and 1 mg anti-MPO antibody i.p. (0.5 mg of each clone 6D1 and 6G4). Mice were painlessly killed after five days, the BALF was collected, and hemorrhages were analyzed. Additionally, plasma was isolated, and progesterone levels were quantified. (**C**) Quantification of hemorrhages in BALF five days after AAPV induction of mice that were at the indicated estrus phases on day 0. (**D**) Correlation of hemorrhages and circulating progesterone levels on day 5. (**E**) Correlation of hemorrhages and neutrophil numbers in BALF on day 5. (**F**) Correlation of neutrophil numbers in BALF and circulating progesterone levels on day 5. Pooled data are shown from two independent experiments with n=37 mice in total. Mean ± SEM; each symbol represents one mouse. One-way ANOVA (C) and regression analysis (D-F).

3.4.3. Estradiol supplementation in male mice reduces disease progression

In order to investigate whether female sex hormones can affect the disease progression of ANCA-associated vasculitis, we performed interventional gain-of-function experiments. We supplemented male mice with female sex hormones to mimic the female proestrus (high circulating estrogen concentration), diestrus (progesterone), and metestrus (progesterone and estrogen) phases and, thus, elucidate direct hormonal effects on disease progression. For this, we injected estradiol (E2), progesterone (P4), estradiol + progesterone (E2P4), or only vehicle (oil) subcutaneously daily into C57BL/6J male mice, starting 4 days before disease induction (Figure 28, A).

Mice treated with progesterone alone had a normal course of disease in terms of weight loss (Figure 28, B), hemorrhages (Figure 28, C), and leukocytes in the BALF (Figure 28, D and E). However, mice that were treated either with E2 or the combination of E2P4 recovered faster from weight loss (Figure 28, B) and had decreased pulmonary hemorrhages (Figure 28, C) as well as fewer overall leukocytes in the BALF (Figure 28, D), 3 days after disease induction. When quantifying different immune cell populations, we observed that E2 alone and in combination with P4 reduced numbers of classical neutrophils significantly (Figure 28, E) but had no major effect on infiltrating monocyte-derived macrophages (Figure 28, F), alveolar macrophages (Figure 28, G) and classical monocytes (Figure 28, H).

Our previous experiments demonstrated that DNA sensing and subsequent STING activation promoted AAPV severity (Figure 16). Hormonal supplementation in male mice did not significantly change DNA release into the BAS (Figure 28, I), suggesting that E2 does not ameliorate disease progression by limiting extracellular DNA accumulation as a potential agonist for STING-mediated nucleic acid sensing.

Hence, P4 supplementation did not affect disease progression, but E2 was sufficient to ameliorate hemorrhages and dampened inflammation independently of P4 co-administration.

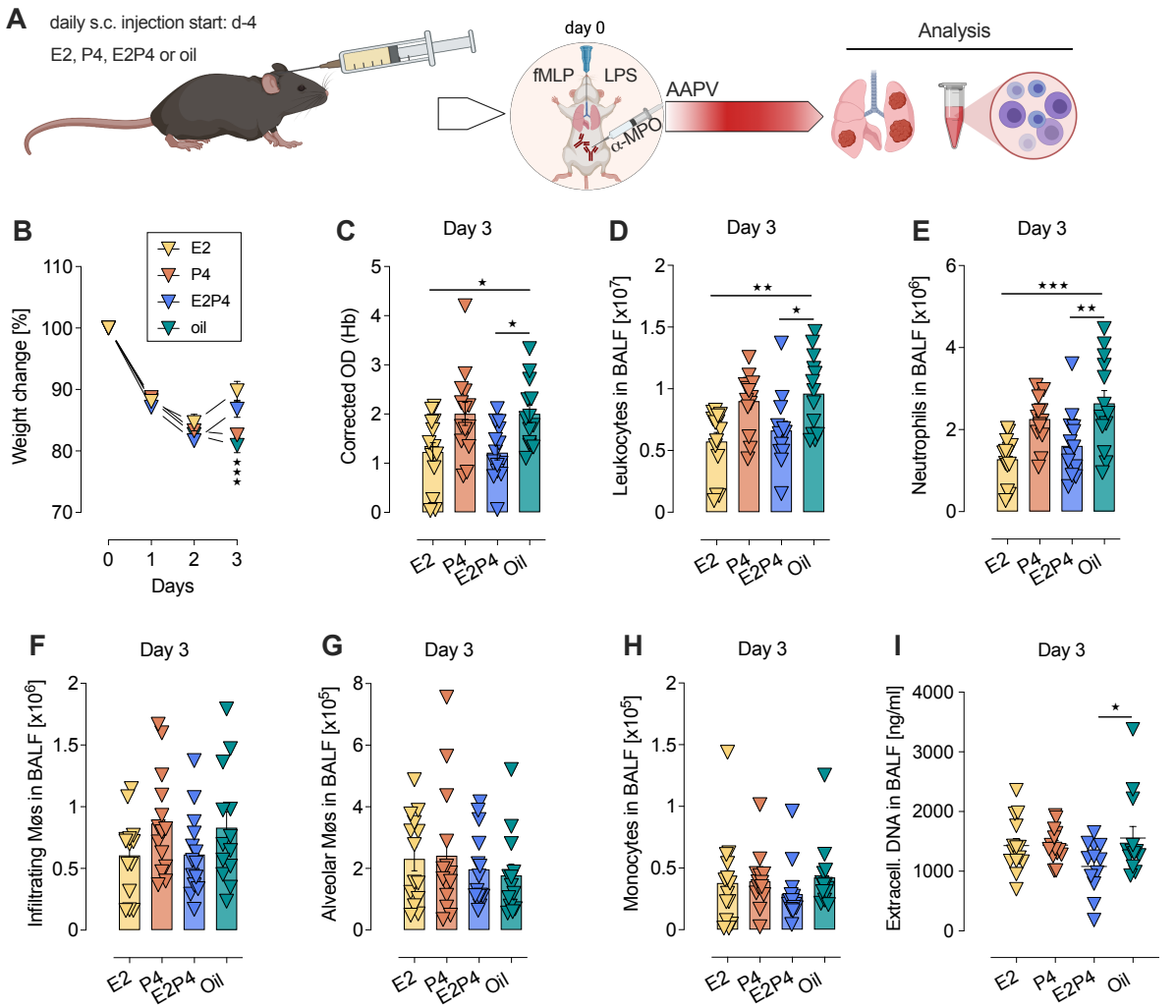

Figure 28: Estradiol supplementation in male mice reduces disease progression. (**A**) Schematic representation of experimental setup. Four days before AAPV induction, male mice were supplemented with female hormones estradiol (E2), progesterone (P4), estradiol + progesterone (E2P4), or vehicle (oil) by subcutaneous injection. On d0, AAPV was induced by applying 10 µg fMLP + 10 µg LPS in 50 µl PBS i.t. and 1 mg anti-MPO antibody i.p. (0.5 mg of each clone 6D1 and 6G4). Mice were painlessly killed after three days, the BALF was collected, and hemorrhages, immune cell infiltration, and extracellular DNA were analyzed. (**B**) Weight changes over time in the indicated groups. (**C**) Quantification of hemoglobin in BALF. (**D-H**) Quantification of total leukocytes (D), neutrophils (E), infiltrating macrophages (F), alveolar macrophages (G), and monocytes (H) in BALF of the indicated groups. (**I**) Quantification of extracellular DNA in BALF. Hormone enrichment was confirmed in the plasma on day 3 (Appendix Figure 39). Pooled data are shown from two independent experiments. Mean ± SEM; each symbol represents one mouse. One-way ANOVA compared to oil, *p<0.05; **p<0.01.

3.4.4. Estradiol supplementation in female mice ameliorates disease progression

To exclude confounding effects from genetic differences between females and males beyond sexual hormones affecting disease progression, we performed hormonal supplementation in females which were previously ovariectomized to disrupt natural hormone production and oscillation. After three weeks, hormone levels were decreased to a basal level, which was confirmed via ELISA (Appendix Figure 40). Mice were supplemented with estradiol and/or progesterone or vehicle alone by subcutaneous injection starting four days before disease induction (Figure 29, A). We could confirm that E2 and E2/P4 treatment ameliorated the well-being of mice (Figure 29, B) and somewhat decreased pulmonary hemorrhages, although not reaching statistical significance (Figure 29, C). E2/P4 treatment also tended to reduce cell-free DNA in BALF (Figure 29, D), as observed in supplemented males. However, contrary to supplementation in males, leukocyte numbers in the BALF did not change upon hormonal treatment in ovariectomized females (Figure 29, E).

Thus, our preliminary data suggest that estradiol ameliorates AAPV disease independently of potentially confounding genetic differences between males and females.

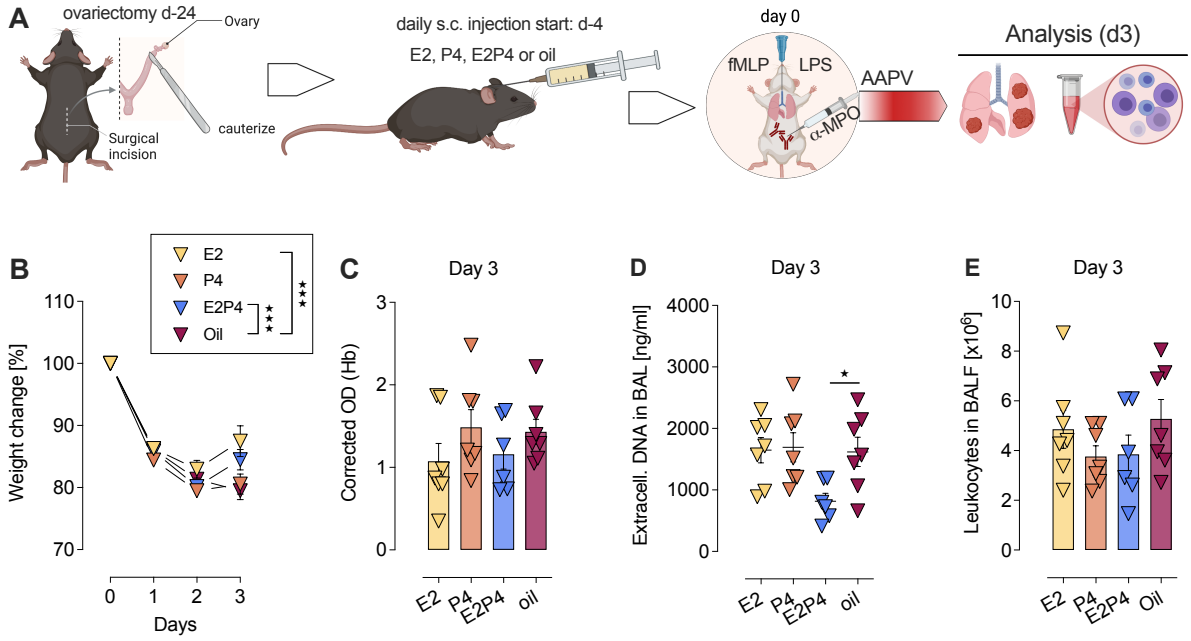

Figure 29: Estradiol supplementation in female mice ameliorates disease progression. (**A**) Schematic representation of experimental setup. Female mice were ovariectomized on day -21 to reduce circulating hormone levels. Four days before AAPV induction (d-4), female mice were supplemented with estradiol (E2), progesterone (P4), estradiol + progesterone (E2P4), or vehicle (oil) by subcutaneous injection. On d0, AAPV was induced by applying 10 µg fMLP + 10 µg LPS in 50 µl PBS i.t. and 1 mg anti-MPO antibody i.p. (0.5 mg of each clone 6D1 and 6G4). Mice were painlessly killed after three days, the BALF was collected, and hemorrhages, extracellular DNA, and immune cell infiltration were analyzed. Blood was taken on d0 and d3 to confirm hormone supplementation by ELISA (Appendix Figure 40). (**B**) Weight changes over time in female mice after ovariectomy and hormone supplementation. (**C**) Quantification of hemoglobin in BALF of the indicated groups. (**D**) Quantification of extracellular DNA in BALF. (**E**) Quantification of leukocytes in BALF. Data are shown from one experiment. Mean ± SEM; each symbol represents one mouse. One-way ANOVA compared to oil, *p<0.05; ***p<0.001.

3.4.5. Unaltered endothelial cell proliferation in estradiol-treated mice

A well-known role of estradiol is its contribution to rebuilding the endometrium after menstruation by promoting proliferation of epithelial cells [207, 208]. Thus, we hypothesized that estradiol counteracts AAPV progression by inducing endothelial proliferation of damaged blood vessels in the lung. To investigate this, we ovariectomized female mice, supplemented them with estradiol or progesterone, and induced vasculitis. Flow cytometric analysis of the proliferation marker Ki-67 three days after AAPV induction revealed no significant differences in the frequency of proliferating Ki-67$^+$ endothelial cells (EnCs) in hormone-supplemented female mice compared to their non-supplemented counterparts (Figure 30, A and B). Additionally, epithelial cells (EpCs) did not differentially proliferate (Figure 30, A and C). Interestingly, CD4$^+$ T cells, which served as a positive control for proliferation, proliferated less upon progesterone treatment than the vehicle-treated group (Figure 30, A and D). However, this most likely is not important for AAPV progression as we didn't see any physiological differences upon progesterone treatment compared to the vehicle control. Thus, this data indicate that E2 did not counteract AAPV progression by promoting endothelial or epithelial cell proliferation at the disease peak (day 3).

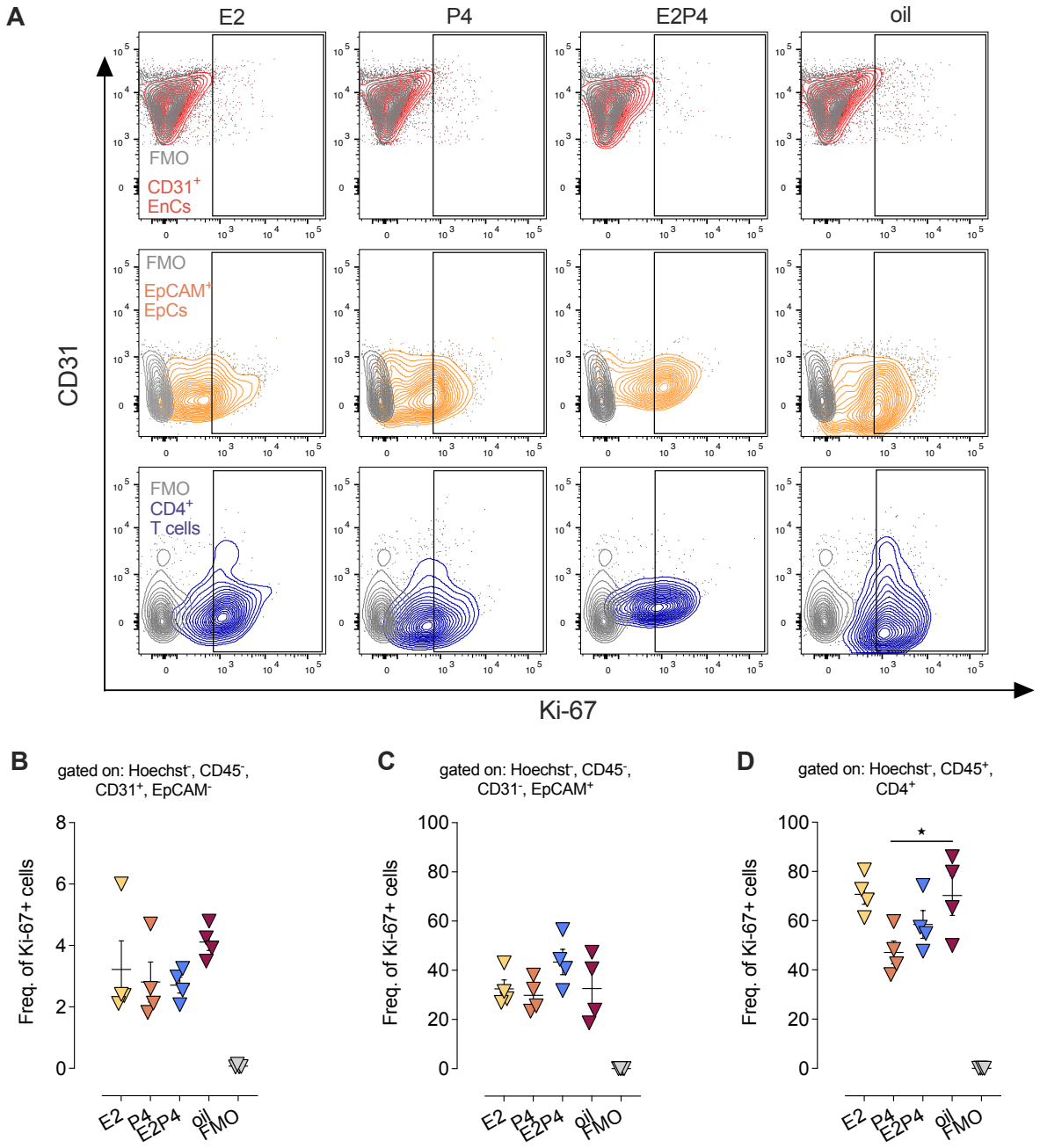

Figure 30: Unaltered endothelial cell proliferation in estradiol-treated mice. Female mice were ovariectomized on day -21 to reduce circulating hormone levels. Four days before AAPV induction (d-4), mice were supplemented with estradiol (E2), progesterone (P4), estradiol + progesterone (E2P4), or vehicle (oil) by subcutaneous injection. On d0, AAPV was induced by applying 10 µg fMLP + 10 µg LPS in 50 µl PBS i.t. and 1 mg anti-MPO antibody i.p. (0.5 mg of each clone 6D1 and 6G4). Mice were painlessly killed after three days, and lungs were digested and samples stained intracellularly for Ki-67. (**A**) FACS contour blots of Ki-67 expression in endothelial cells (EnCs), epithelial cells (EpCs), and T cells of mice with AAPV. (**B-D**) Quantification of frequency of Ki-67$^+$ EnCs (B), EpCs (C), and CD4$^+$ T cells (D). Experiment was performed only once. Data shown as mean ± SEM; each symbol represents one mouse. FMO - fluorescence minus one. One-way ANOVA compared to oil, *p<0.05.

3.4.6. Estradiol supplementation reduces circulating immune cells in steady-state

Our results suggest that estradiol dampens disease progression by a mechanism other than promoting the proliferation of endothelial or epithelial cells to repair damaged blood vessels or bronchi. Therefore, we investigated whether sex hormones affect the immune system itself. For this, female mice were ovariectomized, and female and male mice were supplemented with E2 and/or P4 or vehicle control for four days. Circulating immune cells were quantified in the blood. While numbers of classical neutrophils were unchanged upon hormone supplementation (Figure 31, B), NK cells, monocytes, and B cells were decreased upon E2 and E2/P4 treatment compared to mice receiving only vehicle. In contrast, P4 supplementation alone, did not alter circulating immune cell numbers (Figure 31, C-E)

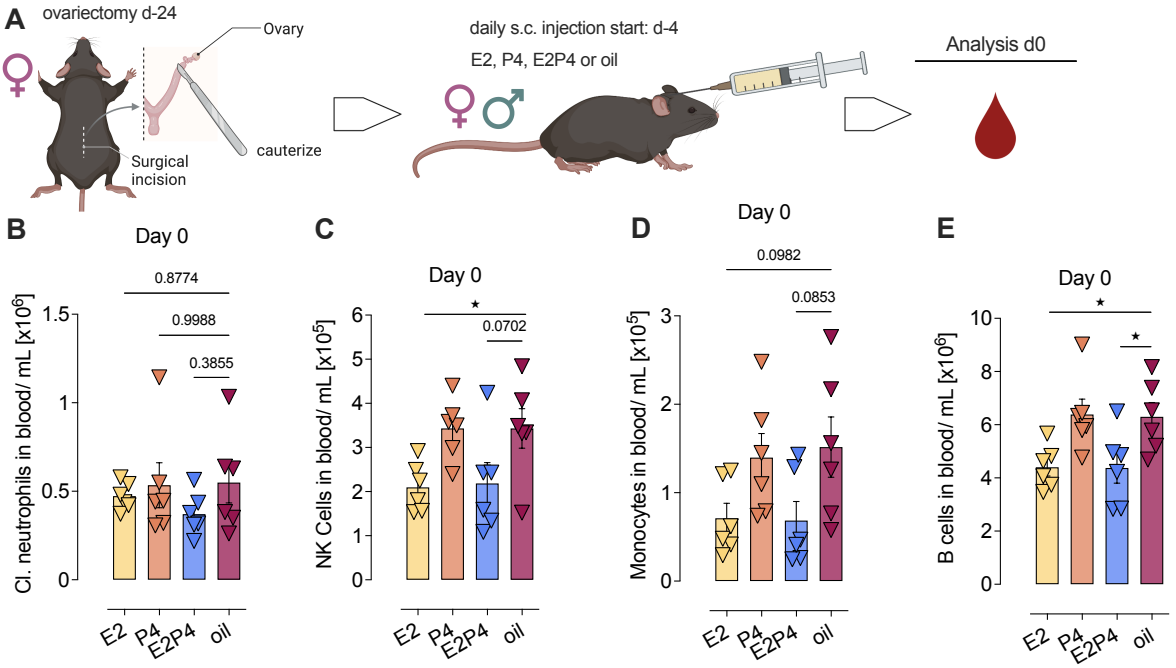

Figure 31: Estradiol supplementation reduces circulating immune cells in steady-state. (**A**) Schematic representation of experimental setup. Female mice were ovariectomized on day -21 to inhibit hormone production. Four days before AAPV induction (d-4), female and male mice were supplemented with estradiol (E2), progesterone (P4), estradiol + progesterone (E2P4), or vehicle (oil) by subcutaneous injection. On d0, mice were painlessly killed, blood was collected, and circulating immune cells were analyzed. (**B-E**) Quantification of classical neutrophils (B), NK cells (C), monocytes (D), and B cells (E) in the blood of the indicated groups. ELISA confirmed hormone enrichment in the plasma on day 0 in female mice (Appendix Figure 40). Data are pooled from two independent experiments. Mean ± SEM; each symbol represents one mouse. One-way ANOVA compared to oil, *p<0.05.

3.4.7. Estradiol decreases ROS production in lung neutrophils during AAPV disease

Estradiol has been shown to inhibit superoxide release and NADPH oxidase activity in vascular smooth muscle cells of ovariectomized mice, while progesterone induced the release of ROS [209]. Having seen that NADPH oxidase-deficiency ameliorates AAPV disease progression (previous Figure 13), we wanted to investigate whether the protective effect of estradiol that we observe in AAPV is associated with altered ROS production. For this purpose, female mice were ovariectomized and supplemented with E2, P4, E2P4, or only vehicle. ROS production by neutrophils was analyzed in the blood before disease onset and in BALF three days after disease induction. On day 0 before disease induction, we found decreased ROS production in blood neutrophils upon estradiol or progesterone single treatment. In contrast, the combinatory treatment of the two hormones did not differ from the vehicle control (Figure 32, A-C). Three days after disease induction, classical neutrophils in the BALF still produced less spontaneous ROS upon estradiol treatment (Figure 32, D-F) which was not the case for Siglec-F^{+} neutrophils (Figure 32, G-I).

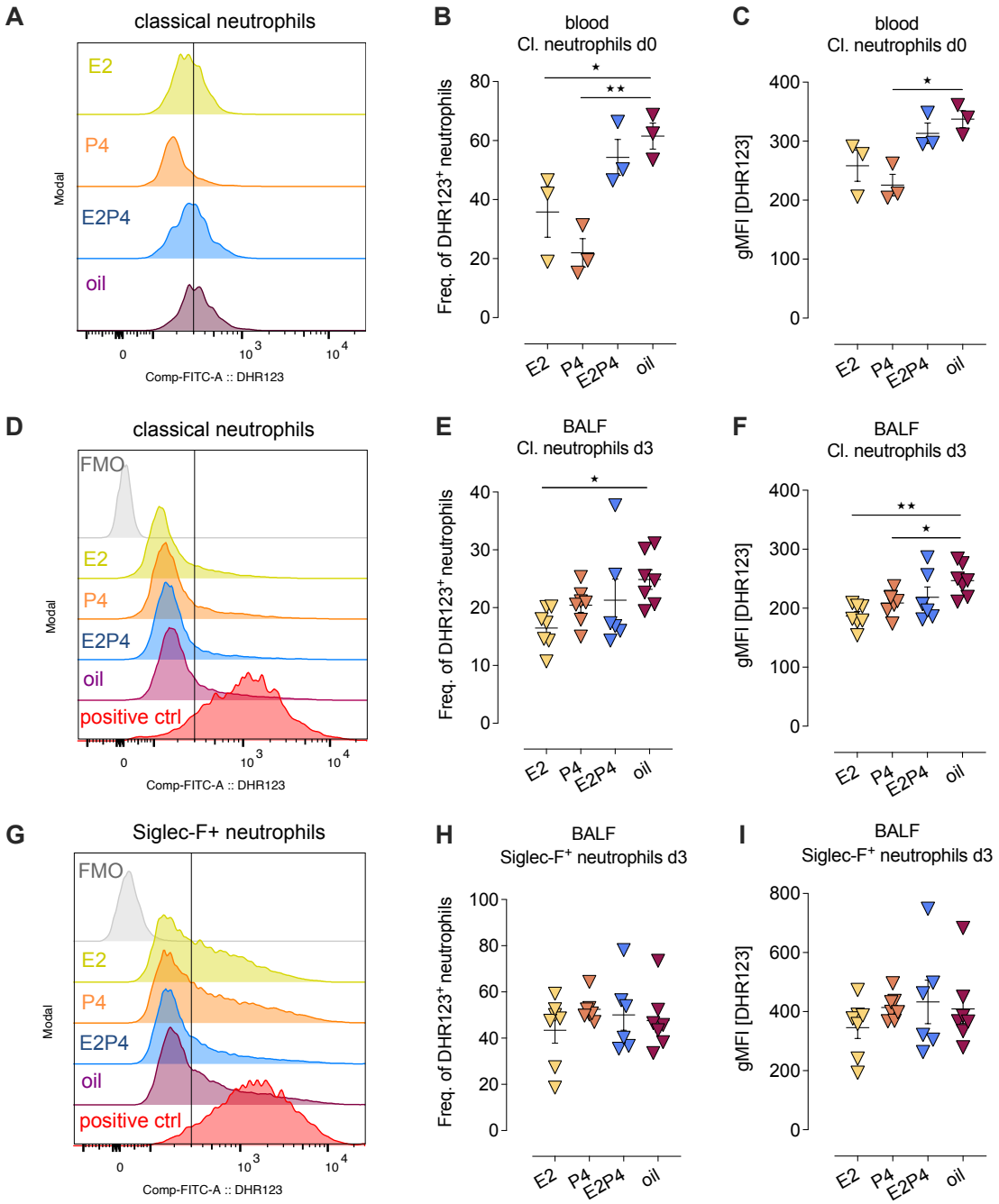

Figure 32: Estradiol decreases ROS production in lung neutrophils during AAPV disease. Female mice were ovariectomized on day -21 to reduce circulating hormone levels. Four days before AAPV induction (d-4), female mice were supplemented with estradiol (E2), progesterone (P4), estradiol + progesterone (E2P4), or vehicle (oil) by subcutaneous injection. On d0, AAPV was induced by applying 10 µg fMLP + 10 µg LPS in 50 µl PBS i.t. and 1 mg anti-MPO antibody i.p. (0.5 mg of each clone 6D1 and 6G4). Mice were painlessly killed on d0 or three days after disease induction, blood and BALF were collected, and ROS production in different neutrophil subsets was quantified. Positive control was treated with PMA before DHR123 staining. (**A-C**) Histogram (A), frequency (B), and gMFI (C) of DHR123 positive classical neutrophils in blood on d0. (**D-F**) Histogram (D), frequency (E), and gMFI (F) of DHR123 positive classical neutrophils in BALF on d3. (**G-I**) Histogram (G), frequency (H), and gMFI (I) of DHR123 positive Siglec-F+ neutrophils in BALF on d3. Experiment was performed only once. Data is shown as mean ± SEM; each symbol represents one mouse. One-way ANOVA compared to oil, *p<0.05, **p<0.01.

3.4.8.Cytokine expression in BALF of mice with AAPV

To further investigate disease pathogenesis and how estradiol ameliorates AAPV progression, we analyzed the release of cytokines in the bronchoalveolar space using a proteome profiler array that allows quantification of 111 different cytokines. First, we investigated cytokine release upon vasculitis induction in comparison to naive mice or mice treated with anti-MPO or fMLP+LPS only at the peak of the disease (day 3). For each group, a sample with an average level of hemorrhages within its group was chosen, quantified by OD. While there were no detectable cytokines in BALF of naive mice or those treated only with anti-MPO, we found increased cytokine levels after fMLP+LPS challenge (Figure 33, A and B). Upon vasculitis induction, we observed an up-regulation, compared to fMLP+LPS, of P- and E-Selectin, which are essential for neutrophil rolling, as well as, e.g., CCL12 which specifically attracts eosinophils, monocytes, and lymphocytes. We further observed increased expression of the B cell attractant CXCL13 and the B cell activator BAFF. Moreover, MMP-3 and -9 were highly increased upon AAPV induction compared to the fMLP+LPS challenge (Figure 33, C and D). In contrast, we also found numerous down-regulated cytokines in mice with AAPV. CXCL2 or GM-CSF, which are potent neutrophil and macrophage attractants, were strongly decreased, the same as, e.g., CD14 which binds LPS in the presence of LPS-binding protein (LBP) (Figure 33, E).

Having observed that estradiol ameliorates disease progression and that this is apparently not because of increased vessel repair by endothelial cell proliferation, we aimed to elucidate whether estradiol regulates cytokine production in mice with AAPV. Therefore, we collected BALF supernatant of male mice supplemented with female hormones and performed a proteome profiler array. We found only six cytokines up-regulated upon estradiol treatment compared to oil-treated mice, including LIX, IL-12, BAFF, CCL12, ICAM-1, and PDGF-BB (Figure 33, F and G). Most of the detectable cytokines were down-regulated upon estradiol treatment, including MMP-9 and -3, as well as IL-6 (Figure 33, F and H), supporting the hypothesis that estradiol acts as an anti-inflammatory mediator. However, identified candidates like the metalloproteases would have to be analyzed more in-depth to investigate their involvement in disease pathogenesis.

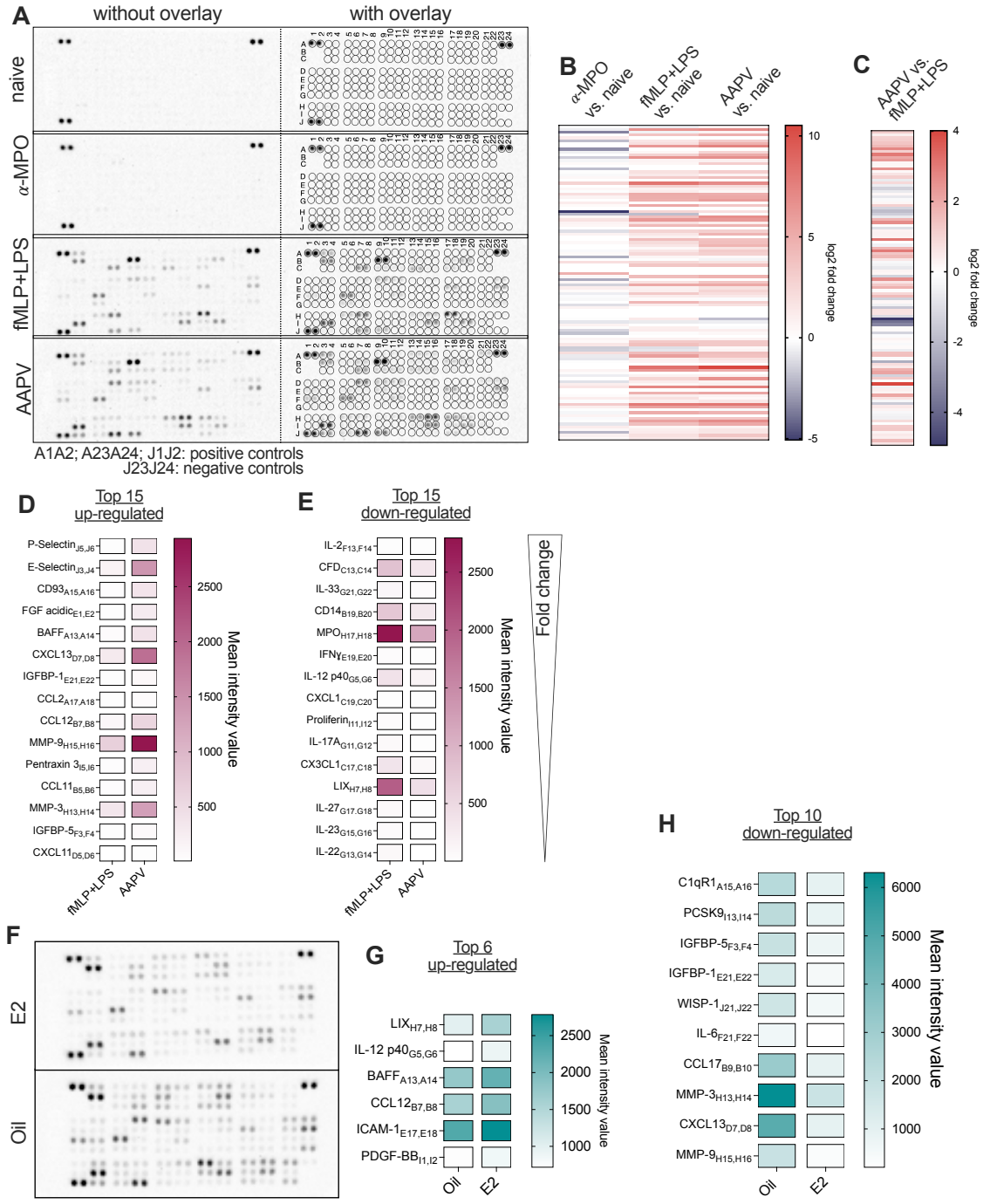

Figure 33: Cytokine expression in BALF of mice with AAPV. (**A**) Picture of proteome profiler array membranes incubated with BALF supernatant of female mice which received 10 µg fMLP + 10 µg LPS in 50 µl PBS i.t. and 1 mg anti-MPO antibody i.p. (0.5 mg of each clone 6D1 and 6G4). Naive mice, anti-MPO, and fMLP+LPS-only treated mice served as control. Mice were painlessly killed after three days, and BALF was collected to quantify cytokines. (**B** and **C**) Fold change of gene expression of the indicated groups compared. (**D** and **E**) Top 15 cytokines that were up-regulated (D) and down-regulated (E) in BALF of mice with AAPV compared to fMLP+LPS treated mice. (**F**) Pictures of proteome profiler array membranes incubated with BALF of male mice treated with estradiol or oil four days before AAPV induction. BALF was collected three days after AAPV induction. (**G**) Top 6 cytokines that were up-regulated in BALF of estradiol-treated mice in comparison to oil. (**H**) Top 10 cytokines that were down-regulated in BALF of estradiol-treated mice in comparison to oil. Data are shown from one experiment.

4. Discussion

This thesis aimed to investigate the molecular and cellular mechanisms promoting ANCA-associated vasculitis in order to elucidate new therapeutic targets. Previous studies have investigated the requirement of neutrophils and ANCA in disease induction. Upon priming, e.g., by an infection and subsequent activation by ANCA, neutrophils extrude granule content and DNA that accumulate in the circulation and at the site of inflammation. However, whether and how this might trigger disease pathogenesis remains to be elucidated. As the current therapy strategies focus on general and sustained immunosuppression, entailing severe side effects, there is an urgent need to identify specific mechanisms involved in disease pathogenesis that may be therapeutically targeted.

4.1. Combination of fMLP+LPS and anti-MPO induces severe pulmonary vasculitis in mice

Clinical observations that patients with AAPV have increased circulating ANCA levels [10] and that disease relapses are often associated with rising ANCA levels [210-212] suggest a crucial role of anti-MPO IgGs in disease development. Consistently with this, B cell depletion [75, 213] and plasma exchange therapies [214] that lower circulating antibody titers are beneficial for patients with AAV. Currently available mouse models for ANCA-associated vasculitis use active or passive transfer of ANCA [45, 81, 215]. To circumvent the mild disease induction and poor reproducibility associated with these models [216], researchers have boosted neutrophil activation with LPS to mimic common infections preceding vasculitis flares in patients, leading to increased disease severity in these models [82]. Despite increased severity, disease penetrance is still poor [216]. In addition, these preclinical models are mostly restricted to kidney pathology [85]. Although kidney involvement is a severe complication, there are no consistent mouse models for pulmonary hemorrhages, which is amongst the most lethal complication during AAV surges of ANCA-associated vasculitis [85]. Therefore, we established a mouse model reflecting severe clinical lung pathology in AAV. By applying low doses of the bacterial ligands fMLP and LPS into the lung and systematically injecting two

monoclonal anti-MPO IgGs, mice developed severe pulmonary hemorrhages and lung pathology within three days. fMLP was needed to increase circulating neutrophil numbers, while LPS led to activation of neutrophils and their subsequent extravasation into the lung [189]. Although fMLP+LPS also increased immune cell infiltration, it only induced a low grade of lung pathology, and mice never developed pulmonary hemorrhages. Like in most clinical cases, disease in our model is transient, and mice with AAPV cleared most of the hemorrhages by day seven after disease induction. Fast recovery from hemorrhages may be due to the single application of anti-MPO antibodies in our model, which stands in contrast to patients with AAV who continuously produce autoantibodies [217].

4.2. Neutrophils maturation in the inflammatory lung environment is indicated by Siglec-F expression

Depletion of circulating neutrophils prevented necrotizing and crescentic glomerulonephritis, proving the essential role of neutrophils in AAV pathogenesis [82]. In our model, we observed massive infiltration of neutrophils in the lung of mice with AAPV as soon as 6 hours after disease induction. Whereas neutrophils are classically characterized as Siglec-F$^-$ Ly-6G$^+$, we found that infiltrating neutrophils in the lung - identified by the polymorphic nucleus and transparent cytoplasm - expressed Siglec-F by day three. In contrast to fMLP+LPS treated mice, Siglec-F$^+$ cells accumulated in the bronchoalveolar space. Additionally, blood neutrophils remained Siglec-F$^-$, indicating that neutrophils up-regulated this marker when infiltrating the lung environment. Siglec-F$^+$ neutrophils were previously identified in a mouse model of lung adenocarcinoma, where osteoblasts remotely supplied the tumor site with these cells promoting cancer processes, e.g., tumor growth, angiogenesis, and immunosuppression [218]. Siglec-F$^+$ neutrophils at the tumor site showed increased ROS production and promoted macrophage differentiation *in vivo* [218]. Further characterization of this neutrophil subset by the group of Mikael Pittet identified it as mature, non-proliferating, and long-lived [219].

This is in line with our findings that Siglec-F$^+$ neutrophils displayed a darker chromatin staining than classical neutrophils, indicating more condensed chromatin, a hallmark of neutrophil maturation [195]. This suggests that Siglec-F$^+$ neutrophils are less transcriptionally active, as DNA transcription is less efficient when densely packed. Furthermore, our data revealed that most of the differentially expressed genes in Siglec-F$^+$ neutrophils were down-regulated compared to classical neutrophils. The gene that decreased the strongest was *Camp,* encoding for LL-37, a protein previously shown to be elevated in the serum of patients with AAV [220]. In psoriasis, LL-37-decorated DNA acted as a potent inflammatory trigger activating pDCs [221], and its role in AAV will be further discussed in the Discussion section 4.3.. *Bcl6*, which was also strongly decreased in Siglec-F$^+$ neutrophils, has been shown to prevent tissue neutrophil apoptosis during pulmonary inflammation [222].

In contrast, *Cdkn1a* is one of the genes highly up-regulated in Siglec-F$^+$ neutrophils. *Cdkn1a* encodes for the protein p21, which was previously shown to cause neutrophil apoptosis [223]. Under resting conditions, neutrophils express only low levels of *Cdkn1a* [224]; however, human airway neutrophils had about 140-fold increased expression upon endotoxin exposure [225]. This data supports the idea that this neutrophil subset reached a terminal differentiation and the end of their lifespan. However, whether Siglec-F$^+$ neutrophils contribute to inflammation or resolution in ANCA-associated vasculitis remains to be investigated.

The production of ROS is a crucial mediator in many inflammatory diseases. We observed high levels of ROS in lung neutrophils upon induction of pulmonary AAV. What was surprising was the fact that NADPHox-deficiency ameliorated only pulmonary hemorrhages but had no effect on immune cell infiltration three days after disease induction. It may be that ROS directly targets the endothelium and induces cell death, resulting in hemorrhages in the lung. For instance, excess ROS inhibits nitric oxide (NO) production, resulting in endothelial dysfunction [226]. Additionally, ROS can trigger apoptotic signaling pathways in liver endothelial cells by degrading their polysaccharide-coated surface layer [227], thus supporting our hypothesis of ROS-induced endothelial death and subsequent hemorrhage induction. However, ROS may play a dual role in the pathogenesis of AAPV, as

NADPHox-deficiency reduced the number of alveolar macrophages in the BALF, which we found to be essential for clearance of hemorrhages in AAPV. It was previously shown that ROS produced by neutrophils is required to trigger the conversion of macrophages to a pro-resolving phenotype in an APAP-induced liver injury model [228]. Therefore, ROS-deficiency might protect from pulmonary hemorrhages but prevent dampening of inflammation and resolution of disease at a later time point, which has not been investigated in this study.

4.3. Nucleic acid sensing via the STING/IFN axis drives AAPV progression

Previously, it has been shown that NADPH oxidase activity and ROS production can drive NETosis [31], and high concentrations of ROS were found to cause neutrophil death [229, 230]. NETosis and aberrant DNA release have been demonstrated in several autoimmune diseases, including AAV, where these mechanisms are believed to be involved in disease pathogenesis [24-26]. We also detected increased extracellular DNA levels in the BALF upon applying our mouse model. However, whether increased extracellular DNA levels and NADPH-oxidase-driven pathogenesis are directly linked in AAPV still needs to be investigated as we did not quantify extracellular DNA in gp91phox-deficient mice.

Interestingly, treatment with the bacterial ligands fMLP+LPS alone already provoked a similar DNA release to AAPV induction but without inducing pulmonary hemorrhages. We hypothesize that anti-MPO antibodies form immune complexes with neutrophilic MPO-decorated DNA and that the antibodies are required for shuttling the DNA into the cell. Indeed, anti-MPO antibodies used in this study bound MPO-decorated DNA released by neutrophils in an *in vitro* NETosis assays (Dr. L. L. Teichmann, pers. comm.). Although we do not have direct proof for DNA shuttling in AAPV, other studies have proposed a similar mechanism. For instance, cytosolic delivery of extracellular DNA has been shown to provoke IFN-α expression *in vitro*, although the mechanism of DNA uptake was not elucidated [231]. In another study, immune complexes with DNA were translocated to the cytosol via Fc receptor binding, driving monocyte activation and subsequent IL-1β production [232].

Besides antibodies, other proteins have been reported to shuttle DNA into the cytosol. LL-37 was demonstrated to bind DNA and transport it into the cytoplasm resulting in STING activation in myeloid cells *in vitro* [231] or TLR9 activation in pDCs during psoriasis [221]. LL-37 was further implicated in the pathogenesis of several autoimmune diseases like psoriasis [233] or SLE [234]. In this study, classical neutrophils in mice with AAPV expressed high levels of *Camp*, suggesting that LL-37 might shuttle neutrophilic DNA in our vasculitis model. In line with this, Kessenbrock et al. found LL-37-decorated DNA to drive renal damage in AAV [24]. However, whether ANCA increase the expression of LL-37 which mediates pathogenic DNA shuttling remains to be investigated.

Cytosolic DNA gets sensed by nucleic acid sensors triggering a pro-inflammatory response, for instance, the expression of type-I IFNs. IFNs are crucial players promoting immunity during infections (reviewed in [235]), but they also play important roles in autoimmune diseases [236, 237]. For instance, IFN signature in peripheral blood mononuclear cells (PBMCs) of patients with SLE correlated positively with disease severity [238]. Recently, it has been shown that NETs are phagocytosed, inducing cGAS-dependent IFN secretion [15]. In our group, we have demonstrated that nucleic acid sensing via the STING/IFN-I axis promotes severe AAPV pathogenesis. Increased cGAMP levels and an enhanced IFN signature in PBMCs of patients with AAV supported the role of nucleic acid sensing also in human disease [189]. These findings are consistent with data obtained from TREX1-knockout mice, mimicking Aicardi-Goutieres syndrome, a STING-dependent interferonopathy induced by TREX1 DNase-deficiency [95].

However, results in other publications are, apparently, in contradiction with our findings. Although patients with STING-associated vasculopathy with onset in infancy (SAVI), which is driven by a self-activating STING mutation, show an IFN-I signature, disease in the corresponding mouse model is not ameliorated by a deficiency in IRF3 or IFNAR-1 [190]. Additionally, Motwani et al. did not observe a substantial increase in the expression of ISG by gain-of-function STING mutations [239]. Altogether, our results indicate that the disease mechanisms driven by

chronic STING activation, like in SAVI, differ from those in acute STING activation, like in AAV.

Another study investigating ISG expression by PBMCs did not observe any differences between patients with AAV and healthy controls [240]. However, they examined the expression of only 7 ISGs (*ISG15*, *SIGLEC1*, *STAT1*, *RSAD2*, *IFI27*, *IFI44L,* and *IFIT1),* which were, besides *IFI27,* also not differentially expressed in our patient's cohort. However, our study investigated more ISGs and found, for instance, *OASL*, *IFI35,* or *MX2* to be expressed stronger in patients with AAV compared to healthy controls (data not shown).

Similar to what Batten et al. suggested in their study of SAVI [240], we propose that DNA sensing via cGAS/STING is not the sole signaling pathway driving pathogenesis, as we observe partial but not complete protection upon interfering with the STING signaling pathway. It may well be that up-taken DNA gets sensed simultaneously by other nucleic acid sensors like AIM2 or TLR9, another double-stranded DNA sensor. TLR9 signaling was found to result in, e.g., IFN-α production upon sensing DNA from herpes simplex virus-2 [241]. However, it is unlikely that TLR9 signaling is involved in ANCA-associated vasculitis because *Unc93B1*-deficient mice, lacking TLR3, 7, and 9, were not protected from disease progression (C. Krollmann and L. L. Teichmann, University Hospital Bonn, pers. comm.). STING signaling was shown to induce TNF-α production, independent of type-I interferon [242]. Our group's preliminary data have also identified that TNF-α promoted disease in our inducible model for autoimmune vasculitis. Therefore, it remains to be investigated whether TNF-α is involved in AAPV disease development together with IFN-I.

4.4. Monocyte-derived macrophages contribute to inflammation, while alveolar macrophages promote resolution

Macrophages are a heterogeneous group of immune cells in many organs that play different homeostatic and inflammatory roles, often performed by different subpopulations [243]. Conversely, macrophages can produce pro-inflammatory molecules like TNF-α, IL-6, NO, and ROS [244]. On the other hand, they actively

inhibit responses to otherwise innocuous stimuli [245] or can even promote resolution of inflammation by releasing anti-inflammatory mediators and clearing cellular debris [246, 247].

In our model of AAPV, we have observed tissue-resident macrophages as well as a macrophage subset infiltrating the lung upon disease induction. Further investigations revealed that infiltrating macrophages were derived from circulating monocytes and were primary producers of pathogenic IFN-β in the lung of mice with AAPV, promoting disease progression. In clear contrast, tissue-resident alveolar macrophages (AMs) in mice undergoing AAPV produced little IFN-β and instead contributed to lung recovery by phagocytosing extravascular red blood cells and dampening inflammation in a STING-independent manner. STING activation in monocyte-derived macrophages, as well as tissue-resident Kupffer cells, was previously found in fibrotic livers of patients with NASH, where STING expression positively correlated with liver inflammation severity [248]. Tissue-resident macrophages are often replaced upon inflammation by infiltrating monocyte-derived macrophages, which are believed to promote inflammation [249-252]. However, few studies compare tissue-resident and monocyte-derived macrophages functionally within the same disease model beyond transcriptomic investigations.

Removal of dead or damaged cells by macrophages is essential to prevent accumulation of inflammatory signals derived from cellular death [253-255]. Clearance of senescent or extravascular red blood cells by tissue-resident macrophages is an important homeostatic process for dampening extracellular heme accumulation as well as an essential mechanism of iron recycling [256]. However, hyper-activation of macrophages and the subsequent excessive uptake of red blood cells may also cause severe anemia, as reported for malaria [257, 258] and hemophagocytic lymphohistiocytosis (HLH) [259]. Therefore, this process requires strict regulation.

Within our study, we observed beneficial clearance of extravascular red blood cells by tissue-resident alveolar macrophages, contributing to recovery from pulmonary hemorrhages. Although neutrophils, monocytes, and monocyte-derived

macrophages are phagocytic cells as well [260, 261], we did not observe any uptake of red blood cells by these populations. A possible explanation of the cell type-specific uptake may be that in comparison to alveolar macrophages, none of these other populations expressed CD206, which was shown to be important for hemophagocytosis in sickle cell anemia and malaria [203]. Additionally, phagocytosis of red blood cells requires the expression of SIRPα [262], which is most abundant in some macrophages, monocytes, and neutrophils [263]. Thus, it would be interesting to investigate SIRPα expression by the different macrophage subsets in our AAPV model. Furthermore, IL-33 is released by damaged erythrocytes, instructing the differentiation of iron-metabolizing macrophages via the IL1RL1 receptor, resulting in subsequent MYD88 activation [264]. Having seen, that *Myd88* expression was strongly decreased in mature Siglec-F^{+} neutrophils in the BAS of mice during recovery from AAPV, it is most likely that this pathway is not activated in neutrophils explaining why they may not have taken up RBCs in the lung.

4.5.Estradiol supplementation ameliorates AAPV progression

Autoimmune diseases occur more frequently in women than men [136]. Although the overall prevalence of vasculitis is equally distributed, 64% of patients with MPO-AAV are women [5]. The sex bias was also reflected in our mouse model, where we observed more severe disease outcomes in female mice. Additionally, disease severity in females was more variable than in male mice, suggesting a dependency of disease pathogenesis on hormonal oscillation rather than genetic differences between females and males. We observed that female mice had more severe hemorrhages at a progestogenic phase at the time of disease induction, where circulating progesterone levels are high and estrogen levels are low. Investigating the role of female sex hormones in the pathogenesis of AAPV revealed that estradiol supplementation can reduce pulmonary hemorrhages and dampen inflammation *in vivo*.

We initially hypothesized that estradiol ameliorates pulmonary hemorrhages by inducing endothelial and/or epithelial cell proliferation, an important estrogen function in the uterus during the menstruation cycle [207, 208]. However, we did not see any significant differences in the proliferation of endothelial or epithelial cells upon hormone supplementation in the lungs of mice with AAPV after three days. The time point of analysis may be critical here. Mice treated with estradiol or the combination with progesterone already displayed reduced pulmonary hemorrhages by day 3, indicating that there have been repairing mechanisms, such as proliferation of endothelial or epithelial cells, taken place earlier. Therefore, it may be interesting to investigate proliferation as early as one day after disease induction.

In steady-state estradiol supplementation, in contrast to progesterone or vehicle control, limited circulating leukocytes, including monocytes, NK cells, and B cells, supporting the anti-inflammatory role of estrogen that has been previously reported [265]. Although circulating neutrophil counts were unaffected by estradiol supplementation at steady-state, they produced less spontaneous ROS compared to vehicle control mice. Thus, three days after AAPV induction, male mice treated with estradiol had significantly decreased neutrophil counts in the BALF. This is in line with findings showing that estradiol can inhibit the NADPH oxidase subunit gp91phox [266] as well as vascular NADPH oxidase activity [209]. It was further demonstrated that NADPHox up-regulates MMP-9 production [35], which in turn mediates neutrophil migration [34]. In line with these observations, we provide evidence that estradiol reduced MMP-3 and -9 in the lungs of mice with AAPV. Estradiol has been previously reported to reduce MMP-9 in an autoimmune demyelinating disease model, leading to decreased infiltration of monocytes and T cells in the CNS [155]. Altogether, these findings suggest that neutrophils are less activated upon estradiol supplementation, leading to decreased NADPHox activity and, consequently, reduced ROS and MMP-9 production. Consequently, this may affect their ability to extravasate in the lung resulting in reduced tissue damage.

Furthermore, we found that estradiol supplementation decreased the number of inflammatory monocyte-derived macrophages in the lung. Previous studies have shown that estradiol inhibits mechanisms of monocyte migration into tissues, where they differentiate into macrophages. For instance, estradiol can inhibit MCP-1 production in coronary artery endothelial cells [267], a molecule required for monocyte migration. Estradiol was also shown to directly inhibit the migration of monocytes exposed to MCP-1 *in vitro* [268] and *in vivo* [269]. The group of Janis et al. elucidated decreased expression of CCR2 in murine monocytes upon estrogen stimulation [270]. Further evidence was provided by Giraud et al., who could show reduced CCL2 expression by astrocytes upon estradiol treatment in a model of experimental allergic encephalomyelitis, resulting in suppressed recruitment of inflammatory myeloid cells [271]. These findings could explain why estradiol-treated mice displayed a weaker disease phenotype, having seen that monocyte-derived macrophages fulfill a pro-inflammatory role by producing IFN-β during AAPV progression.

NADPHox activity was previously shown to decrease NETosis (a form of DNA release) [31]. Having seen nucleic acid sensing dependent AAPV pathogenesis, we investigated NETosis upon hormone supplementation. Interestingly, we observed reduced amounts of extracellular DNA in BALF upon combinatory treatment with estradiol and progesterone but not upon estradiol or progesterone treatment alone. However, the two groups that included estrogen supplementation had ameliorated disease progression. This suggests different mechanisms that improve disease outcomes in estrogen and estrogen+progesterone-treated mice, which remain to be elucidated.

Surprisingly, we have not seen any significant changes upon progesterone supplementation alone. This may be because progesterone responsiveness depends on the presence of estrogen, which is necessary for the expression of the progesterone receptor [272]. Thus, the changes we observe in estradiol+ progesterone-treated mice may be the actual action of progesterone.

A factor that we did not investigate in this project is the role of NO on disease progression. NO regulates several biological processes and is essential for maintaining vascular health and respiratory homeostasis [273, 274]. Estradiol was found to increase the basal release of nitric oxide by endothelial cells, which led to reduced binding of macrophages to the endothelium, an early event in the development of atherosclerosis [275]. Furthermore, estradiol reduced the adhesion of monocytes to the endothelium [276]. Reduced NO production by endothelial cells upon estradiol supplementation may explain the decreased number of infiltrating macrophages we observed during ANCA vasculitis.

Although our findings that constant supplementation with estradiol ameliorates AAPV progression, our experimental design of hormone supplementation has some limitations. The natural oscillation of hormones may have additional effects on the immune system than the sole presence or absence of the single hormone itself. Several studies showed that especially the withdrawal of hormones fulfills important functions. For example, there is evidence that leukocyte infiltration, cytokine release, and up-regulation of MMPs associated with menstruation are due to the withdrawal of progesterone rather than its presence or absence [277, 278]. With this background, it would be highly interesting to supplement mice with hormones and discontinue the treatment to see how the disease progresses after hormonal withdrawal.

5. Conclusions and Outlook

This study has identified key cellular and molecular mechanisms for AAPV progression: (1) nucleic acid sensing via the STING/IRF3/IFN-I axis drives disease pathogenesis; (2) infiltrating monocyte-derived macrophages drive disease progression by producing pathogenic IFN-β, while alveolar macrophages contributed to disease recovery by clearing extravascular RBCs; (3) estradiol supplementation ameliorated disease progression. However, important questions remain to be answered.

1. What are the cellular targets of IFN-β produced by infiltrating macrophages?

Blocking of IFNAR-I or JAK/STAT inhibition with Baricitinib (data not shown) ameliorated AAPV progression, identifying a pathogenic role of IFNAR-I signaling. To elucidate which cell type senses IFN-β in a pathogenic manner, an initial suggestion would be to assess disease severity in bone marrow chimeras to identify whether IFNAR-I expression is necessary on immune or non-immune cells. Identification of specific cell types would require using the Cre/LoxP system in mouse strains. Moreover, it would be interesting to investigate how IFN-β mediates disease progression. A possibility is that endothelial cells recognize IFN-I, which activates a cell death pathway.

2. Which other mechanisms, besides STING/IFN signaling, trigger endothelial cell death?

STING/IFNAR-I axis dampened hemorrhage severity but did not completely prevent them, demonstrating that other mechanisms than nucleic acid sensing via STING/IFN-I contribute to disease progression. Therefore, other nucleic acid sensors, for instance, AIM2, may also play a pathogenic role. Our group's preliminary results have also identified that TNF-α promoted disease in our inducible model for autoimmune vasculitis. Previously, it was shown that STING activation by bacterial second messenger (3'-5')-cyclic-di-guanosine-monophosphate (CDG) led to an IFN-I-independent TNF-α production [242]. Thus, combinatory blockade of IFN-β and TNF-α action may further prevent pulmonary hemorrhages.

3. How does estradiol supplementation ameliorate AAPV progression?

Regarding the hormonal effect on disease progression, an open question remains on how estradiol ameliorates AAPV. As discussed here, suppression of NADPH-oxidase by estradiol may constitute one such mechanism. To test this, estradiol supplementation of gp91phox-deficient mice would be necessary. Moreover, examining the involvement of metalloproteases in disease progression would be interesting, as we have seen a reduction of MMP-3 and -9 as well as reduced neutrophil infiltration upon estradiol treatment.

4. Why do female mice display worse disease severity than males?

The observation that female mice have more severe disease progression than males is apparently contradictory to the improved disease prognosis upon estradiol supplementation. We wonder whether the natural hormonal withdrawal in humans and mice worsens hemorrhages and inflammation in the lung rather than the hormone expression itself. To test this, it would be necessary to mimic hormonal withdrawal and investigate disease progression.

Appendix

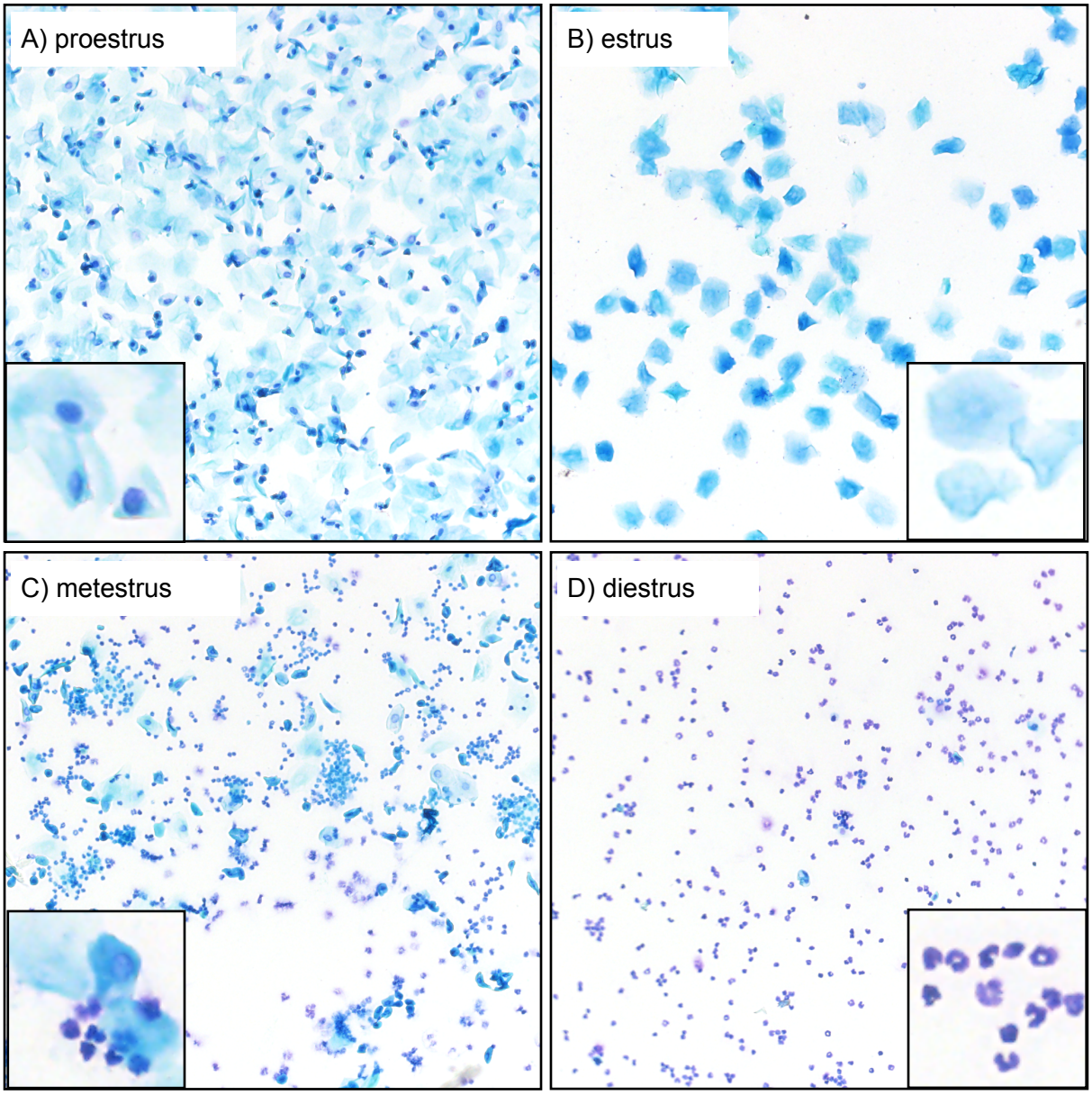

Figure 34: Representative images of vaginal cytology at different estrus-cycle phases. Vaginal lavage was performed, and smears were stained with Giemsa. Images represent estrus-cycle phase: A) proestrus, B) estrus, C) metestrus, and D) diestrus. 10x magnification and zoom-in.

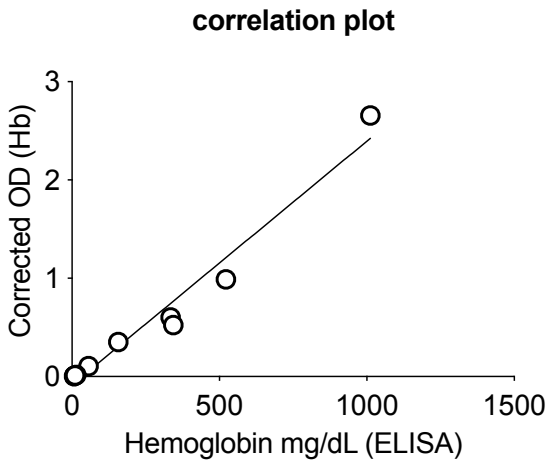

	ELISA (mg/dL) vs. OD [400nm]
Pearson r	
r	0.9828
95% confidence interval	0.9264 to 0.9961
R squared	0.9659
P value	
P (two-tailed)	<0.0001
P value summary	****
Significant? (alpha = 0.05)	Yes
Number of XY Pairs	10

Figure 35: Correlation of optical density of hemoglobin and hemoglobin ELISA. BALF was collected from mice five days after vasculitis induction. Hemoglobin was quantified using an absorbance reader (400 nm - 600 nm reference) and a colorimetric assay (Abcam). Data were correlated using Graphpad Prism Software.

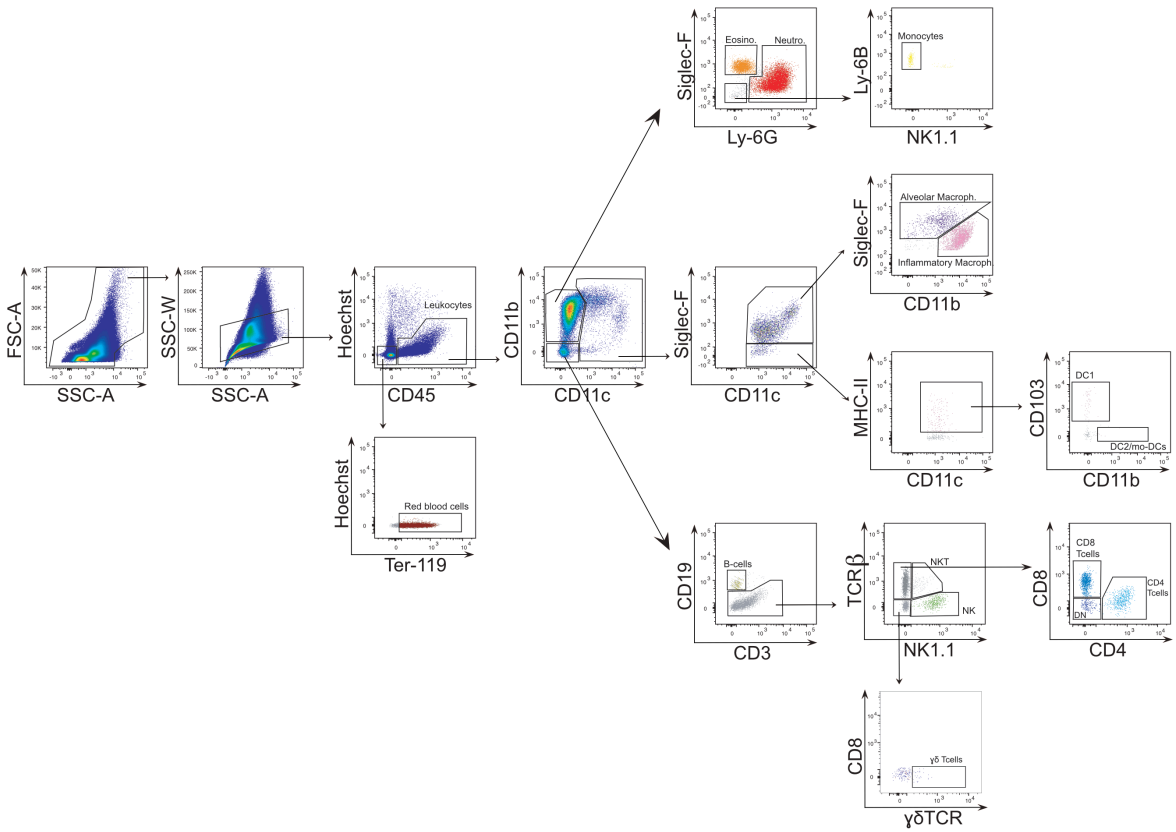

Figure 36: FACS gating strategy of BALF. BALF was collected from mice three days after vasculitis induction. BALF was stained as described in 2.2.17. and analyzed using the LSR Fortessa.

Table 9: Down-regulated genes in Siglec-F+ neutrophils

mRNA	Fold change	p-value	mRNA	Fold change	p-value	mRNA	Fold change	p-value
Camp	0.004	0.00002	Tlr8	0.176	0.00177	Tap1	0.351	0.014
Irf1	0.103	0.00005	Cd36	0.083	0.00196	Il4ra	0.384	0.014
Ifitm1	0.104	0.00006	C1qa	0.157	0.00201	Zbtb7b	0.415	0.0144
Bcl6	0.048	0.00007	Tnfsf14	0.227	0.00203	Cd79b	0.460	0.0158
Fcgr4	0.075	0.00009	Socs3	0.275	0.00241	Ifngr2	0.392	0.0159
Itgal	0.120	0.00010	H2-Eb1	0.168	0.00288	Cxcl12	0.248	0.016
Il15	0.063	0.00013	Cd55	0.321	0.00292	Stat5b	0.344	0.0168
Lilrb3	0.166	0.00027	Cd99	0.316	0.00309	Il23a	0.435	0.0176
H2-Aa	0.095	0.00029	Ly96	0.253	0.00328	Irgm1	0.321	0.0178
Notch2	0.189	0.00030	Ctnnb1	0.398	0.00339	Itga5	0.243	0.018
Litaf	0.173	0.00030	Myd88	0.182	0.00346	Cd53	0.275	0.0196
Irf7	0.134	0.00036	Mbp	0.167	0.00364	Crlf2	0.195	0.0213
Cxcr1	0.104	0.00039	Il13ra1	0.237	0.00376	Nod2	0.325	0.0218
Cxcl15	0.012	0.00048	Cd244	0.219	0.00431	Ltb	0.392	0.0218
Muc1	0.020	0.00052	Irak3	0.356	0.00435	Ciita	0.406	0.0235
Clu	0.030	0.00058	Cd86	0.215	0.00469	Smad3	0.277	0.0237
Bid	0.078	0.00062	Map4k2	0.312	0.00492	Ifi204	0.202	0.0239
Ccl6	0.196	0.00063	Il18	0.245	0.00504	Il10rb	0.490	0.0258
Il18rap	0.218	0.00063	Ifnar1	0.342	0.00507	Npc1	0.538	0.0273
H2-Q10	0.036	0.00070	Tagap	0.252	0.00515	Psmb9	0.233	0.0279
Fas	0.129	0.00074	Stat1	0.314	0.00521	Ets1	0.270	0.028
Entpd1	0.281	0.00081	Ptpn6	0.293	0.00536	Ccr2	0.522	0.0304
Itga4	0.203	0.00084	Cd82	0.346	0.00557	Il6ra	0.480	0.0318
Il1rap	0.144	0.00084	Jak1	0.330	0.00563	Ccl4	0.432	0.0332
Il16	0.192	0.00096	Mapkapk2	0.285	0.00602	Icam1	0.395	0.0339
Il10ra	0.291	0.00096	Hcst	0.262	0.00615	Casp1	0.382	0.0354
Stat6	0.262	0.00097	Tgfbr2	0.297	0.00641	Sell	0.204	0.0356
Stat3	0.248	0.00124	Irak4	0.306	0.00678	Tgfb1	0.486	0.0363
C1qb	0.122	0.00126	Ddx58	0.314	0.00720	Fn1	0.257	0.0366
Lilra6	0.100	0.00131	Spn	0.257	0.00728	Notch1	0.460	0.0369
Cd274	0.213	0.00139	Traf3	0.243	0.00853	Csf1r	0.544	0.0428
Cd74	0.193	0.00146	Card9	0.316	0.00859	Relb	0.304	0.0443
Il33	0.038	0.00147	Fcgr3	0.275	0.00869	Ltf	0.545	0.0455
Cfp	0.154	0.00154	H2-Ab1	0.177	0.00960	Il18r1	0.470	0.046
Bcl3	0.146	0.00158	Stat4	0.369	0.01220	Cd19	0.562	0.0469
Mapk14	0.277	0.00165	H2-DMa	0.339	0.01370			

Table 10: Up-regulated genes in Siglec-F^{+} neutrophils

mRNA	Fold change	p-value
Cdkn1a	13.93	0.004
Ski	8.94	0.014
Il1a	7.31	0.023
Il1rl2	6.82	0.000
Tnf	6.68	0.020
Mif	6.50	0.025
Ccl3	5.82	0.032
Fcgr2b	5.54	0.031
Tnfrsf13b	5.06	0.003
Ahr	4.79	0.001
Cish	4.56	0.039
Ikbke	4.29	0.009
Cd48	3.76	0.011
Trp53	2.99	0.026
Ccl9	2.71	0.002
Psmb10	2.27	0.026

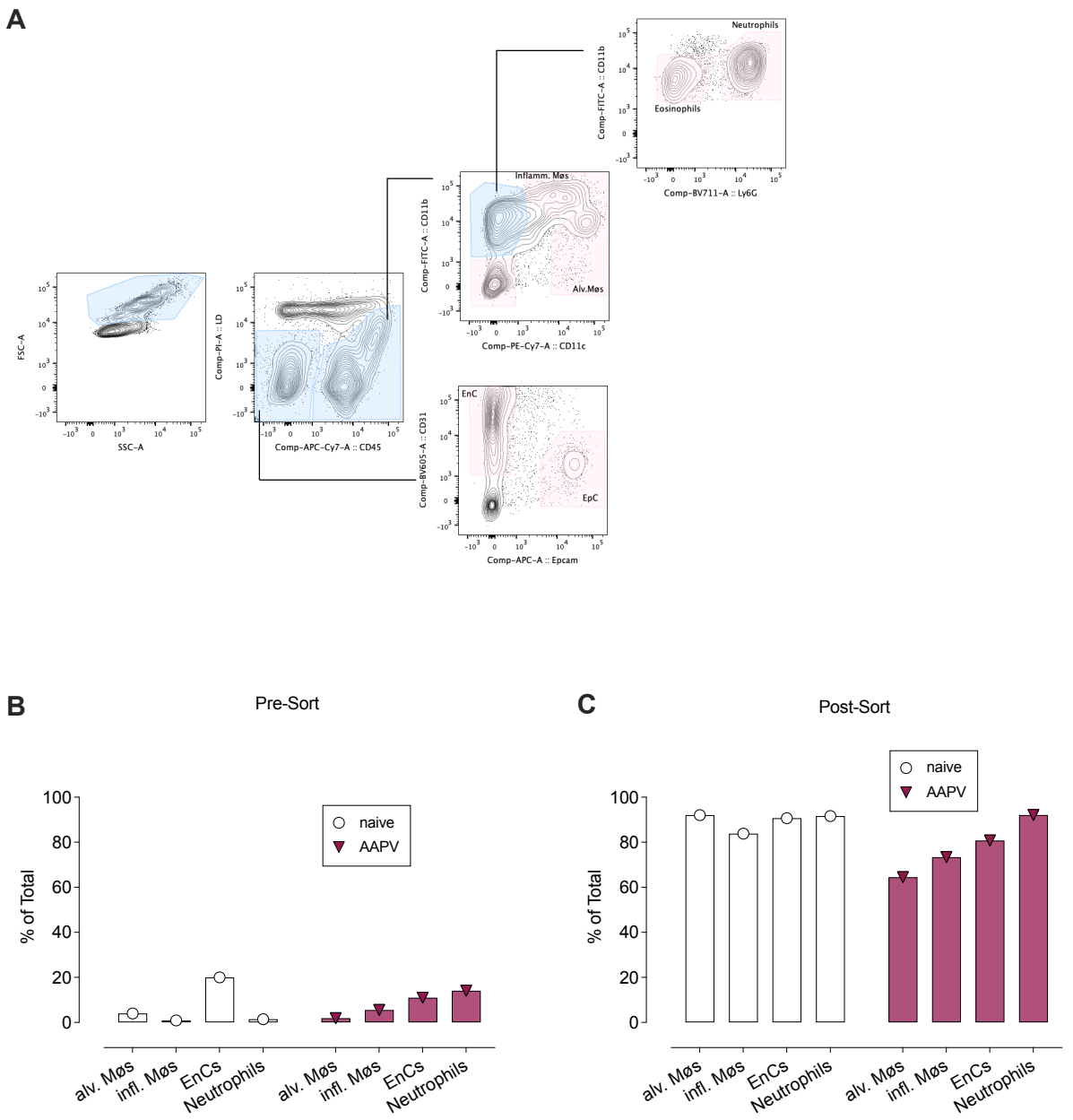

Figure 37: FACS gating strategy and purity of macrophage sort. Lungs were collected from IFN-reporter mice three days after vasculitis induction. (**A**) Gating strategy indicated in mice with AAPV. (**B**) Purity of indicated cell population before sorting of naive and mice with AAPV. (**C**) Purity of indicated cell population after sorting of naive and mice with AAPV.

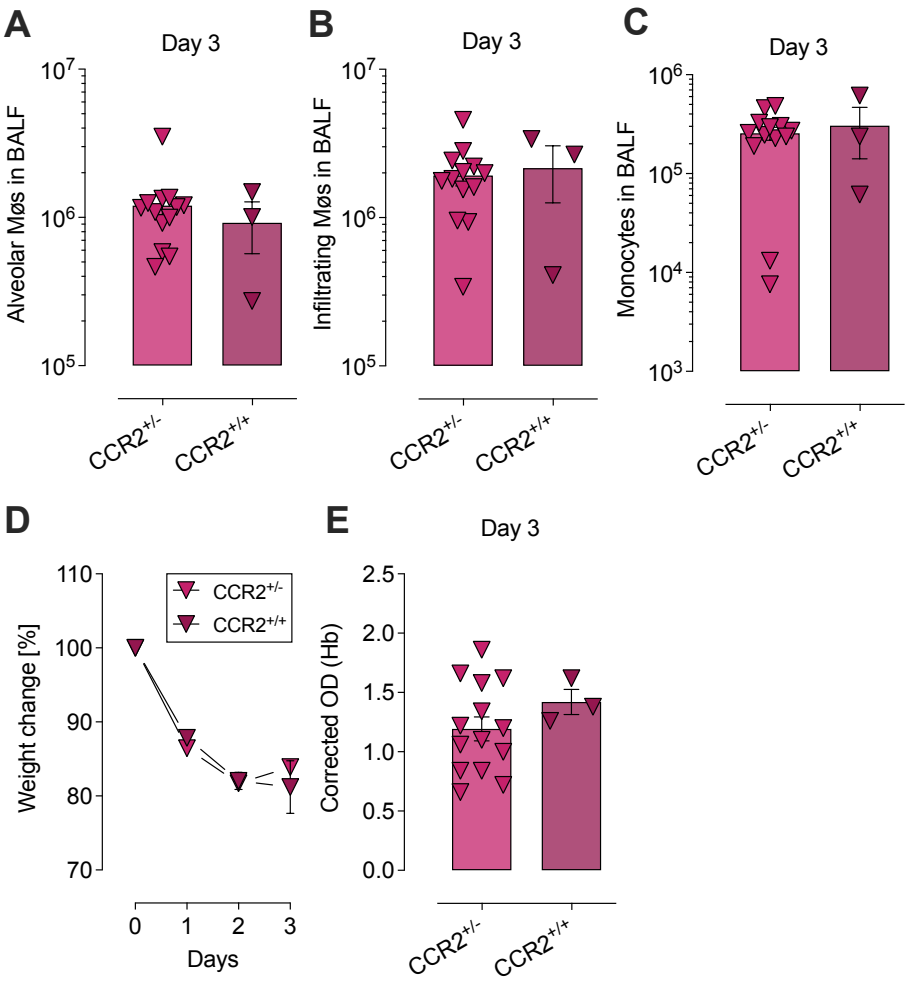

Figure 38: Comparison of homozygous and heterozygous CCR2 wild-type mice. AAPV was induced in CCR2$^{+/+}$ and CCR2$^{+/-}$ mice. After three days, mice were painlessly sacrificed, and BALF was taken. Hemorrhages and immune cell infiltration were quantified. (**A-C**) FACS quantification of alveolar macrophages (A), infiltrating macrophages (B), and monocytes (C) in BALF of the indicated groups. (**D**) Weight changes over time in the indicated groups. (**E**) Hemorrhages in BALF. The data is shown from one experiment. Mean ± SEM; each symbol represents one mouse. Unpaired students *t*-test.

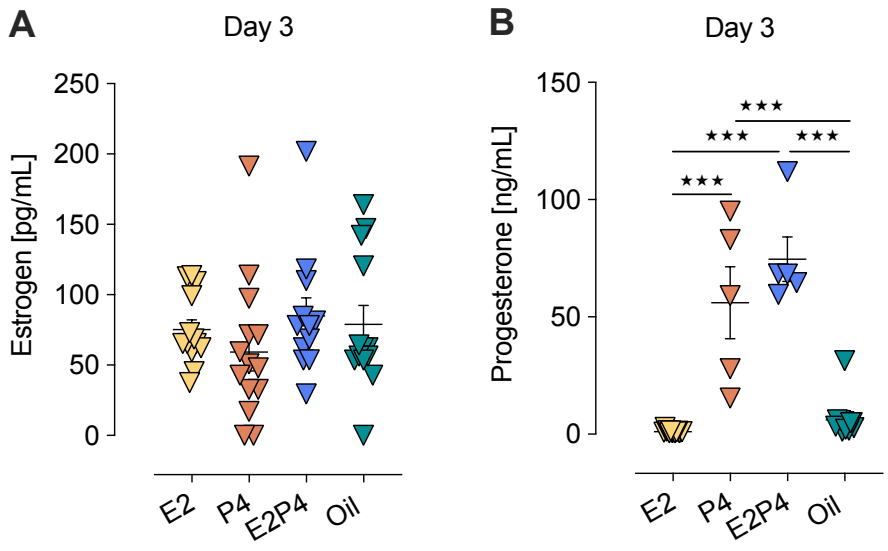

Figure 39: Hormone quantification in plasma of male mice. Blood was taken on d3 of male mice, which were supplemented with hormones starting at d-4. (**A**) Estrogen levels in plasma on d3. (**B**) Progesterone levels in plasma on d3. The data shown are pooled from two independent experiments. Mean ± SEM; each symbol represents one mouse. One-way ANOVA *p<0.05; **p<0.01.

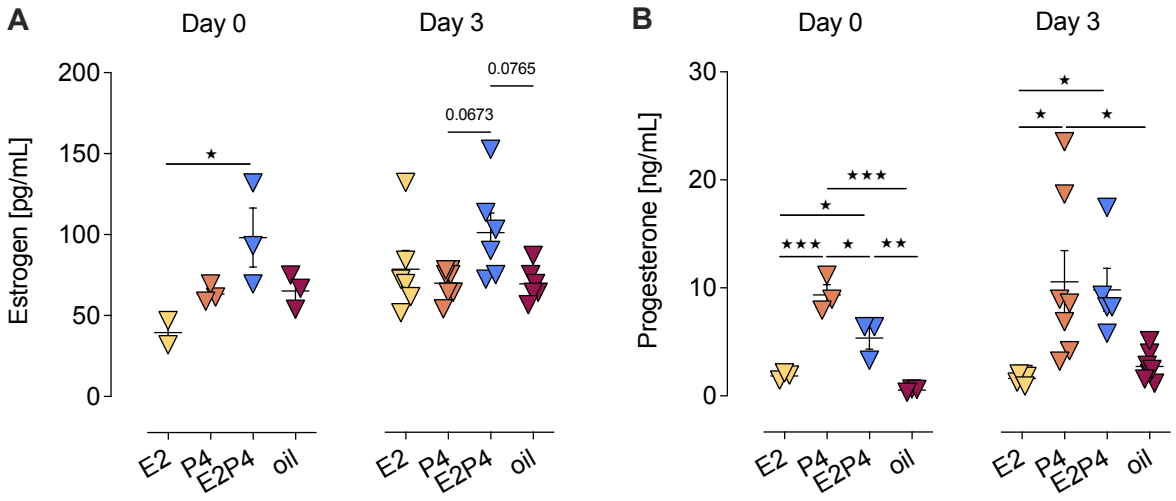

Figure 40: Hormone quantification in plasma of ovariectomized mice. Blood was taken on d0 and d3 of ovariectomized mice supplemented with hormones starting at d-4. (**A**) Estrogen levels in plasma on d0 and three days after AAPV induction. (**B**) Progesterone levels in plasma on d0 and three days after AAPV induction. The data is shown from one experiment. Mean ± SEM; each symbol represents one mouse. One-way ANOVA *p<0.05; **p<0.01 ***p<0.001.

Bibliography

1. Gross, W.L., A. Trabandt, and E. Reinhold-Keller, *Diagnosis and evaluation of vasculitis.* Rheumatology (Oxford), 2000. **39**(3): p. 245-52.

2. Suresh, E., Diagnostic approach to patients with suspected vasculitis. Postgrad Med J, 2006. **82**(970): p. 483-8.

3. Jennette, J.C., Overview of the 2012 revised International Chapel Hill Consensus Conference nomenclature of vasculitides. Clin Exp Nephrol, 2013. **17**(5): p. 603-606.

4. Watts, R.A., et al., Classification, epidemiology and clinical subgrouping of antineutrophil cytoplasmic antibody (ANCA)-associated vasculitis. Nephrol Dial Transplant, 2015. **30 Suppl 1**: p. i14-22.

5. Unizony, S., et al., Clinical outcomes of treatment of anti-neutrophil cytoplasmic antibody (ANCA)-associated vasculitis based on ANCA type. Ann Rheum Dis, 2016. **75**(6): p. 1166-9.

6. Mohammad, A.J., An update on the epidemiology of ANCA-associated vasculitis. Rheumatology (Oxford), 2020. **59**(Suppl 3): p. iii42-iii50.

7. Lin, Y., et al., Antineutrophil cytoplasmic antibody-associated vasculitis complicated with diffuse alveolar hemorrhage: a study of 12 cases. J Clin Rheumatol, 2009. **15**(7): p. 341-4.

8. Xiao, H., et al., Overview of the Pathogenesis of ANCA-Associated Vasculitis. Kidney Dis (Basel), 2016. **1**(4): p. 205-15.

9. Kamesh, L., L. Harper, and C.O. Savage, *ANCA-positive vasculitis.* J Am Soc Nephrol, 2002. **13**(7): p. 1953-60.

10. Kallenberg, C.G., Pathogenesis of ANCA-associated vasculitides. Ann Rheum Dis, 2011. **70 Suppl 1**: p. i59-63.

11. Yates, M. and R. Watts, *ANCA-associated vasculitis.* Clin Med (Lond), 2017. **17**(1): p. 60-64.

12. Cui, Z., et al., Natural autoantibodies to myeloperoxidase, proteinase 3, and the glomerular basement membrane are present in normal individuals. Kidney Int, 2010. **78**(6): p. 590-7.

13. Falk, R.J., et al., Anti-neutrophil cytoplasmic autoantibodies induce neutrophils to degranulate and produce oxygen radicals in vitro. Proc Natl Acad Sci U S A, 1990. **87**(11): p. 4115-9.

14. Reumaux, D., et al., Expression of myeloperoxidase (MPO) by neutrophils is necessary for their activation by anti-neutrophil cytoplasm autoantibodies (ANCA) against MPO. J Leukoc Biol, 2003. **73**(6): p. 841-9.

15. Apel, F., et al., The cytosolic DNA sensor cGAS recognizes neutrophil extracellular traps. Sci Signal, 2021. **14**(673).

16. Falk, R.J. and J.C. Jennette, ANCA are pathogenic--oh yes they are! J Am Soc Nephrol, 2002. **13**(7): p. 1977-1979.

17. Haas, M. and J.A. Eustace, Immune complex deposits in ANCA-associated crescentic glomerulonephritis: a study of 126 cases. Kidney Int, 2004. **65**(6): p. 2145-52.

18. Lin, W., et al., Glomerular Immune Deposition in MPO-ANCA Associated Glomerulonephritis Is Associated With Poor Renal Survival. Front Immunol, 2021. **12**: p. 625672.

19. Groger, M., et al., Immune complexes from vasculitis patients bind to endothelial Fc receptors independent of the allelic polymorphism of FcgammaRIIa. J Invest Dermatol, 1999. **113**(1): p. 56-60.

20. Jennette, J.C., et al., Pathogenesis of antineutrophil cytoplasmic autoantibody-associated small-vessel vasculitis. Annu Rev Pathol, 2013. **8**: p. 139-60.

21. Kinkade, J.M., Jr., et al., Differential distribution of distinct forms of myeloperoxidase in different azurophilic granule subpopulations from human neutrophils. Biochem Biophys Res Commun, 1983. **114**(1): p. 296-303.

22. Witko-Sarsat, V., et al., Presence of proteinase 3 in secretory vesicles: evidence of a novel, highly mobilizable intracellular pool distinct from azurophil granules. Blood, 1999. **94**(7): p. 2487-96.

23. Xiao, H., et al., The role of neutrophils in the induction of glomerulonephritis by anti-myeloperoxidase antibodies. Am J Pathol, 2005. **167**(1): p. 39-45.

24. Kessenbrock, K., et al., Netting neutrophils in autoimmune small-vessel vasculitis. Nat Med, 2009. **15**(6): p. 623-5.

25. Sangaletti, S., et al., Neutrophil extracellular traps mediate transfer of cytoplasmic neutrophil antigens to myeloid dendritic cells toward ANCA induction and associated autoimmunity. Blood, 2012. **120**(15): p. 3007-18.

26. Surmiak, M.P., et al., Circulating mitochondrial DNA in serum of patients with granulomatosis with polyangiitis. Clin Exp Immunol, 2015. **181**(1): p. 150-5.

27. Urban, C.F., et al., Neutrophil extracellular traps contain calprotectin, a cytosolic protein complex involved in host defense against Candida albicans. PLoS Pathog, 2009. **5**(10): p. e1000639.

28. Garcia-Romo, G.S., et al., Netting neutrophils are major inducers of type I IFN production in pediatric systemic lupus erythematosus. Sci Transl Med, 2011. **3**(73): p. 73ra20.

29. Soderberg, D. and M. Segelmark, Neutrophil Extracellular Traps in ANCA-Associated Vasculitis. Front Immunol, 2016. **7**: p. 256.

30. Brinkmann, V., et al., Neutrophil extracellular traps kill bacteria. Science, 2004. **303**(5663): p. 1532-5.

31. Fuchs, T.A., et al., Novel cell death program leads to neutrophil extracellular traps. J Cell Biol, 2007. **176**(2): p. 231-41.

32. Monach, P.A., et al., Serum proteins reflecting inflammation, injury and repair as biomarkers of disease activity in ANCA-associated vasculitis. Ann Rheum Dis, 2013. **72**(8): p. 1342-50.

33. Ishizaki, J., et al., Targeted proteomics reveals promising biomarkers of disease activity and organ involvement in antineutrophil cytoplasmic antibody-associated vasculitis. Arthritis Res Ther, 2017. **19**(1): p. 218.

34. Bradley, L.M., et al., Matrix metalloprotease 9 mediates neutrophil migration into the airways in response to influenza virus-induced toll-like receptor signaling. PLoS Pathog, 2012. **8**(4): p. e1002641.

35. Hsieh, H.L., et al., NADPH oxidase-mediated redox signal contributes to lipoteichoic acid-induced MMP-9 upregulation in brain astrocytes. J Neuroinflammation, 2012. **9**: p. 110.

36. Zalba, G., et al., Phagocytic NADPH oxidase-dependent superoxide production stimulates matrix metalloproteinase-9: implications for human atherosclerosis. Arterioscler Thromb Vasc Biol, 2007. **27**(3): p. 587-93.

37. Charles, L.A., R.J. Falk, and J.C. Jennette, Reactivity of antineutrophil cytoplasmic autoantibodies with mononuclear phagocytes. J Leukoc Biol, 1992. **51**(1): p. 65-8.

38. O'Brien, E.C., et al., Intermediate monocytes in ANCA vasculitis: increased surface expression of ANCA autoantigens and IL-1beta secretion in response to anti-MPO antibodies. Sci Rep, 2015. **5**: p. 11888.

39. Weidner, S., et al., Antineutrophil cytoplasmic antibodies induce human monocytes to produce oxygen radicals in vitro. Arthritis Rheum, 2001. **44**(7): p. 1698-706.

40. Nowack, R., et al., Upregulation of CD14 and CD18 on monocytes In vitro by antineutrophil cytoplasmic autoantibodies. J Am Soc Nephrol, 2000. **11**(9): p. 1639-1646.

41. Heumann, D., et al., Control of lipopolysaccharide (LPS) binding and LPS-induced tumor necrosis factor secretion in human peripheral blood monocytes. J Immunol, 1992. **148**(11): p. 3505-12.

42. Booth, A., et al., Prospective study of TNFalpha blockade with infliximab in anti-neutrophil cytoplasmic antibody-associated systemic vasculitis. J Am Soc Nephrol, 2004. **15**(3): p. 717-21.

43. Tobler, A., et al., Regulation of gene expression of myeloperoxidase during myeloid differentiation. J Cell Physiol, 1988. **136**(2): p. 215-25.

44. Fazekas, B., et al., Alterations in circulating lymphoid cell populations in systemic small vessel vasculitis are non-specific manifestations of renal injury. Clin Exp Immunol, 2018. **191**(2): p. 180-188.

45. Schreiber, A., et al., Bone marrow-derived cells are sufficient and necessary targets to mediate glomerulonephritis and vasculitis induced by anti-myeloperoxidase antibodies. J Am Soc Nephrol, 2006. **17**(12): p. 3355-64.

46. Rastaldi, M.P., et al., Glomerular monocyte-macrophage features in ANCA-positive renal vasculitis and cryoglobulinemic nephritis. J Am Soc Nephrol, 2000. **11**(11): p. 2036-2043.

47. Zhao, L., et al., M2 macrophage infiltrates in the early stages of ANCA-associated pauci-immune necrotizing GN. Clin J Am Soc Nephrol, 2015. **10**(1): p. 54-62.

48. Harper, L., et al., Neutrophil priming and apoptosis in anti-neutrophil cytoplasmic autoantibody-associated vasculitis. Kidney Int, 2001. **59**(5): p. 1729-38.
49. Popat, R.J., et al., Anti-myeloperoxidase antibodies attenuate the monocyte response to LPS and shape macrophage development. JCI Insight, 2017. **2**(2): p. e87379.
50. Mantovani, A., et al., Macrophage polarization: tumor-associated macrophages as a paradigm for polarized M2 mononuclear phagocytes. Trends Immunol, 2002. **23**(11): p. 549-55.
51. Moran, S.M., et al., Urinary soluble CD163 and monocyte chemoattractant protein-1 in the identification of subtle renal flare in anti-neutrophil cytoplasmic antibody-associated vasculitis. Nephrol Dial Transplant, 2020. **35**(2): p. 283-291.
52. Jennette, J.C. and R.J. Falk, B cell-mediated pathogenesis of ANCA-mediated vasculitis. Semin Immunopathol, 2014. **36**(3): p. 327-38.
53. Fillatreau, S., Cytokine-producing B cells as regulators of pathogenic and protective immune responses. Ann Rheum Dis, 2013. **72 Suppl 2**: p. ii80-4.
54. Morgan, M.D., et al., Patients with Wegener's granulomatosis demonstrate a relative deficiency and functional impairment of T-regulatory cells. Immunology, 2010. **130**(1): p. 64-73.
55. Free, M.E., et al., Patients with antineutrophil cytoplasmic antibody-associated vasculitis have defective Treg cell function exacerbated by the presence of a suppression-resistant effector cell population. Arthritis Rheum, 2013. **65**(7): p. 1922-33.
56. Marinaki, S., et al., Abnormalities of CD4 T cell subpopulations in ANCA-associated vasculitis. Clin Exp Immunol, 2005. **140**(1): p. 181-91.
57. Marinaki, S., et al., Persistent T-cell activation and clinical correlations in patients with ANCA-associated systemic vasculitis. Nephrol Dial Transplant, 2006. **21**(7): p. 1825-32.
58. Sanders, J.S., et al., Plasma levels of soluble interleukin 2 receptor, soluble CD30, interleukin 10 and B cell activator of the tumour necrosis factor family during follow-up in vasculitis associated with proteinase 3-antineutrophil cytoplasmic antibodies: associations with disease activity and relapse. Ann Rheum Dis, 2006. **65**(11): p. 1484-9.

59. Ruth, A.J., et al., Anti-neutrophil cytoplasmic antibodies and effector CD4+ cells play nonredundant roles in anti-myeloperoxidase crescentic glomerulonephritis. J Am Soc Nephrol, 2006. **17**(7): p. 1940-9.

60. Walsh, M., A. Chaudhry, and D. Jayne, Long-term follow-up of relapsing/refractory anti-neutrophil cytoplasm antibody associated vasculitis treated with the lymphocyte depleting antibody alemtuzumab (CAMPATH-1H). Ann Rheum Dis, 2008. **67**(9): p. 1322-7.

61. Rastaldi, M.P., et al., Intraglomerular and interstitial leukocyte infiltration, adhesion molecules, and interleukin-1 alpha expression in 15 cases of antineutrophil cytoplasmic autoantibody-associated renal vasculitis. Am J Kidney Dis, 1996. **27**(1): p. 48-57.

62. Pall, A.A., et al., Glomerular vascular cell adhesion molecule-1 expression in renal vasculitis. J Clin Pathol, 1996. **49**(3): p. 238-42.

63. Chong, D.L.W., et al., ICAM-1 and ICAM-2 Are Differentially Expressed and Up-Regulated on Inflamed Pulmonary Epithelium, but Neither ICAM-2 nor LFA-1: ICAM-1 Are Required for Neutrophil Migration Into the Airways In Vivo. Front Immunol, 2021. **12**: p. 691957.

64. Radford, D.J., C.O. Savage, and G.B. Nash, Treatment of rolling neutrophils with antineutrophil cytoplasmic antibodies causes conversion to firm integrin-mediated adhesion. Arthritis Rheum, 2000. **43**(6): p. 1337-45.

65. DiStasi, M.R. and K. Ley, Opening the flood-gates: how neutrophil-endothelial interactions regulate permeability. Trends Immunol, 2009. **30**(11): p. 547-56.

66. Gupta, A.K., et al., Activated endothelial cells induce neutrophil extracellular traps and are susceptible to NETosis-mediated cell death. FEBS Lett, 2010. **584**(14): p. 3193-7.

67. Narasaraju, T., et al., Excessive neutrophils and neutrophil extracellular traps contribute to acute lung injury of influenza pneumonitis. Am J Pathol, 2011. **179**(1): p. 199-210.

68. Schreiber, A., et al., Necroptosis controls NET generation and mediates complement activation, endothelial damage, and autoimmune vasculitis. Proc Natl Acad Sci U S A, 2017. **114**(45): p. E9618-E9625.

69. Saffarzadeh, M., et al., Neutrophil extracellular traps directly induce epithelial and endothelial cell death: a predominant role of histones. PLoS One, 2012. **7**(2): p. e32366.

70. Novack, S.N. and C.M. Pearson, Cyclophosphamide therapy in Wegener's granulomatosis. N Engl J Med, 1971. **284**(17): p. 938-42.

71. Ramamoorthy, S. and J.A. Cidlowski, Corticosteroids: Mechanisms of Action in Health and Disease. Rheum Dis Clin North Am, 2016. **42**(1): p. 15-31, vii.

72. Jennette, J.C. and P.H. Nachman, ANCA Glomerulonephritis and Vasculitis. Clin J Am Soc Nephrol, 2017. **12**(10): p. 1680-1691.

73. Shand, F.L., The immunopharmacology of cyclophosphamide. Int J Immunopharmacol, 1979. **1**(3): p. 165-71.

74. Hoffman, G.S., et al., Wegener granulomatosis: an analysis of 158 patients. Ann Intern Med, 1992. **116**(6): p. 488-98.

75. Stone, J.H., et al., Rituximab versus cyclophosphamide for ANCA-associated vasculitis. N Engl J Med, 2010. **363**(3): p. 221-32.

76. Flossmann, O., et al., Long-term patient survival in ANCA-associated vasculitis. Ann Rheum Dis, 2011. **70**(3): p. 488-94.

77. Cohen, S.B., et al., Rituximab for rheumatoid arthritis refractory to anti-tumor necrosis factor therapy: Results of a multicenter, randomized, double-blind, placebo-controlled, phase III trial evaluating primary efficacy and safety at twenty-four weeks. Arthritis Rheum, 2006. **54**(9): p. 2793-806.

78. Jones, R.B., et al., Rituximab versus cyclophosphamide in ANCA-associated renal vasculitis: 2-year results of a randomised trial. Ann Rheum Dis, 2015. **74**(6): p. 1178-82.

79. Jayne, D.R.W., et al., Randomized Trial of C5a Receptor Inhibitor Avacopan in ANCA-Associated Vasculitis. J Am Soc Nephrol, 2017. **28**(9): p. 2756-2767.

80. Gross, W.L., et al., Anticytoplasmic antibodies in Wegener's granulomatosis. Lancet, 1986. **1**(8484): p. 806.

81. Xiao, H., et al., Antineutrophil cytoplasmic autoantibodies specific for myeloperoxidase cause glomerulonephritis and vasculitis in mice. J Clin Invest, 2002. **110**(7): p. 955-63.

82. Huugen, D., et al., Aggravation of anti-myeloperoxidase antibody-induced glomerulonephritis by bacterial lipopolysaccharide: role of tumor necrosis factor-alpha. Am J Pathol, 2005. **167**(1): p. 47-58.

83. Faycal, C.A., et al., An adapted passive model of anti-MPO dependent crescentic glomerulonephritis reveals matrix dysregulation and is amenable to modulation by CXCR4 inhibition. Matrix Biol, 2022. **106**: p. 12-33.

84. Anderson, G., et al., Wegener's granuloma. A series of 265 British cases seen between 1975 and 1985. A report by a sub-committee of the British Thoracic Society Research Committee. Q J Med, 1992. **83**(302): p. 427-38.

85. Jennette, J.C. and R.J. Falk, *Small-vessel vasculitis.* N Engl J Med, 1997. **337**(21): p. 1512-23.

86. Janeway, C.A., Jr., Approaching the asymptote? Evolution and revolution in immunology. Cold Spring Harb Symp Quant Biol, 1989. **54 Pt 1**: p. 1-13.

87. Isaacs, A., R.A. Cox, and Z. Rotem, Foreign nucleic acids as the stimulus to make interferon. Lancet, 1963. **2**(7299): p. 113-6.

88. Schlee, M. and G. Hartmann, Discriminating self from non-self in nucleic acid sensing. Nat Rev Immunol, 2016. **16**(9): p. 566-80.

89. Junt, T. and W. Barchet, Translating nucleic acid-sensing pathways into therapies. Nat Rev Immunol, 2015. **15**(9): p. 529-44.

90. Patrushev, M., et al., Mitochondrial permeability transition triggers the release of mtDNA fragments. Cell Mol Life Sci, 2004. **61**(24): p. 3100-3.

91. Lan, Y.Y., et al., Extranuclear DNA accumulates in aged cells and contributes to senescence and inflammation. Aging Cell, 2019. **18**(2): p. e12901.

92. Tan, E.M., et al., Deoxybonucleic acid (DNA) and antibodies to DNA in the serum of patients with systemic lupus erythematosus. J Clin Invest, 1966. **45**(11): p. 1732-40.

93. Stroun, M., et al., Isolation and characterization of DNA from the plasma of cancer patients. Eur J Cancer Clin Oncol, 1987. **23**(6): p. 707-12.

94. Christensen, S.R., et al., Toll-like receptor 7 and TLR9 dictate autoantibody specificity and have opposing inflammatory and regulatory roles in a murine model of lupus. Immunity, 2006. **25**(3): p. 417-28.

95. Stetson, D.B., et al., Trex1 prevents cell-intrinsic initiation of autoimmunity. Cell, 2008. **134**(4): p. 587-98.

96. Liu, Y., et al., Activated STING in a vascular and pulmonary syndrome. N Engl J Med, 2014. **371**(6): p. 507-518.

97. Decout, A., et al., The cGAS-STING pathway as a therapeutic target in inflammatory diseases. Nat Rev Immunol, 2021. **21**(9): p. 548-569.

98. Gautier, G., et al., A type I interferon autocrine-paracrine loop is involved in Toll-like receptor-induced interleukin-12p70 secretion by dendritic cells. J Exp Med, 2005. **201**(9): p. 1435-46.

99. Novick, D., B. Cohen, and M. Rubinstein, The human interferon alpha/beta receptor: characterization and molecular cloning. Cell, 1994. **77**(3): p. 391-400.

100. Uze, G., G. Lutfalla, and I. Gresser, Genetic transfer of a functional human interferon alpha receptor into mouse cells: cloning and expression of its cDNA. Cell, 1990. **60**(2): p. 225-34.

101. Darnell, J.E., Jr., I.M. Kerr, and G.R. Stark, Jak-STAT pathways and transcriptional activation in response to IFNs and other extracellular signaling proteins. Science, 1994. **264**(5164): p. 1415-21.

102. Platanias, L.C., Mechanisms of type-I- and type-II-interferon-mediated signalling. Nat Rev Immunol, 2005. **5**(5): p. 375-86.

103. Der, S.D., et al., Identification of genes differentially regulated by interferon alpha, beta, or gamma using oligonucleotide arrays. Proc Natl Acad Sci U S A, 1998. **95**(26): p. 15623-8.

104. Ablasser, A., et al., Cell intrinsic immunity spreads to bystander cells via the intercellular transfer of cGAMP. Nature, 2013. **503**(7477): p. 530-4.

105. Kranzusch, P.J., cGAS and CD-NTase enzymes: structure, mechanism, and evolution. Curr Opin Struct Biol, 2019. **59**: p. 178-187.

106. Ishikawa, H., Z. Ma, and G.N. Barber, STING regulates intracellular DNA-mediated, type I interferon-dependent innate immunity. Nature, 2009. **461**(7265): p. 788-92.

107. Ma, Z., et al., Modulation of the cGAS-STING DNA sensing pathway by gammaherpesviruses. Proc Natl Acad Sci U S A, 2015. **112**(31): p. E4306-15.

108. Wang, J., et al., Pulmonary surfactant-biomimetic nanoparticles potentiate heterosubtypic influenza immunity. Science, 2020. **367**(6480).

109. Harding, S.M., et al., Mitotic progression following DNA damage enables pattern recognition within micronuclei. Nature, 2017. **548**(7668): p. 466-470.

110. Kitajima, S., et al., Suppression of STING Associated with LKB1 Loss in KRAS-Driven Lung Cancer. Cancer Discov, 2019. **9**(1): p. 34-45.

111. Nakamura, T., et al., Liposomes loaded with a STING pathway ligand, cyclic di-GMP, enhance cancer immunotherapy against metastatic melanoma. J Control Release, 2015. **216**: p. 149-57.

112. van Furth, R., et al., The mononuclear phagocyte system: a new classification of macrophages, monocytes, and their precursor cells. Bull World Health Organ, 1972. **46**(6): p. 845-52.

113. Hulsmans, M., et al., Macrophages Facilitate Electrical Conduction in the Heart. Cell, 2017. **169**(3): p. 510-522 e20.

114. Nicolas-Avila, J.A., et al., A Network of Macrophages Supports Mitochondrial Homeostasis in the Heart. Cell, 2020. **183**(1): p. 94-109 e23.

115. Wynn, T.A. and K.M. Vannella, Macrophages in Tissue Repair, Regeneration, and Fibrosis. Immunity, 2016. **44**(3): p. 450-462.

116. Godwin, J.W., A.R. Pinto, and N.A. Rosenthal, Macrophages are required for adult salamander limb regeneration. Proc Natl Acad Sci U S A, 2013. **110**(23): p. 9415-20.

117. Lavine, K.J., et al., Distinct macrophage lineages contribute to disparate patterns of cardiac recovery and remodeling in the neonatal and adult heart. Proc Natl Acad Sci U S A, 2014. **111**(45): p. 16029-34.

118. Lang, R.A. and J.M. Bishop, Macrophages are required for cell death and tissue remodeling in the developing mouse eye. Cell, 1993. **74**(3): p. 453-62.

119. Stevens, B., et al., The classical complement cascade mediates CNS synapse elimination. Cell, 2007. **131**(6): p. 1164-78.

120. Gosselin, D., et al., Environment drives selection and function of enhancers controlling tissue-specific macrophage identities. Cell, 2014. **159**(6): p. 1327-40.

121. Serbina, N.V. and E.G. Pamer, Monocyte emigration from bone marrow during bacterial infection requires signals mediated by chemokine receptor CCR2. Nat Immunol, 2006. **7**(3): p. 311-7.

122. Mossadegh-Keller, N., et al., Developmental origin and maintenance of distinct testicular macrophage populations. J Exp Med, 2017. **214**(10): p. 2829-2841.

123. Heidt, T., et al., Differential contribution of monocytes to heart macrophages in steady-state and after myocardial infarction. Circ Res, 2014. **115**(2): p. 284-95.

124. van de Laar, L., et al., Yolk Sac Macrophages, Fetal Liver, and Adult Monocytes Can Colonize an Empty Niche and Develop into Functional Tissue-Resident Macrophages. Immunity, 2016. **44**(4): p. 755-68.

125. Vainchtein, I.D., et al., In acute experimental autoimmune encephalomyelitis, infiltrating macrophages are immune activated, whereas microglia remain immune suppressed. Glia, 2014. **62**(10): p. 1724-35.

126. Yamasaki, R., et al., Differential roles of microglia and monocytes in the inflamed central nervous system. J Exp Med, 2014. **211**(8): p. 1533-49.

127. Huitinga, I., et al., Suppression of experimental allergic encephalomyelitis in Lewis rats after elimination of macrophages. J Exp Med, 1990. **172**(4): p. 1025-33.

128. Heppner, F.L., et al., Experimental autoimmune encephalomyelitis repressed by microglial paralysis. Nat Med, 2005. **11**(2): p. 146-52.

129. Van Weyenbergh, J., et al., Treatment of multiple sclerosis patients with interferon-beta primes monocyte-derived macrophages for apoptotic cell death. J Leukoc Biol, 2001. **70**(5): p. 745-8.

130. Jiang, H.R., et al., IL-33 attenuates EAE by suppressing IL-17 and IFN-gamma production and inducing alternatively activated macrophages. Eur J Immunol, 2012. **42**(7): p. 1804-14.

131. Mulherin, D., O. Fitzgerald, and B. Bresnihan, Synovial tissue macrophage populations and articular damage in rheumatoid arthritis. Arthritis Rheum, 1996. **39**(1): p. 115-24.

132. Van Lent, P.L., et al., Local removal of phagocytic synovial lining cells by clodronate-liposomes decreases cartilage destruction during collagen type II arthritis. Ann Rheum Dis, 1998. **57**(7): p. 408-13.

133. Park, S.Y., et al., SIRT1 inhibits differentiation of monocytes to macrophages: amelioration of synovial inflammation in rheumatoid arthritis. J Mol Med (Berl), 2016. **94**(8): p. 921-31.

134. van Schouwenburg, P.A., T. Rispens, and G.J. Wolbink, Immunogenicity of anti-TNF biologic therapies for rheumatoid arthritis. Nat Rev Rheumatol, 2013. **9**(3): p. 164-72.

135. Berlin, I.L. *Was sind Autoimmunerkrankungen?* 2020 [cited 2020; Available from: https://www.imd-berlin.de/spezielle-kompetenzen/autoimmunerkrankungen.html.

136. Desai, M.K. and R.D. Brinton, Autoimmune Disease in Women: Endocrine Transition and Risk Across the Lifespan. Front Endocrinol (Lausanne), 2019. **10**: p. 265.

137. Smith-Bouvier, D.L., et al., A role for sex chromosome complement in the female bias in autoimmune disease. J Exp Med, 2008. **205**(5): p. 1099-108.

138. Sasidhar, M.V., et al., The XX sex chromosome complement in mice is associated with increased spontaneous lupus compared with XY. Ann Rheum Dis, 2012. **71**(8): p. 1418-22.

139. Souyris, M., et al., TLR7 escapes X chromosome inactivation in immune cells. Sci Immunol, 2018. **3**(19).

140. Hall, G.M., et al., A randomised controlled trial of the effect of hormone replacement therapy on disease activity in postmenopausal rheumatoid arthritis. Ann Rheum Dis, 1994. **53**(2): p. 112-6.

141. Bebo, B.F., Jr., et al., Low-dose estrogen therapy ameliorates experimental autoimmune encephalomyelitis in two different inbred mouse strains. J Immunol, 2001. **166**(3): p. 2080-9.

142. Ober, C., D.A. Loisel, and Y. Gilad, Sex-specific genetic architecture of human disease. Nat Rev Genet, 2008. **9**(12): p. 911-22.

143. Chung, D., et al., Estrogen mediated epithelial proliferation in the uterus is directed by stromal Fgf10 and Bmp8a. Mol Cell Endocrinol, 2015. **400**: p. 48-60.

144. Agarwal, A.K., S. Durani, and B.S. Setty, Dose dependent modulation of receptor dynamics and uterine growth in immature rat by estradiol: importance of

an additional nuclear binding at 24 hr for long-term (72 hr) uterine growth. Endokrinologie, 1982. **79**(2): p. 235-41.

145. Koike, S., M. Sakai, and M. Muramatsu, Molecular cloning and characterization of rat estrogen receptor cDNA. Nucleic Acids Res, 1987. **15**(6): p. 2499-513.

146. Kuiper, G.G., et al., Cloning of a novel receptor expressed in rat prostate and ovary. Proc Natl Acad Sci U S A, 1996. **93**(12): p. 5925-30.

147. Kovats, S., Estrogen receptors regulate innate immune cells and signaling pathways. Cell Immunol, 2015. **294**(2): p. 63-9.

148. Carlsten, H., et al., Estrogen accelerates immune complex glomerulonephritis but ameliorates T cell-mediated vasculitis and sialadenitis in autoimmune MRL lpr/lpr mice. Cell Immunol, 1992. **144**(1): p. 190-202.

149. Singh, R.P., B.H. Hahn, and D.S. Bischoff, Interferon Genes Are Influenced by 17beta-Estradiol in SLE. Front Immunol, 2021. **12**: p. 725325.

150. Costenbader, K.H., et al., Reproductive and menopausal factors and risk of systemic lupus erythematosus in women. Arthritis Rheum, 2007. **56**(4): p. 1251-62.

151. Intriago, M., et al., Clinical Characteristics in Patients with Rheumatoid Arthritis: Differences between Genders. ScientificWorldJournal, 2019. **2019**: p. 8103812.

152. Koch-Henriksen, N. and P.S. Sorensen, The changing demographic pattern of multiple sclerosis epidemiology. Lancet Neurol, 2010. **9**(5): p. 520-32.

153. Matejuk, A., et al., 17 beta-estradiol inhibits cytokine, chemokine, and chemokine receptor mRNA expression in the central nervous system of female mice with experimental autoimmune encephalomyelitis. J Neurosci Res, 2001. **65**(6): p. 529-42.

154. Liu, H.Y., et al., Estrogen inhibition of EAE involves effects on dendritic cell function. J Neurosci Res, 2002. **70**(2): p. 238-48.

155. Gold, S.M., et al., Estrogen treatment decreases matrix metalloproteinase (MMP)-9 in autoimmune demyelinating disease through estrogen receptor alpha (ERalpha). Lab Invest, 2009. **89**(10): p. 1076-83.

156. Hall, O.J. and S.L. Klein, Progesterone-based compounds affect immune responses and susceptibility to infections at diverse mucosal sites. Mucosal Immunol, 2017. **10**(5): p. 1097-1107.

157. Jameson, J.L. and L.J. De Groot, Endocrinology-E-Book: Adult and Pediatric. 2010: Elsevier Health Sciences.

158. Park, C.J., et al., Progesterone Receptor Serves the Ovary as a Trigger of Ovulation and a Terminator of Inflammation. Cell Rep, 2020. **31**(2): p. 107496.

159. Lydon, J.P., et al., Mice lacking progesterone receptor exhibit pleiotropic reproductive abnormalities. Genes Dev, 1995. **9**(18): p. 2266-78.

160. Pepe, G.J. and E.D. Albrecht, Actions of placental and fetal adrenal steroid hormones in primate pregnancy. Endocr Rev, 1995. **16**(5): p. 608-48.

161. Vukusic, S., et al., Pregnancy and multiple sclerosis (the PRIMS study): clinical predictors of post-partum relapse. Brain, 2004. **127**(Pt 6): p. 1353-60.

162. de Man, Y.A., et al., Disease activity of rheumatoid arthritis during pregnancy: results from a nationwide prospective study. Arthritis Rheum, 2008. **59**(9): p. 1241-8.

163. Yates, M.A., et al., Progesterone treatment reduces disease severity and increases IL-10 in experimental autoimmune encephalomyelitis. J Neuroimmunol, 2010. **220**(1-2): p. 136-9.

164. Ecochard, R. and A. Gougeon, Side of ovulation and cycle characteristics in normally fertile women. Hum Reprod, 2000. **15**(4): p. 752-5.

165. Vink, A.S., et al., Effect of age and gender on the QTc-interval in healthy individuals and patients with long-QT syndrome. Trends Cardiovasc Med, 2018. **28**(1): p. 64-75.

166. Goemaere, S., et al., Onset of symptoms of rheumatoid arthritis in relation to age, sex and menopausal transition. J Rheumatol, 1990. **17**(12): p. 1620-2.

167. Longcope, C., T. Kato, and R. Horton, Conversion of blood androgens to estrogens in normal adult men and women. J Clin Invest, 1969. **48**(12): p. 2191-201.

168. Kelch, R.P., et al., Estradiol and testosterone secretion by human, simian, and canine testes, in males with hypogonadism and in male pseudohermaphrodites with the feminizing testes syndrome. J Clin Invest, 1972. **51**(4): p. 824-30.

169. Longcope, C., et al., Aromatization of androgens by muscle and adipose tissue in vivo. J Clin Endocrinol Metab, 1978. **46**(1): p. 146-52.

170. Bujan, L., et al., Increased oestradiol level in seminal plasma in infertile men. Hum Reprod, 1993. **8**(1): p. 74-7.
171. Sartorius, G., et al., Serum testosterone, dihydrotestosterone and estradiol concentrations in older men self-reporting very good health: the healthy man study. Clin Endocrinol (Oxf), 2012. **77**(5): p. 755-63.
172. Hart, R.J., et al., Testicular function in a birth cohort of young men. Hum Reprod, 2015. **30**(12): p. 2713-24.
173. Tea, N.T., et al., Simultaneous radioimmunoassay of plasma progesterone and 17-hydroxyprogesterone normal values in children, in men and in women throughout the menstrual cycle and in early pregnancy. J Steroid Biochem, 1975. **6**(11-12): p. 1509-16.
174. Courant, F., et al., Assessment of circulating sex steroid levels in prepubertal and pubertal boys and girls by a novel ultrasensitive gas chromatography-tandem mass spectrometry method. J Clin Endocrinol Metab, 2010. **95**(1): p. 82-92.
175. Davison, S.L., et al., Androgen levels in adult females: changes with age, menopause, and oophorectomy. J Clin Endocrinol Metab, 2005. **90**(7): p. 3847-53.
176. Handelsman, D.J., K. Sikaris, and L.P. Ly, Estimating age-specific trends in circulating testosterone and sex hormone-binding globulin in males and females across the lifespan. Ann Clin Biochem, 2016. **53**(Pt 3): p. 377-84.
177. Abi-Ghanem, C., L.S. Robison, and K.L. Zuloaga, Androgens' effects on cerebrovascular function in health and disease. Biol Sex Differ, 2020. **11**(1): p. 35.
178. Van Anders, S.M. and N.V. Watson, Menstrual cycle irregularities are associated with testosterone levels in healthy premenopausal women. Am J Hum Biol, 2006. **18**(6): p. 841-4.
179. Seminog, O.O., et al., Associations between Klinefelter's syndrome and autoimmune diseases: English national record linkage studies. Autoimmunity, 2015. **48**(2): p. 125-8.
180. van Vollenhoven, R.F., E.G. Engleman, and J.L. McGuire, An open study of dehydroepiandrosterone in systemic lupus erythematosus. Arthritis Rheum, 1994. **37**(9): p. 1305-10.

181. van Vollenhoven, R.F., et al., A double-blind, placebo-controlled, clinical trial of dehydroepiandrosterone in severe systemic lupus erythematosus. Lupus, 1999. **8**(3): p. 181-7.

182. Lienenklaus, S., et al., Novel reporter mouse reveals constitutive and inflammatory expression of IFN-beta in vivo. J Immunol, 2009. **183**(5): p. 3229-36.

183. McLean, A.C., et al., Performing vaginal lavage, crystal violet staining, and vaginal cytological evaluation for mouse estrous cycle staging identification. J Vis Exp, 2012(67): p. e4389.

184. Dangi, A., et al., Murine CMV induces type 1 IFN that impairs differentiation of MDSCs critical for transplantation tolerance. Blood Adv, 2018. **2**(6): p. 669-680.

185. Wang, Y., et al., MBD2 serves as a viable target against pulmonary fibrosis by inhibiting macrophage M2 program. Sci Adv, 2021. **7**(1).

186. Liu, Y.F., et al., Progesterone induces the expression of lipocalin-2 through Akt-c-Myc pathway during mouse decidualization. FEBS Lett, 2016. **590**(16): p. 2594-602.

187. Matsumoto, Y.K., M. Kasai, and K. Tomihara, The enhancement effect of estradiol on contextual fear conditioning in female mice. PLoS One, 2018. **13**(5): p. e0197441.

188. Li, C., et al., Avian influenza A H7N9 virus induces severe pneumonia in mice without prior adaptation and responds to a combination of zanamivir and COX-2 inhibitor. PLoS One, 2014. **9**(9): p. e107966.

189. Kessler, N., et al., Monocyte-derived macrophages aggravate pulmonary vasculitis via cGAS/STING/IFN-mediated nucleic acid sensing. J Exp Med, 2022. **219**(10).

190. Luksch, H., et al., STING-associated lung disease in mice relies on T cells but not type I interferon. J Allergy Clin Immunol, 2019. **144**(1): p. 254-266 e8.

191. Enders, M., et al., Splenic Red Pulp Macrophages Cross-Prime Early Effector CTL That Provide Rapid Defense against Viral Infections. J Immunol, 2020. **204**(1): p. 87-100.

192. Cossarizza, A., et al., Guidelines for the use of flow cytometry and cell sorting in immunological studies (third edition). Eur J Immunol, 2021. **51**(12): p. 2708-3145.

193. van Timmeren, M.M., P. Heeringa, and C.G. Kallenberg, *Infectious triggers for vasculitis.* Curr Opin Rheumatol, 2014. **26**(4): p. 416-23.
194. Van Hoecke, L., et al., Bronchoalveolar Lavage of Murine Lungs to Analyze Inflammatory Cell Infiltration. J Vis Exp, 2017(123).
195. Smetana, K., D. Mikulenkova, and H. Klamova, Heterochromatin density (condensation) during cell differentiation and maturation using the human granulocytic lineage of chronic myeloid leukaemia as a convenient model. Folia Biol (Praha), 2011. **57**(5): p. 216-21.
196. Coppo, P., et al., Antineutrophil cytoplasmic antibody-associated neutropenia. Eur J Intern Med, 2004. **15**(7): p. 451-459.
197. Amulic, B., et al., Cell-Cycle Proteins Control Production of Neutrophil Extracellular Traps. Dev Cell, 2017. **43**(4): p. 449-462 e5.
198. Di, A., et al., A novel function of sphingosine kinase 1 suppression of JNK activity in preventing inflammation and injury. J Biol Chem, 2010. **285**(21): p. 15848-57.
199. Nguyen, G.T., E.R. Green, and J. Mecsas, Neutrophils to the ROScue: Mechanisms of NADPH Oxidase Activation and Bacterial Resistance. Front Cell Infect Microbiol, 2017. **7**: p. 373.
200. Mittal, M., et al., Reactive oxygen species in inflammation and tissue injury. Antioxid Redox Signal, 2014. **20**(7): p. 1126-67.
201. Haag, S.M., et al., Targeting STING with covalent small-molecule inhibitors. Nature, 2018. **559**(7713): p. 269-273.
202. Tsou, C.L., et al., Critical roles for CCR2 and MCP-3 in monocyte mobilization from bone marrow and recruitment to inflammatory sites. J Clin Invest, 2007. **117**(4): p. 902-9.
203. Cao, H., et al., Red blood cell mannoses as phagocytic ligands mediating both sickle cell anaemia and malaria resistance. Nat Commun, 2021. **12**(1): p. 1792.
204. Weis, S., et al., Metabolic Adaptation Establishes Disease Tolerance to Sepsis. Cell, 2017. **169**(7): p. 1263-1275 e14.
205. Consonni, F.M., et al., Heme catabolism by tumor-associated macrophages controls metastasis formation. Nat Immunol, 2021. **22**(5): p. 595-606.

206. Hong, K. and Y. Choi, Role of estrogen and RAS signaling in repeated implantation failure. BMB Rep, 2018. **51**(5): p. 225-229.

207. Cunha, G.R. and B. Lung, The importance of stroma in morphogenesis and functional activity of urogenital epithelium. In Vitro, 1979. **15**(1): p. 50-71.

208. O'Brien, J.E., et al., Estrogen-induced proliferation of uterine epithelial cells is independent of estrogen receptor alpha binding to classical estrogen response elements. J Biol Chem, 2006. **281**(36): p. 26683-92.

209. Wassmann, K., S. Wassmann, and G. Nickenig, Progesterone antagonizes the vasoprotective effect of estrogen on antioxidant enzyme expression and function. Circ Res, 2005. **97**(10): p. 1046-54.

210. Tervaert, J.W., et al., Association between active Wegener's granulomatosis and anticytoplasmic antibodies. Arch Intern Med, 1989. **149**(11): p. 2461-5.

211. Boomsma, M.M., et al., Prediction of relapses in Wegener's granulomatosis by measurement of antineutrophil cytoplasmic antibody levels: a prospective study. Arthritis Rheum, 2000. **43**(9): p. 2025-33.

212. Han, W.K., et al., Serial ANCA titers: useful tool for prevention of relapses in ANCA-associated vasculitis. Kidney Int, 2003. **63**(3): p. 1079-85.

213. Falk, R.J. and J.C. Jennette, Rituximab in ANCA-associated disease. N Engl J Med, 2010. **363**(3): p. 285-6.

214. Szpirt, W.M., J.G. Heaf, and J. Petersen, Plasma exchange for induction and cyclosporine A for maintenance of remission in Wegener's granulomatosis--a clinical randomized controlled trial. Nephrol Dial Transplant, 2011. **26**(1): p. 206-13.

215. Little, M.A., et al., Early mortality in systemic vasculitis: relative contribution of adverse events and active vasculitis. Ann Rheum Dis, 2010. **69**(6): p. 1036-43.

216. Shochet, L., S. Holdsworth, and A.R. Kitching, *Animal Models of ANCA Associated Vasculitis.* Front Immunol, 2020. **11**: p. 525.

217. Falk, R.J. and J.C. Jennette, Anti-neutrophil cytoplasmic autoantibodies with specificity for myeloperoxidase in patients with systemic vasculitis and idiopathic necrotizing and crescentic glomerulonephritis. N Engl J Med, 1988. **318**(25): p. 1651-7.

218. Engblom, C., et al., Osteoblasts remotely supply lung tumors with cancer-promoting SiglecF(high) neutrophils. Science, 2017. **358**(6367).

219. Pfirschke, C., et al., Tumor-Promoting Ly-6G(+) SiglecF(high) Cells Are Mature and Long-Lived Neutrophils. Cell Rep, 2020. **32**(12): p. 108164.
220. Zhang, Y., et al., The influence of cathelicidin LL37 in human anti-neutrophils cytoplasmic antibody (ANCA)-associated vasculitis. Arthritis Res Ther, 2013. **15**(5): p. R161.
221. Lande, R., et al., Plasmacytoid dendritic cells sense self-DNA coupled with antimicrobial peptide. Nature, 2007. **449**(7162): p. 564-9.
222. Zhu, B., et al., BCL6 modulates tissue neutrophil survival and exacerbates pulmonary inflammation following influenza virus infection. Proc Natl Acad Sci U S A, 2019. **116**(24): p. 11888-11893.
223. Martin, C., et al., Neutrophil-Expressed p21/waf1 Favors Inflammation Resolution in Pseudomonas aeruginosa Infection. Am J Respir Cell Mol Biol, 2016. **54**(5): p. 740-50.
224. Klausen, P., et al., End-stage differentiation of neutrophil granulocytes in vivo is accompanied by up-regulation of p27kip1 and down-regulation of CDK2, CDK4, and CDK6. J Leukoc Biol, 2004. **75**(3): p. 569-78.
225. Coldren, C.D., et al., Functional and genomic changes induced by alveolar transmigration in human neutrophils. Am J Physiol Lung Cell Mol Physiol, 2006. **291**(6): p. L1267-76.
226. Bar, A., et al., Degradation of Glycocalyx and Multiple Manifestations of Endothelial Dysfunction Coincide in the Early Phase of Endothelial Dysfunction Before Atherosclerotic Plaque Development in Apolipoprotein E/Low-Density Lipoprotein Receptor-Deficient Mice. J Am Heart Assoc, 2019. **8**(6): p. e011171.
227. Cogger, V.C., et al., The effect of acute oxidative stress on the ultrastructure of the perfused rat liver. Pharmacol Toxicol, 2001. **89**(6): p. 306-11.
228. Yang, W., et al., Neutrophils promote the development of reparative macrophages mediated by ROS to orchestrate liver repair. Nat Commun, 2019. **10**(1): p. 1076.
229. Chanock, S.J., et al., The respiratory burst oxidase. J Biol Chem, 1994. **269**(40): p. 24519-22.
230. Simon, H.U., A. Haj-Yehia, and F. Levi-Schaffer, Role of reactive oxygen species (ROS) in apoptosis induction. Apoptosis, 2000. **5**(5): p. 415-8.

231. Chamilos, G., et al., Cytosolic sensing of extracellular self-DNA transported into monocytes by the antimicrobial peptide LL37. Blood, 2012. **120**(18): p. 3699-707.

232. Shin, M.S., et al., Self double-stranded (ds)DNA induces IL-1beta production from human monocytes by activating NLRP3 inflammasome in the presence of anti-dsDNA antibodies. J Immunol, 2013. **190**(4): p. 1407-15.

233. Ong, P.Y., et al., Endogenous antimicrobial peptides and skin infections in atopic dermatitis. N Engl J Med, 2002. **347**(15): p. 1151-60.

234. Sun, C.L., et al., LL-37 expression in the skin in systemic lupus erythematosus. Lupus, 2011. **20**(9): p. 904-11.

235. McNab, F., et al., Type I interferons in infectious disease. Nat Rev Immunol, 2015. **15**(2): p. 87-103.

236. Banchereau, J. and V. Pascual, Type I interferon in systemic lupus erythematosus and other autoimmune diseases. Immunity, 2006. **25**(3): p. 383-92.

237. Kretschmer, S. and M.A. Lee-Kirsch, Type I interferon-mediated autoinflammation and autoimmunity. Curr Opin Immunol, 2017. **49**: p. 96-102.

238. Baechler, E.C., et al., Interferon-inducible gene expression signature in peripheral blood cells of patients with severe lupus. Proc Natl Acad Sci U S A, 2003. **100**(5): p. 2610-5.

239. Motwani, M., et al., Hierarchy of clinical manifestations in SAVI N153S and V154M mouse models. Proc Natl Acad Sci U S A, 2019. **116**(16): p. 7941-7950.

240. Batten, I., et al., Investigation of type I interferon responses in ANCA-associated vasculitis. Sci Rep, 2021. **11**(1): p. 8272.

241. Lund, J., et al., Toll-like receptor 9-mediated recognition of Herpes simplex virus-2 by plasmacytoid dendritic cells. J Exp Med, 2003. **198**(3): p. 513-20.

242. Blaauboer, S.M., V.D. Gabrielle, and L. Jin, MPYS/STING-mediated TNF-alpha, not type I IFN, is essential for the mucosal adjuvant activity of (3'-5')-cyclic-di-guanosine-monophosphate in vivo. J Immunol, 2014. **192**(1): p. 492-502.

243. Gordon, S. and A. Pluddemann, Tissue macrophages: heterogeneity and functions. BMC Biol, 2017. **15**(1): p. 53.

244. Haniffa, M., V. Bigley, and M. Collin, *Human mononuclear phagocyte system reunited.* Semin Cell Dev Biol, 2015. **41**: p. 59-69.

245. Garbi, N. and B.N. Lambrecht, Location, function, and ontogeny of pulmonary macrophages during the steady state. Pflugers Arch, 2017. **469**(3-4): p. 561-572.
246. Muraille, E., O. Leo, and M. Moser, TH1/TH2 paradigm extended: macrophage polarization as an unappreciated pathogen-driven escape mechanism? Front Immunol, 2014. **5**: p. 603.
247. Minutti, C.M., et al., Tissue-specific contribution of macrophages to wound healing. Semin Cell Dev Biol, 2017. **61**: p. 3-11.
248. Wang, X., et al., STING expression in monocyte-derived macrophages is associated with the progression of liver inflammation and fibrosis in patients with nonalcoholic fatty liver disease. Lab Invest, 2020. **100**(4): p. 542-552.
249. Maus, U.A., et al., Resident alveolar macrophages are replaced by recruited monocytes in response to endotoxin-induced lung inflammation. Am J Respir Cell Mol Biol, 2006. **35**(2): p. 227-35.
250. Bleriot, C., et al., Liver-resident macrophage necroptosis orchestrates type 1 microbicidal inflammation and type-2-mediated tissue repair during bacterial infection. Immunity, 2015. **42**(1): p. 145-58.
251. Scott, C.L., et al., Bone marrow-derived monocytes give rise to self-renewing and fully differentiated Kupffer cells. Nat Commun, 2016. **7**: p. 10321.
252. Li, F., et al., Monocyte-derived alveolar macrophages autonomously determine severe outcome of respiratory viral infection. Sci Immunol, 2022. **7**(73): p. eabj5761.
253. Larsen, R., et al., A central role for free heme in the pathogenesis of severe sepsis. Sci Transl Med, 2010. **2**(51): p. 51ra71.
254. Gordon, S., Phagocytosis: An Immunobiologic Process. Immunity, 2016. **44**(3): p. 463-475.
255. Boada-Romero, E., et al., The clearance of dead cells by efferocytosis. Nat Rev Mol Cell Biol, 2020. **21**(7): p. 398-414.
256. Knutson, M. and M. Wessling-Resnick, Iron metabolism in the reticuloendothelial system. Crit Rev Biochem Mol Biol, 2003. **38**(1): p. 61-88.
257. Dondorp, A.M., et al., Red blood cell deformability as a predictor of anemia in severe falciparum malaria. Am J Trop Med Hyg, 1999. **60**(5): p. 733-7.

258. Buffet, P.A., et al., Retention of erythrocytes in the spleen: a double-edged process in human malaria. Curr Opin Hematol, 2009. **16**(3): p. 157-64.

259. Morimoto, A., Y. Nakazawa, and E. Ishii, Hemophagocytic lymphohistiocytosis: Pathogenesis, diagnosis, and management. Pediatr Int, 2016. **58**(9): p. 817-25.

260. Camilli, G., et al., Impaired phagocytosis directs human monocyte activation in response to fungal derived beta-glucan particles. Eur J Immunol, 2018. **48**(5): p. 757-770.

261. Garcia-Senosiain, A., et al., Neutrophils dominate in opsonic phagocytosis of P. falciparum blood-stage merozoites and protect against febrile malaria. Commun Biol, 2021. **4**(1): p. 984.

262. Burger, P., et al., CD47 functions as a molecular switch for erythrocyte phagocytosis. Blood, 2012. **119**(23): p. 5512-21.

263. Adams, S., et al., Signal-regulatory protein is selectively expressed by myeloid and neuronal cells. J Immunol, 1998. **161**(4): p. 1853-9.

264. Lu, Y., et al., Interleukin-33 Signaling Controls the Development of Iron-Recycling Macrophages. Immunity, 2020. **52**(5): p. 782-793 e5.

265. Jansson, L. and R. Holmdahl, Estrogen-mediated immunosuppression in autoimmune diseases. Inflamm Res, 1998. **47**(7): p. 290-301.

266. Wagner, A.H., M.R. Schroeter, and M. Hecker, 17beta-estradiol inhibition of NADPH oxidase expression in human endothelial cells. FASEB J, 2001. **15**(12): p. 2121-30.

267. Seli, E., et al., Estradiol down-regulates MCP-1 expression in human coronary artery endothelial cells. Fertil Steril, 2002. **77**(3): p. 542-7.

268. Yamada, K., et al., Physiological concentration of 17 beta-estradiol inhibits chemotaxis of human monocytes in response to monocyte chemotactic protein 1. Artery, 1996. **22**(1): p. 24-35.

269. Xing, D., et al., Estradiol and progestins differentially modulate leukocyte infiltration after vascular injury. Circulation, 2004. **109**(2): p. 234-41.

270. Janis, K., et al., Estrogen decreases expression of chemokine receptors, and suppresses chemokine bioactivity in murine monocytes. Am J Reprod Immunol, 2004. **51**(1): p. 22-31.

271. Giraud, S.N., et al., Estradiol inhibits ongoing autoimmune neuroinflammation and NFkappaB-dependent CCL2 expression in reactive astrocytes. Proc Natl Acad Sci U S A, 2010. **107**(18): p. 8416-21.

272. Kowalik, M.K., R. Rekawiecki, and J. Kotwica, The putative roles of nuclear and membrane-bound progesterone receptors in the female reproductive tract. Reprod Biol, 2013. **13**(4): p. 279-89.

273. Koh, K.K., Effects of estrogen on the vascular wall: vasomotor function and inflammation. Cardiovasc Res, 2002. **55**(4): p. 714-26.

274. Iyer, A.K., et al., Nitric oxide mediates bleomycin-induced angiogenesis and pulmonary fibrosis via regulation of VEGF. J Cell Biochem, 2015. **116**(11): p. 2484-93.

275. Hayashi, T., et al., Basal release of nitric oxide from aortic rings is greater in female rabbits than in male rabbits: implications for atherosclerosis. Proc Natl Acad Sci U S A, 1992. **89**(23): p. 11259-63.

276. Bath, P.M., et al., Nitric oxide and prostacyclin. Divergence of inhibitory effects on monocyte chemotaxis and adhesion to endothelium in vitro. Arterioscler Thromb, 1991. **11**(2): p. 254-60.

277. Salamonsen, L.A. and L.J. Lathbury, *Endometrial leukocytes and menstruation.* Hum Reprod Update, 2000. **6**(1): p. 16-27.

278. Critchley, H.O., et al., The endocrinology of menstruation--a role for the immune system. Clin Endocrinol (Oxf), 2001. **55**(6): p. 701-10.